Department of Precision and Microsystems Engineering

Semi-Analytical Thermal Modelling of Laser Powder Bed Fusion Process: Influence of Laser Source shapes on Defects studied through Process Maps

Kanza Zafar

Report no : 2025.067
Coach : Dr. Can Ayas
Professor : Dr. Can Ayas
Specialisation: Computational Design and Mechanics
Type of report Master Thesis
Date : 29 October 2025

TU Delft Delft University of Technology

Challenge the future

Delft University of Technology

MSc. Thesis
(ME56035)

Semi-Analytical Thermal Modelling of Laser Powder Bed Fusion Process: Influence of Laser Source shapes on Defects studied through Process Maps

---

Department of Precision and Microsystems Engineering
Research Group: Computational Design and Mechanics

Author:
Kanza Zafar

Supervisors:
Dr. Can Ayas
Date: 29 October 2025

Acknowledgments

I begin by expressing gratitude to the Almighty, whose guidance and blessings have been my source of strength throughout this journey. As the Qur'an beautifully says, 'My Lord, increase me in knowledge' (20:114).
I would like to express my sincere gratitude to my thesis supervisor, Professor Can Ayas, for his exceptional guidance and insightful feedback throughout the course of this research. His expertise in additive manufacturing and computational modelling has been pivotal in shaping the technical rigor and overall direction of this work. I am also deeply thankful to Yang for his continuous support and for patiently addressing my questions on a daily basis.
I extend my heartfelt thanks to my family for their unwavering love, patience, and constant belief in me throughout this journey. Their support has been a vital source of strength. In particular, I would like to acknowledge my mother, Amma, whose support during my most difficult moments made it possible for me to complete this work.
I would also like to extend my gratitude to my friends and peers, with whom I had the opportunity to have discussions, which gave me different perspectives and I would also like to thank them for their support.
Finally, I would like to express my profound gratitude to TU Delft for awarding me the prestigious Justus and Louise van Effen Excellence Scholarship. This opportunity not only enabled me to pursue my dream of a master's degree but also provided an inspiring academic environment that continuously fostered my curiosity and deepened my passion for research.

Abstract

Laser Powder Bed Fusion (L-PBF) is a metal additive manufacturing process in which localized melting and rapid solidification govern the formation of successive layers. The focused and transient nature of the laser–material interaction makes the thermal history and melt-pool geometry highly sensitive to parameters such as laser power, scan velocity, and spatial energy distribution. Most thermal models represent the laser as a Gaussian heat source, which captures energy concentration near the beam center, but often overestimates temperature gradients and underestimate uniform heating regions. Alternative non-Gaussian profiles, such as square or top-hat intensity distributions, offer a more uniform power density that can reduce peak temperatures, limit keyhole instability, and promote consistent melt-pool formation. However, the quantitative influence of these beam-shape variations on melt-pool morphology, thermal stability, and defect formation remains inadequately characterized, underscoring the need for systematic modeling of non-Gaussian source effects in L-PBF.

In this study, a semi-analytical thermal model is utilized to investigate the influence of different laser source shapes on the melt-pool geometry and thermal history during single-track scanning of Ti-6Al-4V. The model simulates the temperature evolution by representing the moving laser spot as a finite set of heat sources. The temperature field is obtained by superimposing analytical solutions for heat sources in a semi-infinite medium. To accurately account for boundary effects, a finite-difference correction field is superimposed on the analytical solution. The analytical temperature field for different source shapes is obtained by convolving the laser intensity distribution with the Green's function solution of the transient heat conduction equation. The model computes three-dimensional temperature transients and extracts melt-pool width and depth based on the isotherm corresponding to the alloy's melting temperature.

A parametric computational study across a wide range of laser powers and scan velocities is performed to construct Power–Velocity (PV) process maps, identifying regimes of conduction, lack-of-fusion, and keyholing. Results show that non-Gaussian profiles, such as top-hat beams, significantly expand the defect-free window by promoting uniform melt-pool geometry and reducing thermal gradients. The proposed framework offers a physically consistent and computationally efficient approach for predicting temperature fields and defect formation, enabling process optimization and laser beam design in advanced L-PBF systems.

List of Figures

List of Tables

Contents

1 Introduction

1.1 Background and Motivation

Additive manufacturing (AM) is paving the way towards the next industrial revolution and has emerged as a transformative technology with major implications in various industries, including aerospace, automotive, and biomedical [9]. It offers the ability to fabricate complex and customized parts with enhanced performance characteristics. The ability to develop such complex geometries is not always possible through conventional manufacturing methods.

Laser Powder Bed Fusion (L-PBF) is an additive manufacturing technique in which a high-energy laser selectively melts layers of metal powder to fabricate complex components, based on digital models derived from CAD files. The working principles of L-PBF involves intricate interactions between the laser, metal powder, and melt pool dynamics, making it a highly complex process. As the laser scans the powder bed, it quickly melts the material and creates a molten region called the melt pool. This pool cools and solidifies rapidly, forming the solid part. After the cross-section of a layer is completed, the build plate lowers by a set distance, referred to as the layer thickness. The process takes place in a sealed chamber under inert gas conditions [10]. A schematic of the process is shown in Figure 1 below:

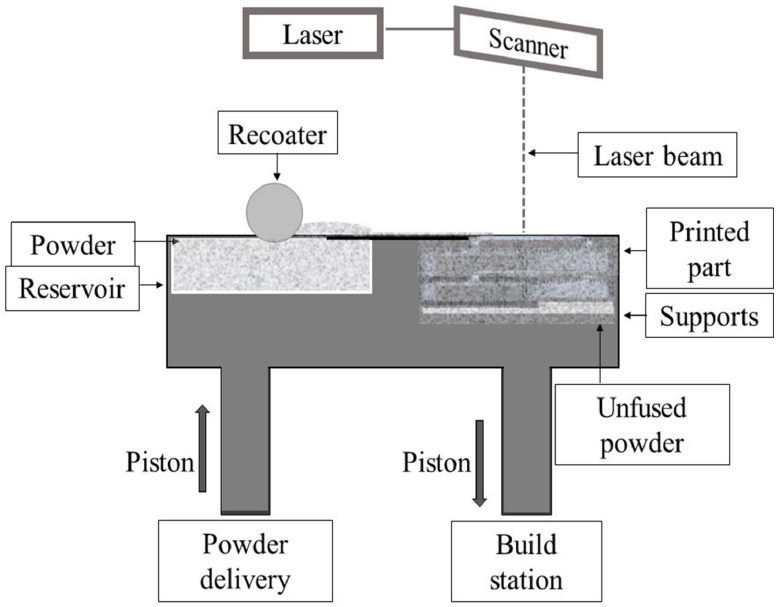

Figure 1.1: Schematic of the L-PBF Process, reproduced from [1]

Understanding the physical phenomena in laser melting, particularly laser–matter interaction, is essential for controlling melt pool behaviour [11]. The laser beam profiles are directly correlated with the laser-material interaction and recent studies suggests that the laser intensity profiles as a critical factor influencing the processing window, melt-pool shape and dimension, and product quality in additive manufacturing. Moreover, the design and optimisation of laser beam profiles usually relies on trial-and-error experiments that are generally expensive and

time-consuming. This highlights the necessity of developing reliable predictive models that facilitate design-space exploration and process optimization within a reasonable timeframe. The different laser beam profiles affects the thermal history which also have effects over the melt pool shapes. However, widespread adoption of L-PBF with metallic parts hinges on to solving a main challenge: the requirement that the final product should meet engineering quality standards [12]. Experiments relies on trial and error methods, which are time consuming and inefficient, so a better way to go for it would be modelling and simulation and it is integral that the effects of process and design parameters on part quality are known prior to entering the production environment. In L-PBF, the characteristics of the laser beam play a key role in determining the quality of the manufactured parts. Different laser beam profiles are defined by how energy is distributed spatially and temporally. These characteristics strongly affect the melt pool profiles and the thermal gradients [13], [3].

1.2 Heat Transfer Mechanisms in L-PBF

The melt pool constitutes the essential unit of the L-PBF process and serves as the foundational element for any component. The melt track can be divided into three distinct regions: a transition zone in between, a tail end region near the end of the melt track, and a depression region at the laser spot. Firstly, the heat is generated where the laser rays hit the surface of the powder particles and diffuses inward, whereas homogeneous deposition heats the inner volume of the particle uniformly [12]. Further heat input will be transmitted to the surrounding loose powder by conduction while the laser keeps irradiating the melt pool. The melt pool is said to be in the "conduction mode" when conduction is the primary heat transmission mechanism during the melting process [14]. Heat dissipates into the surrounding material, melting it as the laser moves, until a steady state is established in which there is clear solid-liquid interface forms between the melt pool and the adjacent loose powder [15]. In the conduction mode the heat transfer is not 100% efficient as the loose powder will reflect some of the laser beam. The ratio of the energy that is absorbed by the powder or melt pool to the total energy output from the laser is known as absorptivity [16]. The absorptivity of the metal is a material-dependent property and has also been shown to be dependent on the physical properties of the powder used in the process [17].

The melt pool formation mechanisms for the conduction mode is given in the Figure 1.2(a), where the red arrows represent the path and penetration of the laser energy into the material. They show how the laser power is distributed and deposited into the melt pool. Blue arrows indicate the direction of heat conduction into the surrounding, unmelted material. These arrows show how thermal energy spreads away from the melt pool into the bulk solid. Black arrows illustrate the powder particle movement within the melt pool (in a and b) and, in (c), also show the vapor flow direction inside the vapor depression (keyhole). They highlight the internal material movement or vapor movement caused by temperature gradients and laser-material interaction.

When the energy input is below a material-dependent threshold, the melt pool remains in the conduction mode. At higher energy input, the laser begins to vaporize the top of the melt pool. Vaporization at the laser focus generates a significant recoil pressure on the liquid metal surface, forming a depression at the center of the melt pool. This pressure-driven cavity causes incident laser rays to interact with and reflect off the depression walls, promoting multiple internal reflections and enhanced absorption, until a steady-state keyhole shape is established. At this stage, the melt pool enters the "keyhole" mode, and this is named because of its keyhole-

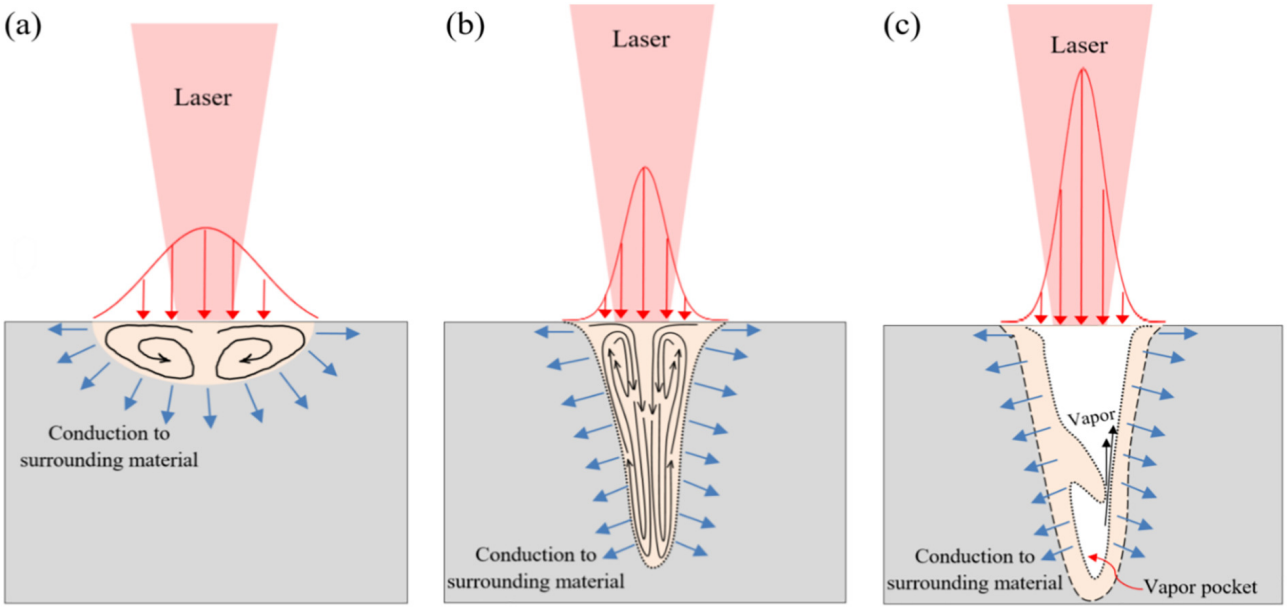

Figure 1.2: Melt-pool formation mechanisms a) conduction Mode b) keyhole mode c) keyhole with porosity, reproduced from [2].

shaped cross-section [18]. An example of the melt pool in the keyhole mode is given in the Figure 1.2 (b). In keyhole mode, the increased melt pool surface area generates surface tension, which is counterbalanced by the recoil pressure from vaporization. This balance prevents the surrounding molten material from collapsing inward, Figure 1.2 (c). Also the dotted lines in the Figure 1.2 illustrates the solid-liquid interface that bounds the central keyhole cavity formed by the recoil pressure. Between conduction and keyhole modes lies a transition regime, but there is no clear boundary that marks the change. A common rule of thumb is that keyhole mode is reached when the melt pool aspect ratio, defined as depth divided by width, exceeds 0.5 [19]. Since melt pool control is critical for part quality, extensive research has focused on accurately predicting melt pool geometry [20].

1.3 Laser source shapes in L-PBF

Like other manufacturing methods, the quality of parts produced by L-PBF depends on several process parameters, including laser power, scanning speed, hatch spacing, and powder characteristics. These parameters influence relative density (the ratio of measured density to the theoretical density), surface finish, microstructure, mechanical properties, and residual stresses. They are generally classified as laser-related, scan-related, powder-related, and temperature-related parameters. While many studies have focused on optimizing these parameters to achieve defect-free parts, comparatively little research has examined the role of laser beam shape and its intensity distribution in L-PBF. The laser source shapes is basically the physical beam profile at focus. The dimensions and shape of the laser beam intensity profile are important factors influencing the thermal fields in L-PBF. The tuning of spatial laser intensity profiles will lead to different heat source shapes. Some common laser beam profiles are given in the Figure 1.3. Some of the commonly used source shapes includes elliptical and circular with Gaussian intensity profiles 1.3 (a and d). The laser intensity or heat distribution typically conforms to a Gaussian beam shape in most commercially available L-PBF processes. While widely used, this peak intensity limits the use of higher laser powers, as it can cause local overheating,

evaporation, balling, spatter formation, and large thermal gradients with rapid solidification [21]. Gaussian beams often lead to deep melt pools, strong convection, and chaotic or predominantly columnar microstructures. There is a limitation on the build rate associated with the Circular Gaussian profile and it primarily stems from the compromise required to achieve desired microstructural properties and maintain process stability, despite its potential for high raw throughput.

Elliptical beams offer an improved microstructure due to lower thermal gradients and shallower melt depths. The intensity distribution for the elliptical beams is spread over a non-circular, elongated area. The other type of beam includes the square beam profile which is a form of laser beam shaping characterized by a uniform intensity profile. The melt pool profile for the square beam is more spread out as compared to the Gaussian source. It generally have lower peak temperatures compared to Circular Gaussian beams, as the energy is dispersed.

Another laser beam configuration used in laser powder bed fusion, though less common, is the ring-shaped beam, also referred to as the annular or doughnut-shaped beam profile. This beam shape is characterized by a central region of low intensity surrounded by a circumferential ring of relatively uniform energy distribution. The annular beam delivers energy predominantly along a radial ring, enabling modified thermal gradients and melt pool dynamics. In experimental systems, the annular profile is often realized with a double-core configuration, where the beam comprises two concentric rings with distinct radii [13], as illustrated in Figure 1.3(e).

Some beams have uniform intensity profile where they are also referred to as top-hat, and flat-top and are generally used interchangeably used to describe a laser beam intensity distribution where the energy is spread relatively evenly across the beam spot, as opposed to being concentrated at the center (like a Gaussian profile), 1.3 (b, c and f). Flat-top lasers, with their large, uniformly distributed energy, promote directional growth of columnar grains by creating wider and shallower melt pools with moderate flow of molten metal, thus enabling the production of parts with tailored crystal orientations for specific applications [22, 23]. For certain beam shapes, such as circular, square, or ring profiles, a uniform intensity distribution is often used to ensure consistent energy delivery across the illuminated area.

Limited studies in this field have been done where non-Gaussian laser source shapes and their effect on defect mitigation and process optimization have been looked into. The shape of the beam with the Gaussian intensity profile tends to create more process instabilities and can cause spatter, whereas the source shapes with the uniform intensity profiles (top-hat) will have more stable process and less spattering. For the circular Gaussian and circular top-hat cases, the melt pool dimensions are particularly comparable. The top-hat case being less as compared to the gaussian circular but there is a difference in the peak temperatures [11]. Table 1.1 serves as a comprehensive summary of the effects of different beam shapes in the L-PBF process. It provides key information and insights into how the choice of beam shape influences the factors like surface roughness, build rate, process stability and melt pool morphology. It serves as a valuable reference for understanding the impact of beam shape selection in L-PBF and facilitates informed decision-making in process optimization.

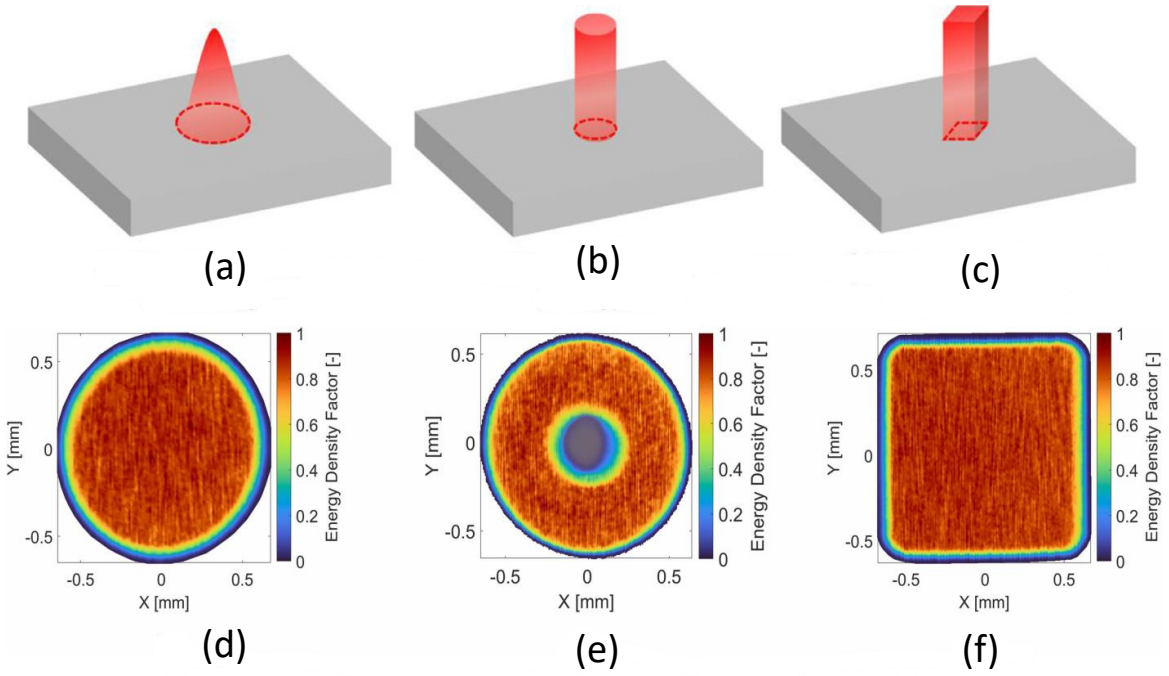

Figure 1.3: Some common laser profiles: (a) surface circular Gaussian, (b) surface uniform-intensity circular, (c) uniform-intensity square, (d) normalized laser beam energy density profile for a uniform circular source, (e) normalized laser beam energy density profile for a ring source, and (f) normalized laser beam energy density profile for a square source. Reproduced from [3, 4].

Table 1.1: Comparitive study of impact of laser source shapes on different factors

Source Shape	**Intensity Distribution**	**Melt pool geometry**	**Process stability**	**References**
Circular-Gaussian	Concentrated at the center, gradually tapering off toward the edges	Deep and narrow	Limited build rate, high spattering, unstable process at high laser powers, limited process window	[11]
Top-Hat Square	Uniform distribution across a larger area and Lower peak intensity	Wider melt pool due to larger area	More stable due to larger melt pool area	[3, 11]
Top-hat Circular	Uniform energy profile	comparable Melt pool size with the gaussian-circular but there is a difference in peak temperatures	faster fluid flow and instabilities	[3, 11]

Source Shape	Intensity Distribution	Melt pool geometry	Process stability	References
Ring	High at the edges, low in the center	Shallow and wide	Improved build rate, less spattering, larger process window, and higher laser power needed to produce fully dense parts	[3]
Elliptical	Elongated Gaussian beam shape	Shallow and elongated	Stable melt tracks at large beam diameters	[23, 24]

1.4 Defect Mechanisms and Process Maps

Defect formation mechanisms such as lack-of-fusion (LOF) and Keyhole porosity are critical considerations in Laser Powder Bed Fusion (L-PBF) additive manufacturing, and their understanding is essential for defining optimal processing regions to produce high-quality, defect-free parts. In the previous section, the physics underlying the melting modes was explained, along with their influence on the types of defects formed during processing. Defects in L-PBF parts can arise in three main ways: transfer from the feedstock powder, the laser–powder–metal interaction during melting, or post-processing treatments. The most common defect types include lack-of-fusion porosity, keyhole porosity, balling, and gas porosity [8]. Of these, the laser-powder-metal interaction is the most common means of porosity transfer during metal AM processing, where defects such as "keyhole" and "lack-of-fusion" (LOF) porosity can be generally observed.

LOF porosity is characterized by large, irregularly shaped pores that often contain unmelted powder particles, Figure 1.4(a). These defects are particularly detrimental to mechanical behavior because of their sharp corners. LOF defects are mainly attributed to conditions in which not all locations in the powder bed are sufficiently melted. The primary reasons involves low laser power and high laser scan velocity. This corresponds to a region of low energy density input. To mitigate LOF porosity, a geometric modeling approach is frequently used to predict its boundary within the processing parameter space. The key geometric criterion for avoiding lack-of-fusion (LOF) defects is to ensure sufficient overlap between adjacent melt pools and to maintain a melt-pool depth greater than the layer thickness [5, 25].

Keyhole porosity results in large, spherical pores. These defects often form in pairs and are observed deep beneath the uppermost boundary of the loose powder layer (i.e., the powder surface) that is freshly spread before each laser pass. Keyhole formation occurs under conditions of excessive energy input. The instability of this vapor depression (keyhole), particularly at the base of the keyhole cavity, leads to the pinch-off of gas bubbles (pores), Figure 1.4(b), that can become trapped in the solidifying part. Keyholes with large aspect ratios are prone to front wall fluctuations that generate these bubbles. Front wall fluctuations means oscillations or instability of the keyhole's leading boundary, which is most exposed to the incoming laser energy and dynamic fluid flow. This directly contributes to gas bubble generation due to uneven collapse or pinching of the cavity walls. The boiling and evaporation of material due to high energy input also contributes to porosity. The melt pool depth-to-width (D/W) ratio (aspect ratio) is a common indicator, with $D/W > 0.5$ often identifying keyhole mode.

Optimal regions in the "process windows" also referred to as "printability maps," represent the combinations of processing parameters where parts with nominally full density (>99.9% volumetric density) and minimal defects can be reliably produced. There is a perfect melt pool overlap is expected to happen in optimal regions, see Figure 1.4 (b). The "optimal" regions on predictive P-V maps typically represents the set of processing parameters least likely to cause porosity defects.

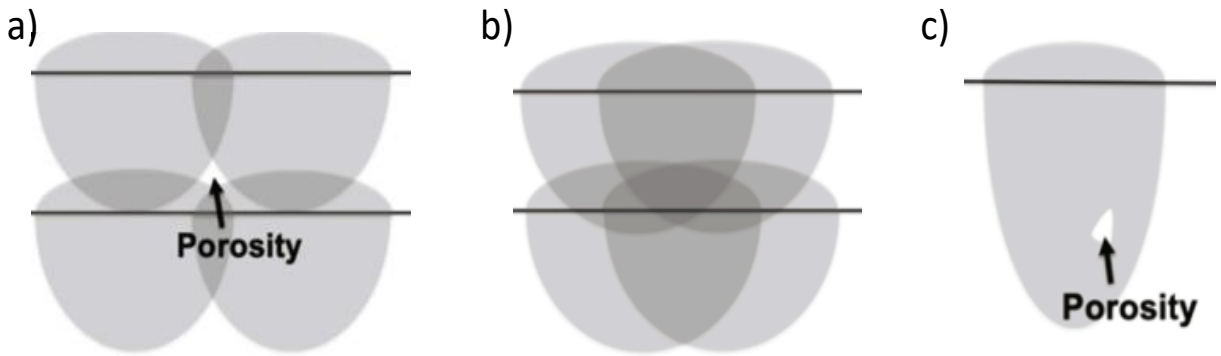

Figure 1.4: Simplified cross-sections of melt pool tracks showing typical sites of porosity defects: (a) lack-of-fusion due to insufficient overlap and penetration, (b) optimal semi-spherical melt pool with sufficient overlap, and (c) keyhole porosity caused by excessive penetration of the fusion zone. Reproduced from [5].

According to the literature, the main process parameters that govern the physics of L-PBF are:

- **Laser power (P):** the energy intensity of the laser.
- **Scan speed (v):** the velocity at which the laser moves across the powder bed.
- **Hatch spacing (h):** the distance between adjacent laser scan tracks.
- **Layer thickness (t):** the thickness of material added per layer, corresponding to the downward movement of the build platform after each layer.

Process mapping techniques define process outcomes as a function of process variables. The most immediate L-PBF process maps are a function of laser power and scan speed, titled P-V maps. A generalized defect formation P-V map is shown in the following Figure 1.5 and defines a process window bounded by three distinct defect formation mechanisms in L-PBF. Printability maps can be developed using fully computational, predictive approaches that leverage physics-based thermal models and various defect formation criteria. These frameworks can estimate material properties, simulate single-track melt pool dimensions, and classify tracks as defective or defect-free, mapping these onto power-velocity space [26, 27].

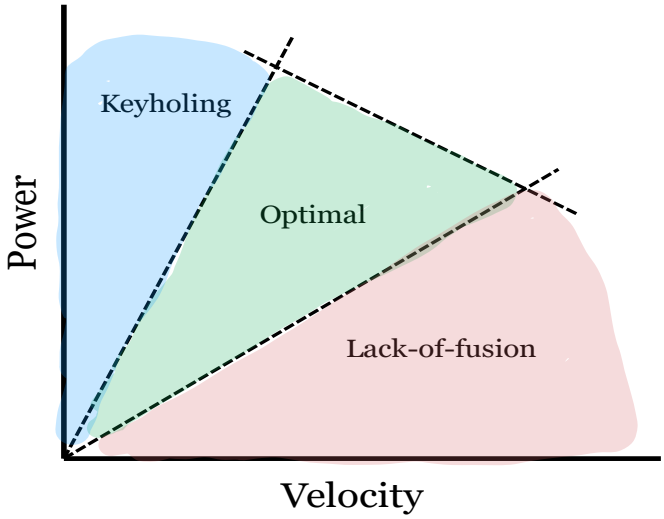

Figure 1.5: A representative L-PBF process window delineates the operating regimes associated with lack-of-fusion and keyholing defects, with the bounded interior identifying the domain of parameter combinations that yield stable, defect-minimized (optimal) melt pools.

1.5 State-of-the-art

Defects such as porosity and keyholing significantly undermine the structural integrity of L-PBF components, particularly in aerospace applications where fatigue resistance is critical. Conventional Gaussian laser beam profiles, while widely used, often lead to excessive thermal gradients and uneven melt pool behavior, exacerbating these defects. In contrast, non-Gaussian profiles like top-hat [15] and ring beams [3] offer the potential to reduce thermal gradients and stabilize the melt pool, thereby mitigating defect formation. In the study done by [28], for low layer thicknesses, the RSBP (Ring spot Beam profile), which refers to a point in between a ring profile can increase the possible build rate for Ti-6Al-4V, offering reduced surface roughness and no significant disadvantage in hardness compared to GBP (Gaussian Beam Profile). However, for high layer thicknesses, GBP leads to higher relative densities and overall higher build rates, despite potentially higher roughness values. This is attributed to the RSBP's reduced penetration depth into the melt pool compared to GBP. Higher scanning speeds with RSBP lead to a stronger decrease in part quality. Only the higher intensity of GBP at higher scanning speeds achieves sufficient melt pool depth to avoid delamination and lack-of-fusion defects.

In the study by [29], it was reported that beam shaping-particularly through the use of ring-core and inverse-calculated beam profiles-significantly reduces the laser penetration depth compared to the conventional Gaussian distribution. These tailored beam profiles consistently promote conduction-mode melting, as indicated by a depth-to-width ratio of less than 0.8. Recent studies indicate that inverse-designed beam profiles with larger spot sizes-particularly ring-core–type distributions-substantially broaden the usable L-PBF process window. These profiles promote wider, more stable melt pools and support higher scan velocities, enabling defect-resistant operation with less parameter sensitivity. Incorporating tailored laser source shapes offers a fresh approach to reducing defects and optimizing L-PBF performance by utilising Power-Velocity Maps for predicting the defect-free regions. This strategy seeks to establish a process window defined by both defect content and laser source shapes, enhancing material

properties and expanding the capabilities of L-PBF. Despite advancements in process modeling, the role of alternative non-Gaussian laser source shapes, such as top-hat and ring, remains underexplored.

From the literature, it is safe to say that, the investigation of efficient methods to reduce defects in L-PBF processes that are supported by thorough quantitative analysis and validation represents a research gap. Despite increasing interest in alternative laser beam profiles, the specific impact of different laser source shapes-particularly circular Gaussian and rectangular top-hat profiles-on defect formation in L-PBF remains insufficiently explored when analyzed through semi-analytical thermal modeling approaches. Existing research mainly focuses on parameter studies or experimental observations for Gaussian and non-Gaussian beams but lacks systematic semi-analytical investigations quantifying how these source shapes influence melt pool thermal fields, solidification behavior, and resulting defect mechanisms such as lack-of-fusion porosity and keyholing. This gap constrains accurate prediction and process optimization across varying source geometries. Future studies should look into a wider range of process variables and how they relate with the source shapes. This would help identify the optimal processing parameters that minimize defects in Powder Bed Fusion made products by employing varied source shapes.

1.6 Problem Motivation and Research Scope

Additive manufacturing by laser powder bed fusion (L-PBF) still lacks robust guidance on how laser beam shape influences defect formation and the size/shape of the melt pool. Most prior work focuses on Gaussian beams and treats the laser as an idealized point or axisymmetric source. In contrast, non-Gaussian profiles (e.g., top-hat, square, elliptical, ring-core) are only under explored, and their role in widening the defect-free operating window is not well quantified. This limits our ability to tailor process parameters for stable melting in alloys such as Ti-6Al-4V.

1.6.1 Research Gap

The key research gaps identified from the literature includes the following:

1. Limited, systematic study of non-Gaussian laser source shapes and their impact on lack-of-fusion and keyhole defects.

2. Inconsistent mathematical definitions of laser source profiles and boundary conditions in semi-analytical thermal models hinder direct comparison of melt pool predictions across studies.

3. Using semi-analytical thermal models to quickly test power–speed settings and sort them into “defect” or “no-defect” cases has been used only sparingly.

1.6.2 Research Question

What is the optimal power–velocity process window for defect-free L-PBF of Ti-6Al-4V when using rectangular (top-hat square) and circular (Gaussian) laser sources?

1.6.3 Objectives

The objectives to achieve this includes the following:

1. Closed-form Temperature field equations: Derive and present closed-form analytical temperature solutions for the target source shapes, focusing on a top-hat square source and a 2D circular Gaussian source.

2. Model fidelity: Implement accurate source representations within a semi-analytical thermal L-PBF process modelling framework and benchmark against a point-source formulation.

3. Process maps: Compute steady-state melt pool dimensions (depth and width) for single-track cases, classify defect regimes, and construct power–velocity process maps for each source shape to identify defect-free windows.

1.7 Thesis Structure

The remainder of this report is organized as follows. Chapter **2** presents the detailed methodology used to derive closed-form solutions for the laser source shapes studied. This chapter also describes the semi-analytical thermal model, which is built on the superposition principle.

Chapter **3** details the simulation setup, including material properties, geometric specifications, and process parameters. The single-track simulation cases considered for the different source shapes are given boundary-condition enforcement for each source is verified, followed by an evaluation of the computed temperature fields.

Chapter **4** gives an overview of how the process maps are built and the workflow used to generate them. It first reports the steady-state melt-pool width and depth for a range of power–velocity settings. Next, it compares melt-pool shapes across different laser source profiles. Finally, it assembles the power–velocity (PV) maps and classifies operating points into lack-of-fusion or keyholing, identifying the corresponding defect boundaries.

Finally, Chapter **5** summarizes the main findings and contributions of this work, and outlines directions for future research.

2 Methodology

This section outlines the methodology used to achieve the research objectives. It provides a detailed explanation of the approaches and tools applied to ensure that the results are systematic, consistent, and reliable. A semi-analytical method is employed to simulate the Laser Powder Bed Fusion (L-PBF) process and to obtain the corresponding temperature transients. These temperature data are then used to determine the melt pool dimensions, which serve as the foundation for developing the process maps.

2.1 Governing Heat Conduction Equation for Thermal Problem

In the L-PBF process, consider a 3D cubic body as shown in the Figure 2.1. At time $t = 0$, the body V and its surface ∂V have already been built and are surrounded by the powder bed, with a new powder layer deposited on top. The lateral surface ∂V_{lat} and the top surface ∂V_{top} are in contact with the powder, while the bottom surface ∂V_{bot} is attached to the base plate. The origin of the coordinate system is located such that ∂V_{bot} corresponds to $x_1 - x_2$ plane. At this stage, a laser beam begins scanning the top surface of the powder bed with a predefined pattern, and energy is transferred into the body through the laser beam which further leads to conduction. The resulting temperature rise in the body is given according to the following heat equation:

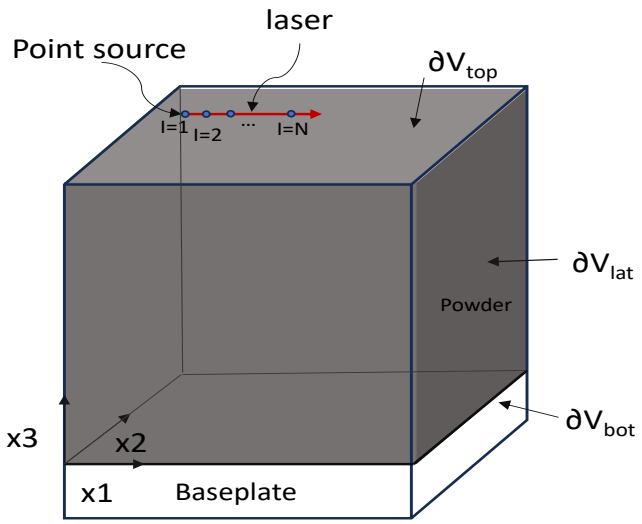

Figure 2.1: Body V submerged into the powder bed where it is bonded to the base plate at ∂V_{bot} and laser scanning is applied on the uppermost layer of powder.

$$\rho c_p \frac{\partial T}{\partial t} = \nabla \cdot (k \nabla T) + Q, \qquad \text{in } V \tag{2.1}$$

where T denotes the temperature, Q is the volumetric heat generation term, ρ is the density, c_p is the specific heat capacity at constant pressure, and k is the thermal conductivity. In the above equation, the properties are temperature dependent. To formulate a well defined thermal boundary problem, the following boundary conditions are prescribed on the domain boundary ∂V, which consists of top, lateral and bottom surfaces, $\partial V = \partial V_{top} \cup \partial V_{lat} \cup \partial V_{bot}$ A zero heat flux (Neumann) condition is imposed on ∂V_{lat} and ∂V_{top} surfaces, representing adiabatic boundaries where no heat transfer occurs normal to the surface. Furthermore, during Laser powder bed fusion processes the base plate is typically maintained at a constant temperature. Taking this into account, a prescribed temperature (Dirichlet) boundary condition is imposed on the bottom surface ∂V_{bot} that is bonded to the base plate. The resulting boundary conditions are:

$$\frac{\partial T}{\partial \mathbf{x}} \cdot \mathbf{n} = 0 \quad \text{on } \partial V_{lat}, \tag{2.2}$$

$$\frac{\partial T}{\partial \mathbf{x}} \cdot \mathbf{m} = 0 \quad \text{on } \partial V_{top}, \tag{2.3}$$

$$T = T_c \quad \text{on } \partial V_{bot}, \tag{2.4}$$

where $\mathbf{n}$ and $\mathbf{m}$ are the components of the outward-facing normal vectors on ∂V_{lat} and ∂V_{top}, respectively, and T_c is the prescribed base plate temperature. This combination of boundary conditions reflects typical L-PBF operating conditions, where heat losses through radiation or convection from the powder surface are negligible compared to the dominant conductive heat transfer within the substrate.

2.1.1 Assumptions and Simplifications

Several assumptions and simplifications are introduced to make the heat conduction problem tractable. First, the governing equation is linearized by treating the thermal properties as temperature-independent. Heat losses due to convection and radiation are neglected, as they are considered insignificant compared to conduction. During phase changes, the latent heat absorbed during melting is assumed to be instantaneously released upon solidification, occurring over a short time interval. Therefore, the net energy contribution of the melting-solidification cycle is considered negligible, and latent heat effects are excluded from the model. For heat absorption, the uppermost powder layer is omitted. It is assumed that the laser energy is directly absorbed at the top surface of the solid body, ∂V_{top}. This removes the need for geometry updates during simulation and significantly improves computational efficiency. With these assumptions, the original non-linear heat equation, given by Equation 2.1 is approximated by the following linear form, which remains valid provided that suitable thermal parameters are chosen:

$$\frac{\partial T}{\partial t} = \alpha \nabla^2 T + \frac{Q}{\rho c_p}, \tag{2.2}$$

where $\alpha = \frac{k}{\rho\, c_p}$ is the thermal diffusivity.

2.2 Semi-Analytical Method

Yang et al. [6] proposed a semi-analytical model for modelling the thermal evolution of a body during L-PBF process in a highly computationally efficient manner. The method also facilitates the subsequent evaluation of thermally induced residual stresses and deformations in L-PBF parts. The framework couples an analytical solution, $\tilde{T}$, which captures the steep thermal gradients associated with the laser heat source, with a numerical correction field, $\hat{T}$, that enforces the boundary conditions within the domain. In this framework, the analytical solution represents the temperature field of point heat sources in a semi-infinite medium, while the numerical component provides the necessary correction to satisfy boundary constraints. Even with simplifications, direct numerical solution of the full boundary-value problem remains computationally intractable due to the significant mismatch in length scales between the laser spot size, typically $10-50$ μm and the overall part dimensions, which are on the order of $10-100$ mm. To overcome this, Yang et al. [6] simplified the transient heat equation by neglecting the temperature dependence of the thermal properties and linearizing the heat conduction, given by Equation 2.2. The laser scanning vector is then discretized into a sequence of point heat sources along the scanning path, as shown in Figure 2.1. The laser scanning vector is approximated by a finite number of point heat sources indexed by N, where $N = 1, \ldots, N$. A point source I is introduced at time $t_0^{(I)}$, while the subsequent source $I+1$ is created at $t_0^{(I+1)} = t_0^{(I)} + \Delta t$, with Δt representing the temporal step size for time integration. The predefined scanning pattern specifies the position of each point source, and successive sources are spaced by $v\Delta t$, where v is the laser scanning speed. This discretization transforms the continuously moving heat input into a temporally and spatially manageable formulation.
Since, Equation 2.2 is linear, the principle of superposition can be applied to efficiently compute the transient temperature field. The model employs the superposition principle to describe the temperature distribution accurately while considering boundary conditions numerically Figure 2.2.

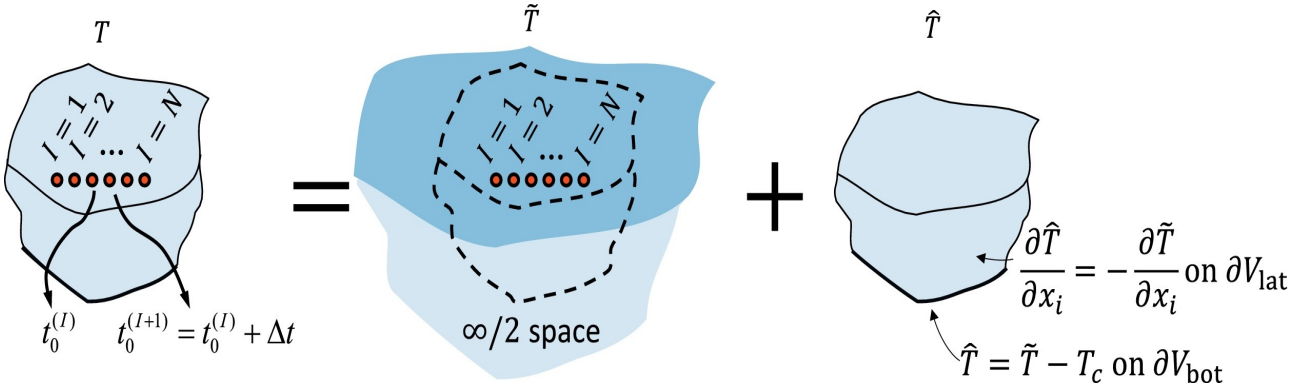

Figure 2.2: Decomposition of the temperature field into $\tilde{T}$ which accounts for N point heat sources, and $\hat{T}$, without the heat sources and accounts for the boundary conditions. Reproduced from [6].

The approach combines the analytical solutions for point sources in semi-infinite space with numerical corrections to enforce boundary conditions. This method efficiently captures steep temperature gradients near the laser and provides insights into thermal effects on part deformation and stress. This model is then solved by applying the superposition principle, which decompose the temperature field T as given below

$$T = \tilde{T} + \hat{T}, \tag{2.3}$$

where:

- $\tilde{T}$: Analytical Temperature field due to N point heat sources in a semi-infinite domain, each of them created at different time instants depending on the scanning history.
- $\hat{T}$: Numerical correction field accounts for the finite dimensions of the powder bed and the associated boundary conditions.

The analytical temperature field $\tilde{T}$ is determined analytically as

$$\tilde{T}(x_i, t) = \sum_{I=1}^{M} \tilde{T}^{(I)}(x_i, t) \quad \text{for } t > t_0^{(M)} \text{ and } M \leq N, \tag{2.4}$$

where,

$$\tilde{T}^{(I)}(x_i, t) = \frac{Q^{(I)} A}{4\rho c_p \left(\pi\alpha \left(t - t_0^{(I)}\right)\right)^{3/2}} \exp\left(-\frac{\left(R^{(I)}\right)^2}{4\alpha\left(t - t_0^{(I)}\right)}\right). \tag{2.5}$$

The energy associated with the source I is represented by $Q^{(I)}$. When the time step Δt is very small $Q^{(I)} = P\Delta t$, where P is the power of the laser beam in watts (W). Moreover, $R^{(I)}$ is the distance between the material point of interest x_i and the position of the source $x_i^{(I)}$, which is given by:

$$\left(R^{(I)}\right)^2 = \left(x_1 - x_1^{(I)}\right)^2 + \left(x_2 - x_2^{(I)}\right)^2 + \left(x_3 - x_3^{(I)}\right)^2. \tag{2.6}$$

For $t \geq t_0^{(I)}$, Equation 2.5 represents the analytical solution of the linear heat equation for a point source I in a semi-infinite medium bounded by the top surface ∂V_{top}. If $t < t_0^{(I)}$, $\tilde{T}^{(I)}(x_i) = 0$ and the solution is defined in the temporal domain. It is noted that Equation 2.5 becomes singular when $t = t_0^{(I)}$. Physically, this occurs because the point source formulation assumes an instantaneous release of energy at a single point. In reality, the laser beam has a finite radius r, over which energy is distributed. To account for this, Yang et al [6] introduced a time shift corresponding to the diffusion time over a distance r, given by

$$\tau_0^{(I)} = t_0^{(I)} - \frac{r^2}{8\alpha}. \tag{2.7}$$

Replacing $\tau_0^{(I)}$ by $t_0^{(I)}$ in Equation 2.5.

$$\tilde{T}^{(I)}(x_i, t) = \frac{Q^{(I)} A}{4\rho c_p \left(\pi\alpha \left(t - \tau_0^{(I)}\right)\right)^{3/2}} \exp\left(-\frac{\left(R^{(I)}\right)^2}{4\alpha\left(t - \tau_0^{(I)}\right)}\right) \tag{2.8}$$

where the term $t - \tau_0^{(I)}$ in the Equation 2.8, becomes $t - t_0^{(I)} + \frac{r^2}{8\alpha}$, where the term $\frac{r^2}{8\alpha}$ eliminates the singularity as t approaches $t_0^{(I)}$. This modification eliminates the mathematical singularity. While $\tilde{T}$ accurately describes the heat diffusio from each point source, it does not satisfy the thermal boundary conditions imposed by the finite geometry of the powder bed. Therefore, a complementary correction field $\hat{T}$ is introduced such that the total temperature field is given as from Equation 2.3. The correction field satisfies the homogeneous transient heat equation:

$$\frac{\partial \hat{T}}{\partial t} = \alpha \nabla^2 \hat{T}, \quad \text{in } V, \tag{2.9}$$

subjected to the boundary conditions:

$$\hat{T} = T_c - \tilde{T}, \quad \text{on } \partial V_{\text{bot}}, \tag{2.10}$$

$$\frac{\partial \hat{T}}{\partial x_i} m_i = -\frac{\partial \tilde{T}}{\partial x_i} m_i, \quad \text{on } \partial V_{\text{lat}}, \tag{2.11}$$

$$\frac{\partial \hat{T}}{\partial x_i} n_i = -\frac{\partial \tilde{T}}{\partial x_i} n_i, \quad \text{on } \partial V_{\text{top}}, \tag{2.12}$$

where $\mathbf{n_i}$ and $\mathbf{m_i}$ denote the components of the outward-facing normal vectors to the lateral ∂V_{lat} and top ∂V_{top} boundaries, respectively. T_c is the prescribed base plate temperature. The temperature gradients of $\tilde{T}$ in Equations (2.11) and (2.12), i.e., $\frac{\partial \tilde{T}}{\partial x} \cdot \mathbf{n}$ and $\frac{\partial \tilde{T}}{\partial x} \cdot \mathbf{m}$, are known since they can be obtained analytically from the derivatives of the Equation 2.8. The boundary condition of no heat flux on ∂V_{top} is already implicit in the solution of $\tilde{T}$. Therefore, the term $\frac{\partial \tilde{T}}{\partial x} \cdot \mathbf{m}$ in Equation 2.12 becomes zero, and Equation 2.12 can be rewritten as:

$$\frac{\partial \hat{T}}{\partial x} \cdot \mathbf{m} = 0 \quad \text{on } \partial V_{top}. \tag{2.13}$$

2.3 Analytical Formulations for Different Heat Source Shapes

The analytical temperature field equations for different source shapes have been derived using different techniques and mathematical tools. Solutions for two cases, 2D circular Gaussian and Top-Hat Square, are presented in this section which are used for calculating the total temperature distribution. The gradients for implementing the numerical correction fields are also calculated by utilizing these formulations. The primary difference between the intensity distributions, namely, top-hat and Gaussian is given below:

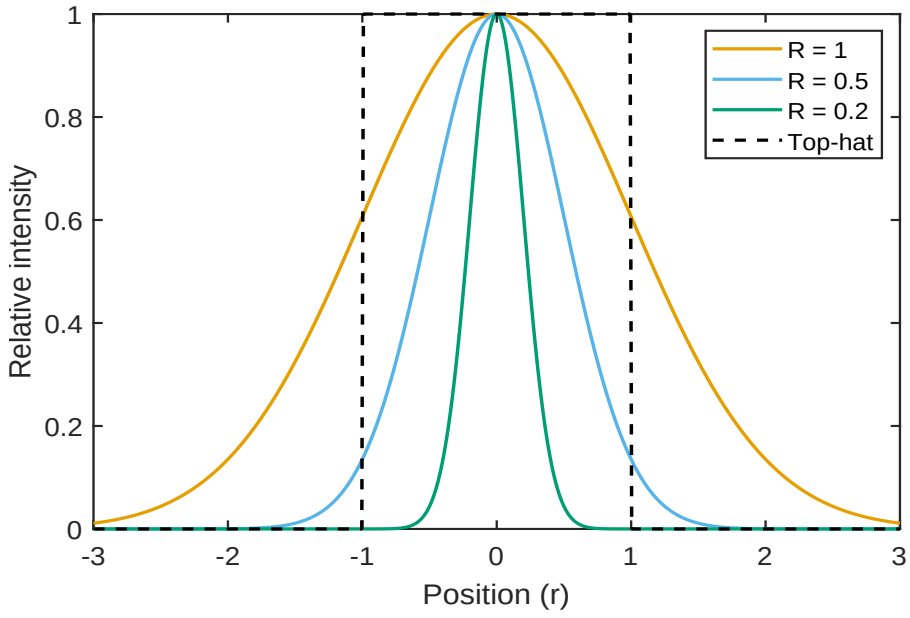

Figure 2.3: Comparison of heat source intensity distributions for Gaussian beams with different standard deviations and a uniform top-hat beam.

Figure 2.3 illustrates the intensity distributions of Gaussian heat sources with different standard deviations ($R = 1.0, 0.5, 0.2$) and a top-hat (uniform) distribution. Smaller R values correspond to narrower, more localized energy distributions. In contrast, the top-hat beam maintains uniform intensity within its spot size and exhibits a sharp cutoff at the edges. Mathematically, as the Gaussian Radius R approaches zero, the profile approaches a spatial Dirac delta function, representing a point-like energy deposition. However, in practice while modelling a physical point source, a small temporal offset is applied to prevent singularities and to represent the finite laser interaction time which ensure physical and numerical stability.

2.3.1 Point Source Formulation

The first baseline case is considered for the point source in a semi infinite domain. The time evolution of the temperature field is then directly predicted and is given by:

$$T^{(I)}(x,t) = \frac{P\,\Delta t}{4\rho c_p\,(\pi\alpha)^{3/2}} \frac{\exp\left(-\frac{\left(R^{(I)}\right)^2}{4\alpha\,(t-\tau_0^{(I)})}\right)}{(t-\tau_0^{(I)})^{3/2}}, \tag{2.14}$$

where P is the lser power, Δt is the time increment, ρ is the material density, c_p is the specific heat capacity and, $\alpha = \frac{k}{\rho\, c_p}$ the thermal diffusivity. The term $R^{(I)}$ denotes the spatial distance from the point source to the observation point. This formulation assumes a homogenous and isotropic material with thermal properties independent of the temperature. The semi-infinite domain assumption implies that boundary effects are neglected and the heat conduction extends infinitely away from the source. The exponential term governs the radial decay of the temperature field, while the prefactor $(t-\tau_0^I)^{-3/2}$ reflects the temporal diffusion behaviour.

2.3.2 Analytical formulation for 2D Circular Gaussian Source

In this section, the derivation for the 2D circular Gaussian source is presented. The laser beam is modeled as a circular spot with Gaussian intensity distribution. The laser heat flux is applied over the surface $z = 0$, where the absorbed energy decays radially with the beam radius R. The material is treated as a semi-infinite solid and the absorbed surface heat flux at a point (x', y') is defined as:

$$q(x', y') = \frac{2\,A\,P}{\pi R^2} \exp\left(-\frac{2(x'^2 + y'^2)}{R^2}\right) \tag{2.15}$$

where P is the laser power (W), A is the laser absorption rate of the powder material, and R is the radius of the laser beam. A schematic representation of the Gaussian laser beam geometry is shown in Figure 2.4.

The solution for the temperature field of a 2D circular Gaussian in a semi-infinite body is evaluated by utilizing the Green's function solution of the transient heat conduction equation for a semi-infinite domain [30]. The Green's function represent the temperature response at a point (x, y, x) and time t due to an instantaneous point heat source applied at position (x', y', z') and time t'. The detailed mathematical formulation of this Green's function is provided in Appendix A.1. Accordingly, the temperature rise dT at (x, y, x) and at time t due to an infinitesimal energy input dQ applied at (x', y', z') and time t' is expressed as:

$$dT(x, y, z, t') = \frac{dQ}{\rho\, c\,(4\,\pi\,\alpha(t-t'))^{3/2}} \exp\left(-\frac{(x-x')^2 + (y-y')^2 + (z-z')^2}{4\alpha(t-t')}\right) \tag{2.16}$$

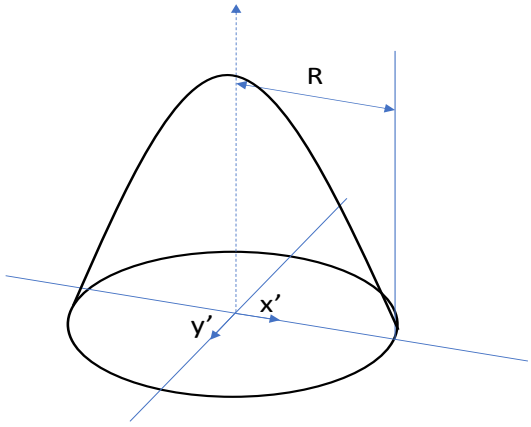

Figure 2.4: Schema for laser-beam heat source models for a circular 2D Gaussian.

where ρ is the density (kg/m^3), dQ = instantaneous heat generated, c = specific heat capacity (J/kg K), $\alpha = k/\rho\, c$ is the thermal diffusivity. Here, t' denotes the time of heat deposition and $t - t'$ represents the elapsed time for thermal diffusion, k = thermal conductivity.
The corresponding schematic of the circular Gaussian laser-beam geometry, including the coordinate system and surface heat flux distribution, is shown in Figure 2.4. The total energy absorbed over a differential area $dx'dy'$ during a short time interval Δt is given by:

$$dQ = q(x', y')\, \Delta t\, dx'dy' = \frac{2AP\, \Delta t}{\pi R^2} \exp\left(-\frac{2(x'^2 + y'^2)}{R^2}\right) dx'dy'. \tag{2.17}$$

Substituting the above Equation 2.17 in Equation 2.16 due to all infinitesimal surface elements can be written as:

$$T(x, y, z, t) - T_o = \frac{2\, A\, P\, \Delta t}{\pi R^2\, \rho c (4\pi\alpha(t - t'))^{3/2}} \int_{-\infty}^{\infty}\int_{-\infty}^{\infty} \exp\left(-\frac{-2(x'^2 + y^2)}{R^2}\right) \exp\left(-\frac{(x - x')^2 + (y - y')^2 + z^2}{4\alpha(t - t')}\right) dx'dy' \tag{2.18}$$

Where T_o is initial temperature. The integration bounds ($-\infty$ to $+\infty$) in the x' and y' directions are selected because the Gaussian distribution decays rapidly, becoming negligible beyond approximately $\pm 3\sigma$, where σ is the standard deviation associated with the radius R. These limits are used to formally account for the entire spatial domain influenced by the heat source, although in practice most of the heat intensity is confined within a few multiples of σ. The other reason also involves the mathematical simplicity and ease of attaining the closed-form solutions. Next we can rearrange the equations in such a way so as to able to solve it through Gaussian Convulation method, more details in Appendix A.2. This double integral is of the standard Gaussian convulation form. It evaluates to:

$$T(x,y,z,t) - T_o = \frac{2\,A\,P\,\Delta t}{\pi R^2\,4\,\rho c\,(\pi\alpha(t-t'))^{3/2}} \exp\left(-\frac{z^2}{4\alpha(t-t')}\right) \int_{-\infty}^{\infty}\int_{-\infty}^{\infty} \exp\left(-\frac{2x'^2}{R^2} - \frac{(x-x')^2}{4\alpha(t-t')}\right) \exp\left(-\frac{2y'^2}{R^2} - \frac{(y-y')^2}{4\alpha(t-t')}\right) dx'\,dy' \tag{2.19}$$

Now, further arranging them accordingly to factorize, we get the following:

$$a = \frac{2}{R^2}, \quad b = \frac{1}{4\alpha(t-t')}$$

$$a + b = \frac{2}{R^2} + \frac{1}{4\,\alpha(t-t')} = \frac{8\,\alpha(t-t') + R^2}{R^2 4\,\alpha\,(t-t')} \tag{2.20}$$

$$ab = \frac{2}{R^2}\frac{1}{4\alpha(t-t')} = \frac{1}{2\,R^2\,\alpha\,(t-t')} \tag{2.21}$$

Finally, the integral takes up the form as:

$$\begin{aligned} I &= \left(\sqrt{\frac{\pi}{a+b}} \exp\left(-\frac{a\,b}{a+b}x^2\right)\right)\left(\sqrt{\frac{\pi}{a+b}} \exp\left(-\frac{a\,b}{a+b}y^2\right)\right) \\ &= \frac{\pi}{a+b} \exp\left(-\frac{a\,b}{a+b}(x^2+y^2)\right) \end{aligned} \tag{2.22}$$

Putting the expressions obtained above in Equation 2.20 and 2.21 in Equation 2.22, we obtain the complete temperature field expression for the 2D circular Gaussian source, given by the Equation 2.23.

$$T = \frac{P\,A\,\Delta t}{\rho c\,\pi^{3/2}(4\alpha(t-t') + R^2)\sqrt{\alpha\,(t-t')}} \exp\left(-\frac{(x^2+y^2)}{4\,\alpha\,(t-t') + R^2} - \frac{z^2}{4\alpha(t-t')}\right) \tag{2.23}$$

where P is the laser power (W), A is the laser absorption rate of the powder material, and R is the radius of the laser beam and the dimension of the circular source considered.
To ensure the validity of the derived solution, a limiting case is evaluated. Specifically, the distribution parameter R is reduced to zero, i.e., $\lim_{R\to 0}$, to check whether the solution converges to the well-known point-source solution. If this condition holds, it confirms the correctness of the formulation. The limit was computed using Mathematica, yielding the following expression:

$$\lim_{R\to 0} T = \frac{P\,A\,\Delta t}{\rho c_p\,\pi^{3/2}\left(4\alpha(t-t') + R^2\right)\sqrt{\alpha(t-t')}} \exp\left(-\frac{x^2+y^2}{4\alpha(t-t') + R^2} - \frac{z^2}{4\alpha(t-t')}\right). \tag{2.24}$$

As $R \to 0$, this expression simplifies to the classical point-source solution of the heat equation:

$$T = \frac{P\,A\,\Delta t}{4\,\rho\,c_p\left(\pi\alpha(t-t')\right)^{3/2}} \exp\left(-\frac{x^2+y^2+z^2}{4\alpha(t-t')}\right). \tag{2.25}$$

This confirms that the derived formulation is consistent with the established analytical solution for a point heat source in a semi-infinite medium.

Furthermore, a stationary heat source was considered with a pulse duration of 5×10^{-5} s, representing the short time interval during which the laser remains active and delivers energy to the substrate. Figure 2.5 illustrates the temperature evolution for the stationary circular source at different time instants. As shown in Figure 2.5a, a sharp and intense Gaussian hot spot is observed at the center at 1 μs. In the subsequent frames (Figures 2.5b and 2.5c), a gradual reduction in the peak temperature is evident, indicating the onset and progression of heat conduction within the material.

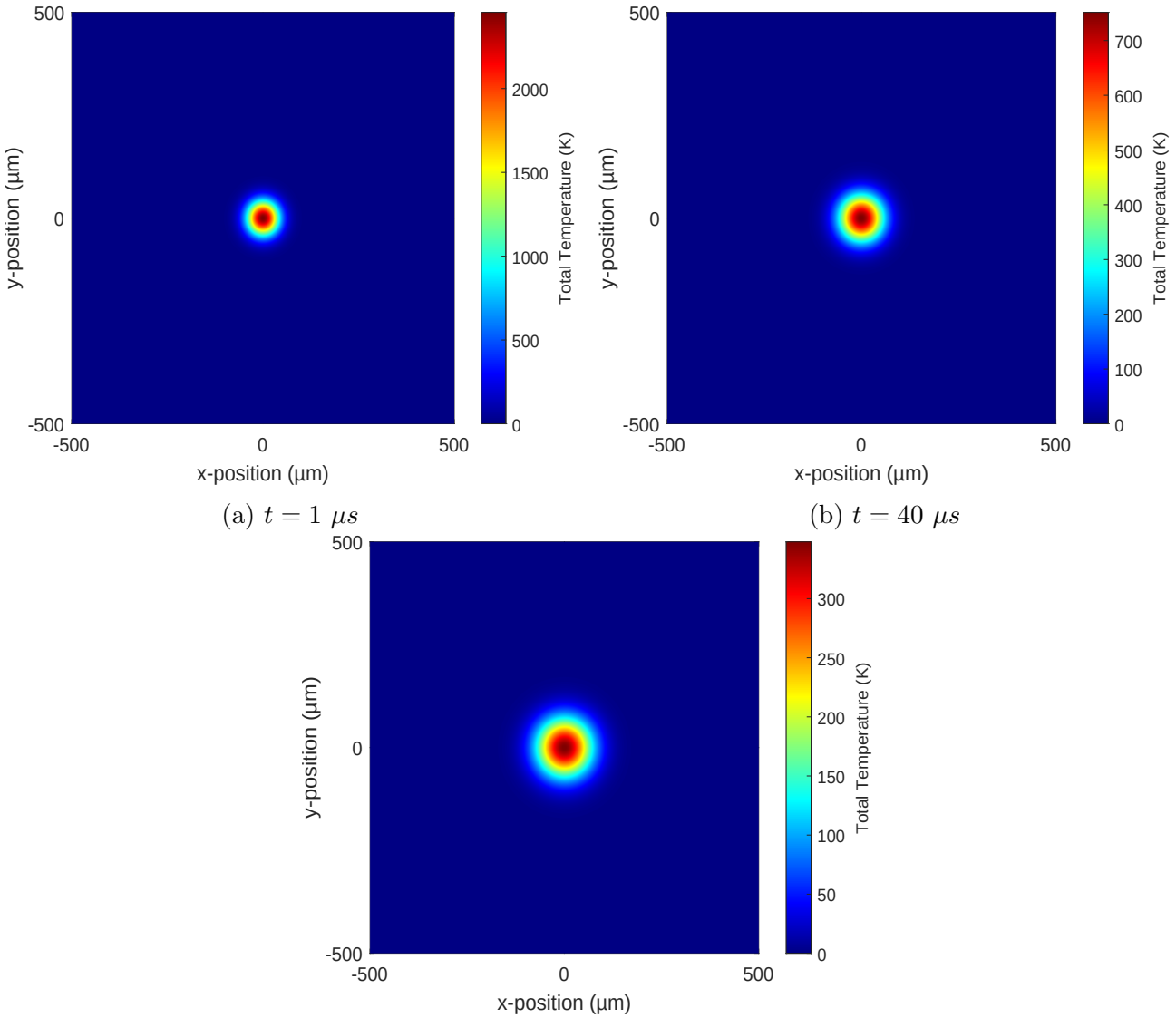

(a) $t = 1\ \mu s$ (b) $t = 40\ \mu s$

(c) $t = 90\ \mu s$

Figure 2.5: Simulated temperature distribution of a stationary 2D circular Gaussian heat source with a spot size of 35 μm, $P = 35$W on the surface of Ti-6Al-4V at different times after an instantaneous pulse: (a) $t = 1$ μs, (b) $t = 40$ μs, and (c) $t = 90$ μs.

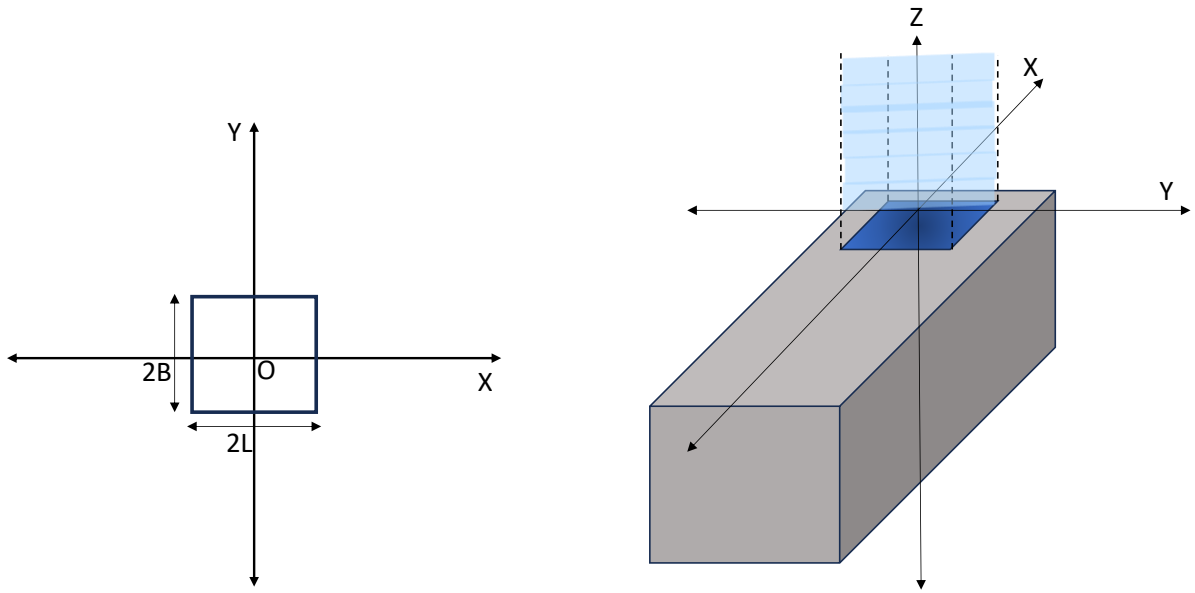

Figure 2.6: Schema for laser-beam heat source model for a uniform intensity square source, where 2L and 2B are representative of the dimensions of the square source.

2.3.3 Analytical Formulation for Uniform intensity (Top-Hat) Square Heat Source

A top-hat, or uniform-intensity, laser beam provides a constant energy flux per unit area across its entire cross-section. As a result, the intensity profile appears uniform when viewed along the beam axis. The following derivation presents the closed-form analytical solution for a square top-hat source, beginning from the instantaneous point heat source formulation given in Equation 2.26.

$$dT(x,y,z,t) = \frac{dQ}{\rho\, c\, (4\,\pi\,\alpha(t-t'))^{3/2}} \exp\left(-\frac{(x-x')^2+(y-y')^2+(z-z')^2}{4\alpha(t-t')}\right) \tag{2.26}$$

To extend the formulation to a uniform-intensity square source, the instantaneous point heat source solution is integrated over the area defined by the square beam profile. In this case, the source is assumed to have dimensions $2L$ and $2B$, as illustrated in Figure 2.6. Accordingly, the limits of integration for x' and y' are taken as $-l < x' < l$ (length) and $-b < y' < b$ (breadth). The source is applied on the surface of the material, hence $z' = 0$. The heat intensity is expressed as $q(x', y') = P/A$, where P is the applied power and $A = 4 \times l \times b$ represents the area of the source.

For the square heat source, the corresponding temperature distribution is obtained from the following double integral:

$$T(x,y,z,t) - T_o = \frac{P\,A\,\Delta t}{4\,b\,l\,\rho\,c_p\,(4\pi\alpha(t-t_0))^{3/2}} \int_{-l}^{l}\int_{-b}^{b} \exp\left(-\frac{(x-x')^2+(y-y')^2+z^2}{4\alpha(t-t_0)}\right) dx'\,dy'$$
$$\text{for } t \geq t_0,\ \alpha > 0,\ l > 0,\ b > 0,\ x, y \in \mathbb{R}. \tag{2.27}$$

It can further be written as:

$$T(x,y,z,t) - T_0 = \frac{P\,A\,\Delta t}{4\,b\,l\,\rho\,c_p\,[4\pi\alpha(t-t_0)]^{3/2}} \exp\left(-\frac{z^2}{4\alpha(t-t_0)}\right) \int_{-l}^{l} \exp\left(-\frac{(x-x')^2}{4\alpha(t-t_0)}\right) dx' \int_{-b}^{b} \exp\left(-\frac{(y-y')^2}{4\alpha(t-t_0)}\right) dy', \quad \text{for } t \geq t_0,\ \alpha > 0,\ l > 0,\ b > 0,\ x, y \in \mathbb{R}. \tag{2.28}$$

Evaluating this integral in *Mathematica* yields the following closed-form expression:

$$T(x,y,z,t) = \frac{P\,A\,\Delta t}{4\,(\pi\alpha)^{3/2}\,\rho c_p\,4\,l\,b} \frac{\alpha\pi\,\exp\left(-\frac{z^2}{4\alpha(t-t_0)}\right)}{\sqrt{t-t_0}} \left[\operatorname{erf}\left(\frac{l-x}{2\sqrt{\alpha(t-t_0)}}\right) + \operatorname{erf}\left(\frac{l+x}{\sqrt{4\alpha(t-t_0)}}\right)\right] \left[\operatorname{erf}\left(\frac{b-y}{2\sqrt{\alpha(t-t_0)}}\right) + \operatorname{erf}\left(\frac{b+y}{\sqrt{4\alpha(t-t_0)}}\right)\right] \tag{2.29}$$

Here, $\operatorname{erf}(x)$ represents the error function (see Appendix A.3), while P, A, and α denote the laser power, absorptivity, and thermal diffusivity, respectively. The appearance of the error functions in the final expression results from the integration of the fundamental solution of the heat conduction equation over the finite dimensions of the square laser source. These functions represent the cumulative thermal effect over the bounded region. Similar to the 2D circular Gaussian case, the consistency of the square source formulation are confirmed by evaluating its limiting behavior as $l \to 0$ and $b \to 0$.

$$\begin{aligned}\lim_{l\to 0,\ b\to 0} T(x,y,z,t) &= \frac{P\,A\,\Delta t}{4\,l\,b\,4\,(\pi\alpha)^{3/2}\,\rho c_p} \frac{\alpha\pi\,\exp\left(-\frac{z^2}{4\alpha(t-t_0)}\right)}{\sqrt{t-t_0}} \left[\operatorname{erf}\left(\frac{l-x}{2\sqrt{\alpha(t-t_0)}}\right) + \operatorname{erf}\left(\frac{l+x}{\sqrt{4\alpha(t-t_0)}}\right)\right] \left[\operatorname{erf}\left(\frac{b-y}{2\sqrt{\alpha(t-t_0)}}\right) + \operatorname{erf}\left(\frac{b+y}{\sqrt{4\alpha(t-t_0)}}\right)\right] \\ &= \frac{A\,\Delta t\,P}{4\,\rho\,c_p\,(\pi\alpha\,(t-t_0))^{3/2}} \exp\left(-\frac{x^2+y^2+z^2}{4\alpha(t-t_0)}\right)\end{aligned} \tag{2.30}$$

This confirms that the square heat source model is mathematically consistent, as it reduces correctly to the point-source solution in the limiting case.

Similarly, a stationary square heat source was considered with a pulse duration of 5×10^{-5} s, representing the brief interval during which the laser is active and transfers energy to the substrate. The subsequent time instants following the pulse were analyzed to observe the progression of heat conduction. As shown in Figure 2.7 (a), at 1 μs, the temperature field exhibits a uniform intensity across the entire square region. At this early stage, the temperature distribution is sharply defined and closely follows the geometry of the source, indicating minimal heat diffusion. In the later cases, 2.7 (b) and (c), the heat begins to diffuse into the surrounding material, causing the initially sharp edges of the temperature profile to smooth out and the peak

temperature to decrease as energy spreads. By the third case, a significant reduction in the peak temperature is observed, reflecting the continued dissipation of thermal energy through conduction.

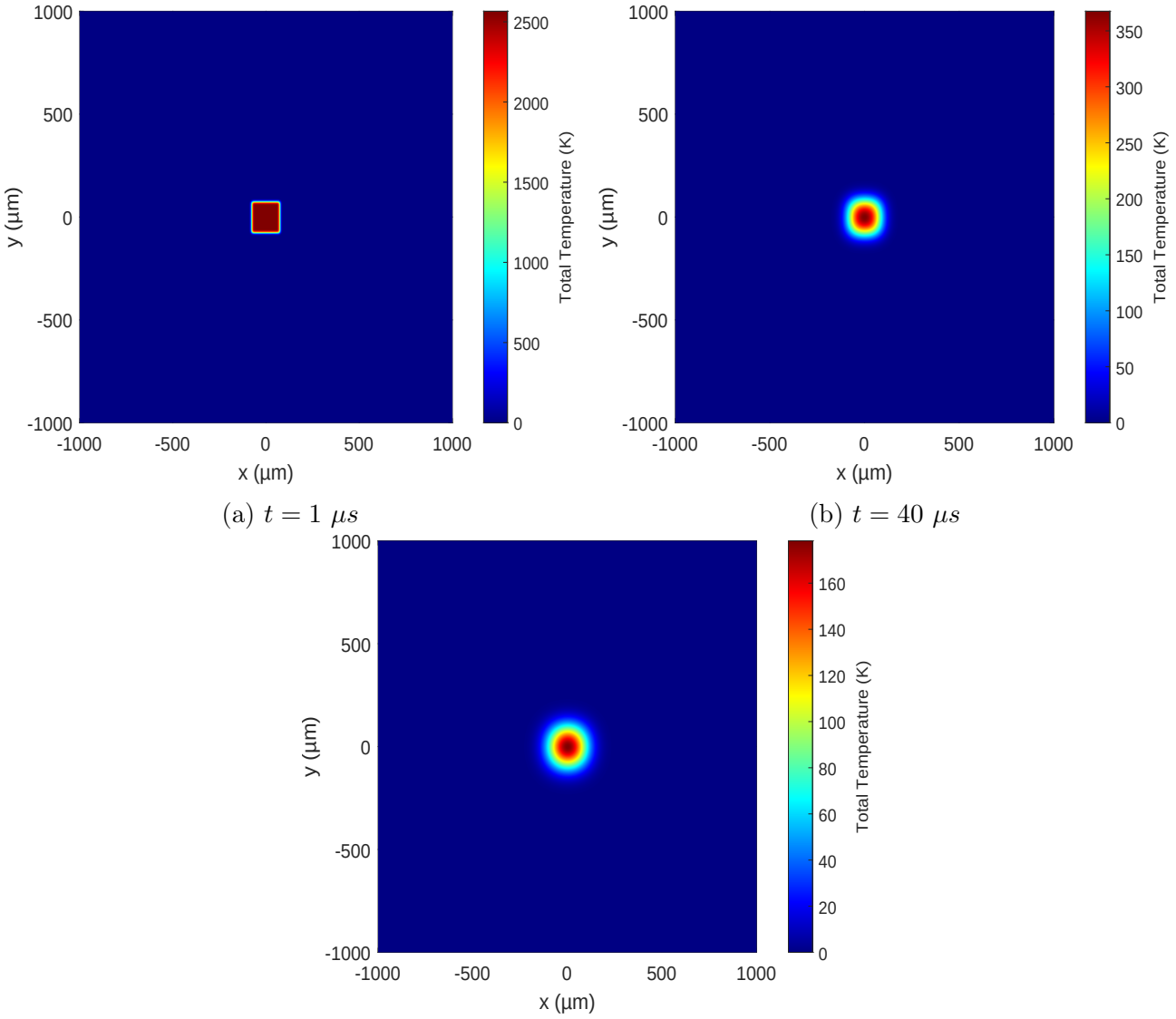

(a) $t = 1\ \mu s$

(b) $t = 40\ \mu s$

(c) $t = 90\ \mu s$

Figure 2.7: Simulated temperature distribution of a square heat source with a spot size of $75\,\mu\text{m} \times 75\,\mu\text{m}$, $P = 35\,\text{W}$ on the surface of Ti-6Al-4V at different times after an instantaneous pulse: (a) $t = 1\ \mu$s, (b) $t = 40\ \mu$s, and (c) $t = 90\ \mu$s.

2.4 Analytical Solutions Convergence

In addition to the mathematical limit calculation, the convergence of the analytical temperature field ($\tilde{T}$) for different source shapes was evaluated in MATLAB by comparing with the point-source solution. The chosen observation point A(1.0,1.0,2.0) mm was selected at the center of the computational domain, sufficiently distant from the boundaries, to ensure an unbiased comparison, as illustrated in Figure 2.8. The convergence analysis was carried out

by systematically reducing the spot size of the distributed sources (square and circular) while comparing their analytical temperature profiles to the reference point-source solution at the same central location. At each step, the temperature field corresponding to the distributed source was plotted alongside the point-source solution at the same spatial location, allowing both visual and quantitative comparison. Convergence was considered achieved when a further reduction in spot size produced negligible differences between the two temperature fields that is when the relative difference between successive profiles fell below 1% in peak temperature and time-dependent response. The specific spot size values reported in Table 2.1 were determined through this iterative calibration process. For the point-source reference of spot size of 50μm was adopted, while the equivalent square and circular sources converged at 30μm and 36μm, respectively. The process and scanning parameters were held constant throughout the analysis. Figure 2.9a compares the temperature distributions for the point source and the uniform-intensity square source, whereas Figure 2.9b shows the comparison between the Gaussian and point-source cases. This systematic, stepwise calibration approach ensures that, in the limit of vanishing spot size, the distributed-source models correctly converge to the analytical point-source solution. Such convergence validates the underlying assumptions of the semi-analytical framework and confirms the physical consistency of the temperature field formulations used in subsequent thermal analyses.

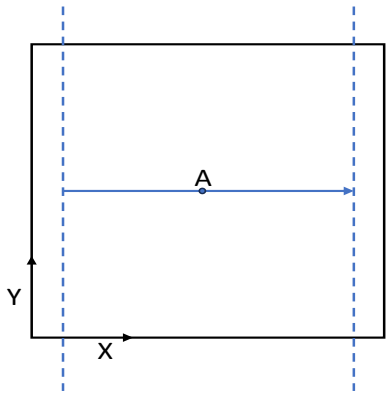

Figure 2.8: Schematic of the top surface of the computational domain, where the moving laser track (blue) and boundary offsets (dotted) are shown. Temperature was monitored at point A(1.0,1.0,2.0 mm).

Table 2.1: Spot sizes for the convergence of Analytical solutions

Source	spot size
Point	50 μm
Uniform intensity square source	30 μm
2D Circular Gaussian	36 μm

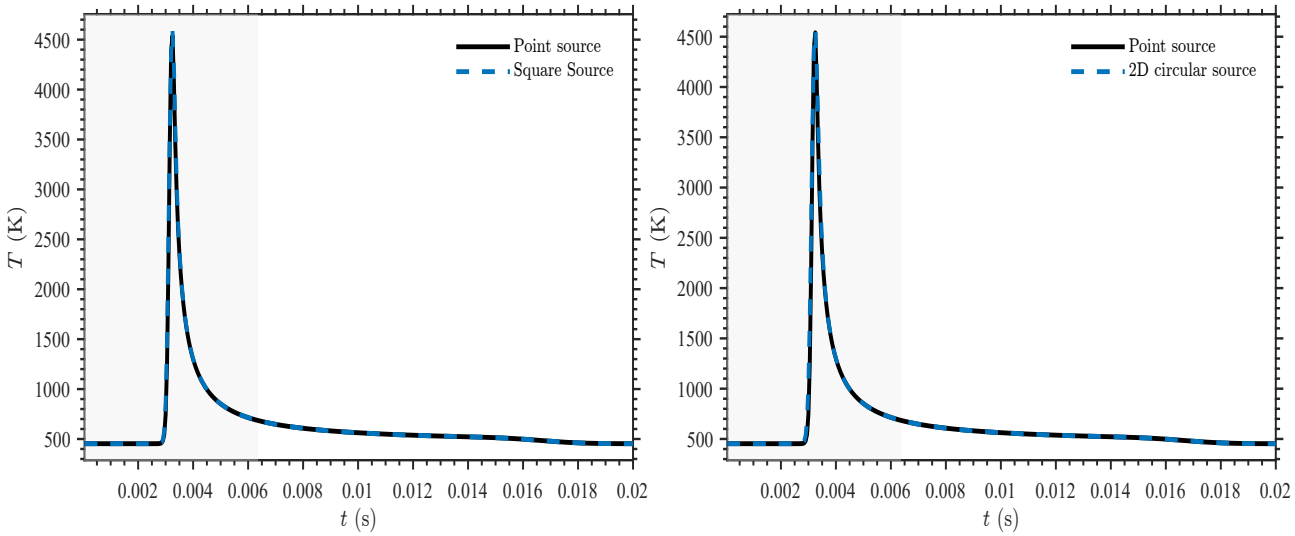

(a) (b)

Figure 2.9: Comparison of analytical temperature fields for two laser source shapes measured at point A. a) Analytical Temperature of 2D circular Gaussian vs point case b) Analytical Temperature of square source vs point case, P = 35 W

2.5 Numerical Correction for Boundary Effects

The analytical formulations derived earlier assume a semi-infinite medium, which has no consideration of the boundary effects. For the incorporation the effects of a finite surface domain, the finite difference (FD) technique is employed. The finite difference method is an effective method to numerically solve the heat equation. The FD method provides a discrete numerical framework to solve the transient heat conduction equation by approximating the spatial and temporal derivatives at nodal points. In this study, a cubic domain size of 2 mm x 2 mm x 2 mm is considered and has been discretized into $40 \times 40 \times 40$ elements corresponding to a spatial resolution of 0.05 mm. To compare the solutions of different source shapes with the known solution of point source in the proposed semi-analytical scheme, the accuracy of the $\hat{T}$ can be analyzed. The boundary conditions imposed in the thermal problem are of the type Dirichlet on ∂V_{bot} and Neumann on ∂V_{lat}. For the points located in ∂V_{bot}, the boundary condition is easily imposed as it is dependent on the temperature of the base plate, T_c. The numerical correction field is then given by $\hat{T} = T_c - \tilde{T}$.

For the implementation of different source shapes within the semi-analytical method, the primary dependency arises from variations in the analytical temperature field $\tilde{T}$. Since the numerical correction field $\hat{T}$ is computed from the gradients of $\tilde{T}$, any change in the source profile directly influences the analytical formulation and its spatial derivatives. The finite-difference scheme and boundary condition enforcement, however, remain identical across all source types: Dirichlet conditions are applied on the base plate, and Neumann (zero-flux) conditions are imposed on all other surfaces through the correction field $\hat{T}$. The gradients of $\tilde{T}$ for each source shape were derived in *Mathematica* and integrated into the boundary condition source terms, ensuring consistency, accuracy, and flexibility of the semi-analytical model across different beam profiles. For the 2D circular Gaussian source, the starting point is the temperature field given in Equation 2.23. Its spatial derivatives are then obtained, as shown in Equations 2.31, 2.32, and 2.33. Similarly, the derivatives for the square source are provided in Equations 2.37, 2.38, and 2.39.

$$\frac{\partial \tilde{T}}{\partial x} = -\frac{2\,x\,P\,A\,\Delta t}{\rho\,c\,\pi^{3/2}\sqrt{(t-t')\alpha}\left(R^2+4\alpha(t-t')\right)^2}\exp\left[-\frac{z^2}{4\alpha(t-t')}-\frac{x^2+y^2}{R^2+4\alpha(t-t')}\right], \tag{2.31}$$

$$\frac{\partial \tilde{T}}{\partial y} = -\frac{2\,y\,P\,A\,\Delta t}{\rho\,c\,\pi^{3/2}\sqrt{(t-t')\alpha}\left(R^2+4\alpha(t-t')\right)^2}\exp\left[-\frac{z^2}{4\alpha(t-t')}-\frac{x^2+y^2}{R^2+4\alpha(t-t')}\right], \tag{2.32}$$

$$\frac{\partial \tilde{T}}{\partial z} = -\frac{P\,A\,z\,\Delta t}{2\,\rho\,c\,\pi^{3/2}\left((t-t')\alpha\right)^{3/2}\left(R^2+4\alpha(t-t_p)\right)}\exp\left[-\frac{z^2}{4\alpha(t-t')}-\frac{x^2+y^2}{R^2+4\alpha(t-t')}\right]. \tag{2.33}$$

Simplifying, Now let $D = (4\alpha(t-t')+R^2)$, the expressions takes up the following form as given by the Equations 2.34, 2.35 and 2.36:

$$\frac{\partial \tilde{T}}{\partial x} = \frac{-2\,x\,T}{D}, \tag{2.34}$$

Similarly, in the y-direction and z-direction it is given as:

$$\frac{\partial \tilde{T}}{\partial y} = \frac{-2\,y\,T}{D}, \tag{2.35}$$

$$\frac{\partial \tilde{T}}{\partial z} = \frac{-z\,T}{2\,\alpha(t-t')} \tag{2.36}$$

where T is the Temperature field equation given by the Equation 2.23.
The derivatives of the square source were obtained in a similar manner, and the results are presented in Equations 2.37, 2.38, and 2.39. The derivative in the x, y and z direction are given as follows:

$$\begin{aligned}\frac{\partial \tilde{T}}{\partial x} = {} & \frac{\sqrt{\alpha}\sqrt{\pi}}{t-t_0}\exp\left(-\frac{2l^2+2x^2+z^2}{4\alpha(t-t_0)}\right) \\ & \left[\exp\left(\frac{(l-x)^2}{4\alpha(t-t_0)}\right)-\exp\left(\frac{(l+x)^2}{4\alpha(t-t_0)}\right)\right] \\ & \left[\operatorname{erf}\left(\frac{b-y}{2\sqrt{\alpha}\sqrt{t-t_0}}\right)+\operatorname{erf}\left(\frac{b+y}{2\sqrt{\alpha}\sqrt{t-t_0}}\right)\right],\end{aligned} \tag{2.37}$$

$$\begin{aligned}\frac{\partial \tilde{T}}{\partial y} = {} & \frac{\sqrt{\alpha}\sqrt{\pi}}{t-t_0}\exp\left(-\frac{2b^2+2y^2+z^2}{4\alpha(t-t_0)}\right) \\ & \left[\exp\left(\frac{(b-y)^2}{4\alpha(t-t_0)}\right)-\exp\left(\frac{(b+y)^2}{4\alpha(t-t_0)}\right)\right] \\ & \left[\operatorname{erf}\left(\frac{l-x}{2\sqrt{\alpha}\sqrt{t-t_0}}\right)+\operatorname{erf}\left(\frac{l+x}{2\sqrt{\alpha}\sqrt{t-t_0}}\right)\right],\end{aligned} \tag{2.38}$$

$$\begin{aligned}\frac{\partial \tilde{T}}{\partial z} = {} & -\frac{\pi z}{2(t-t_0)^{3/2}}\exp\left(-\frac{z^2}{4\alpha(t-t_0)}\right) \\ & \left[\operatorname{erf}\left(\frac{l-x}{2\sqrt{\alpha(t-t_0)}}\right)+\operatorname{erf}\left(\frac{l+x}{2\sqrt{\alpha(t-t_0)}}\right)\right] \\ & \left[\operatorname{erf}\left(\frac{b-y}{2\sqrt{\alpha(t-t_0)}}\right)+\operatorname{erf}\left(\frac{b+y}{2\sqrt{\alpha(t-t_0)}}\right)\right].\end{aligned} \tag{2.39}$$

2.6 Melt Pool Dimension Extraction Methodology

The melt pool has been defined as the connected region in which the predicted temperature field exceeds the alloy's liquidus temperature, i.e., $T \geq T_l$. The main concept behind melt pool measurement is to accurately identify and quantify the physical dimensions of the molten and subsequently solidified material. For Ti-6Al-4V we take $T_l = 1928K$ which is consistent with prior L-PBF thermal modelling study [6]. A single laser scan track can be divided into three regions based on spatial variation of the melt pool track width and height [31], as illustrated in Figure 2.10.

- The initial transient region is typically wider and taller often exhibiting a bump due to laser's initial transition with the powder bed.
- The steady-state region, located in the middle portion of the track where the temperature field and melt pool dimensions stabilize leading to smaller variations in width and height, or almost constant track width and depth.
- The final transient region, near the end of a scan, has a tapered profile with decreasing track width and height.

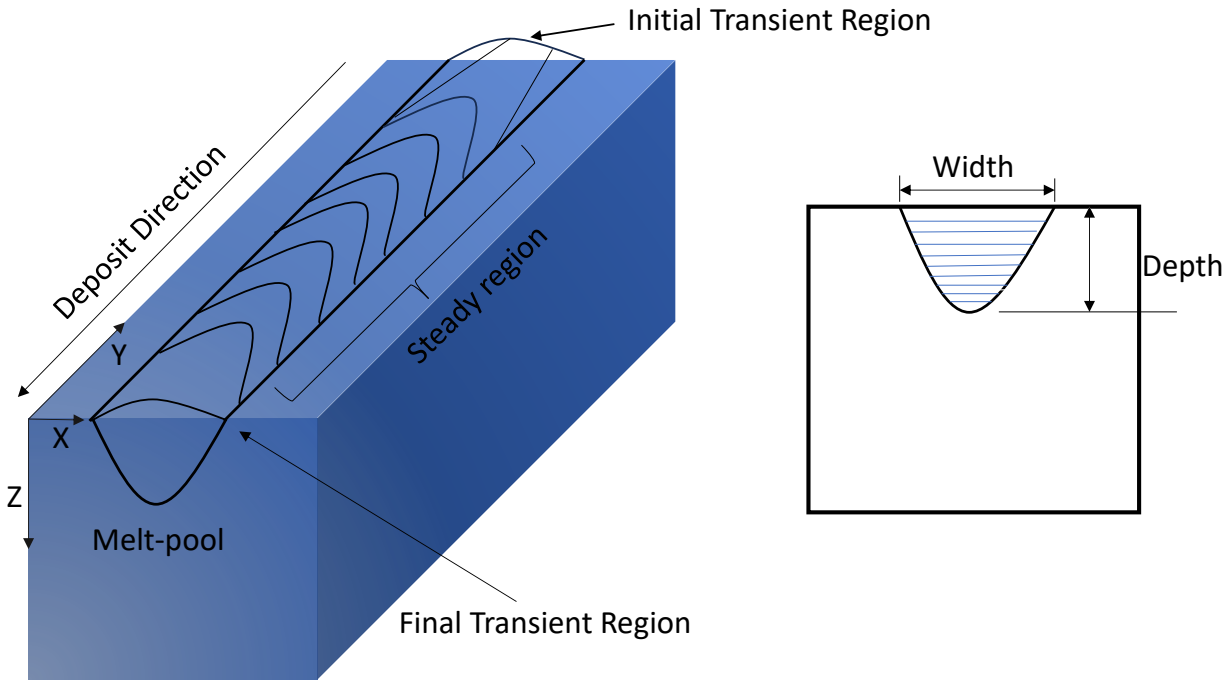

Figure 2.10: Schematic illustration of a single track deposition by the L-PBF process and the melt pool geometry parameters from the cross-section view.

The melt pool width and depth are determined using an isotherm-based method, in which the molten boundary is identified from the liquidus–solidus transition in the computed temperature field. This approach is particularly suited to the present semi-analytical framework, as it provides complete temporal information on the evolving temperature field, enabling the melt

pool to be clearly defined at successive time steps and tracked until steady-state conditions are reached. Moreover, this method ensures consistency with both experimental and numerical investigations reported in [32]. An additional advantage is that the resulting geometric parameters exhibit strong correlations with defect mechanisms such as porosity formation and melt-pool mode transitions.

2.6.1 Width of the melt pool

For single-track deposition, the melt-pool dimensions are determined from the transient temperature field by identifying the $T = T_{\text{melt}}$ isotherm, which delineates the boundary between solid and liquid regions. Lets investigate the case of a point source first to understand how the data is extracted through the semi-analytical method. A cube of dimensions 2 mm x 2 mm x 2 mm is considered. The laser scans the top surface ($z = z_{\text{top}}$), the melt pool width refers to the lateral dimensions of the solidified track or the molten region as viewed from above as shown in Figure 2.11. The white dotted line depicts the boundary of the melt pool. The width represent the span of the molten track in the y-direction at a given scan position.

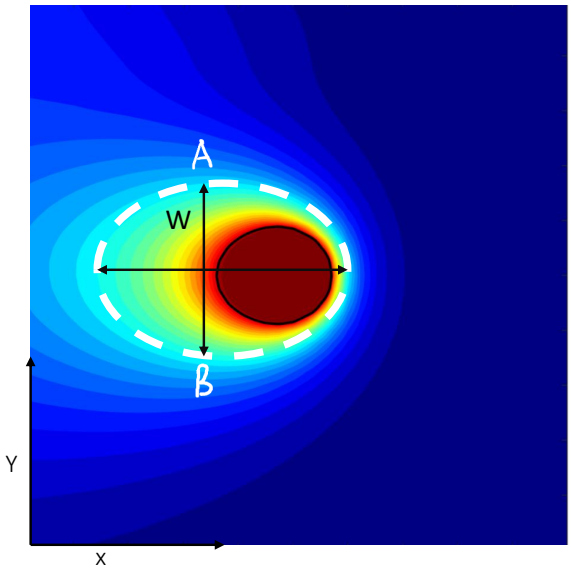

Figure 2.11: Width (W) of the melt pool as seen from the top view. Points A and B are the isotherm intersections.

Let the laser move along the scan direction x from a predefined starting to a predefined end point and at each time step t_k, let the laser center be located at $x_{\text{src}}(k)$. The melt pool width $W(x,t)$ is mathematically defined as:

$$W(x,t) = \max\{\, y :\ T(x,y,z_{\text{top}},t) \geq T_{\text{melt}} \,\} - \min\{\, y :\ T(x,y,z_{\text{top}},t) \geq T_{\text{melt}} \,\}.$$

The x-direction has been discretized by sampling points and then along those points melt pool widths are calculated. Using MATLAB, temperature transients $T(x,y,z,t)$ are computed via a semi-analytical model. For each scan position $x_{\text{src}}(k)$, a scattered linear interpolant reconstruct the temperature profile T(y) along a line at fixed $x = x_{\text{src}}$. The two intersection

points denoted by A and B in Figure 2.11 are identified by linear interpolation. If multiple disconnected segments exist, the widest contiguous span defines $W\big(x_{\mathrm{src}}(k), t_k\big)$.
Plots of melt pool width along the scan direction are generated to assess the variation and identify the steady-state region, where the melt pool width stabilizes with minimal fluctuation. An example for a point-source simulation at P = 200 W and V =1 m/s is shown in Figure 2.12a.

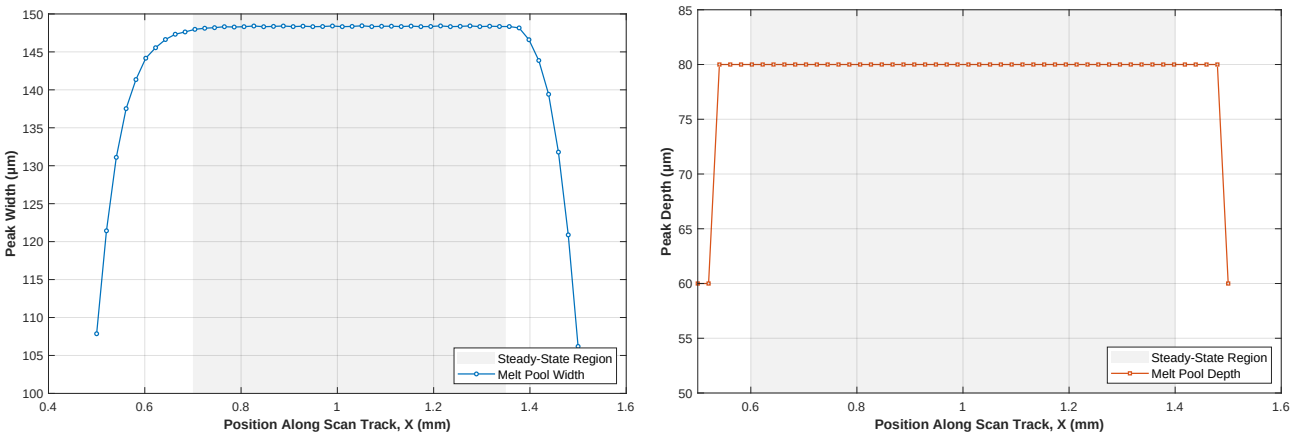

(a) Melt pool width as a function of scan position. (b) Melt pool depth as a function of scan position.

Figure 2.12: Variation of melt pool dimensions with scan position for $P = 200$ W and $V = 1$ m/s, corresponding to a scan range from $x = 0.5$ mm to $x = 1.5$ mm.

2.6.2 Depth of the melt pool

The melt pool depth is defined as the vertical penetration of the molten region below the powder surface, typically measured from the top surface down to the deepest point where temperature exceeds T_{melt}. At a given scan position x_{src} and time t_k, the melt-pool depth is the distance from the top surface to the deepest point of the connected liquid region on a y-z cross-section through the track as depicted in the Figure 2.13 and can be expressed as follows:

$$D(x_{\mathrm{src}}, t_k) \;=\; z_{\mathrm{top}} - \min\Big\{\, z : \; \exists\, y \text{ s.t. } T(x, y, z, t) \geq T_{\mathrm{melt}} \,\Big\}.$$

Computationally, the temperature field is interpolated in three dimensions to capture sub-surface variations. At each scan position $x_{\mathrm{src}}(k)$, a 2D temperature slice is extracted in the y-z plane centered on the laser path. The variation of depth along the scan direction for the same processing conditions is shown in Figure 2.12b. Regions exhibiting minimal deviation in both width and depth are subsequently used to define the steady-state melt pool dimensions, which is discussed in the next subsection.

2.6.3 Steady State criterion

In Laser Powder Bed Fusion (L-PBF), the steady-state criterion refers to a region along the laser scan path where the melt pool dimensions stabilize after an initial transient phase. This regime is characterized by minimal variation in melt pool dimensions over time and scan positions as shown in the spatial 2.12a and 2.12b and time evolution plots given by Figure 2.14, where the width is given by the Figure 2.14a and depth is given by Figure 2.14b. As the laser scan

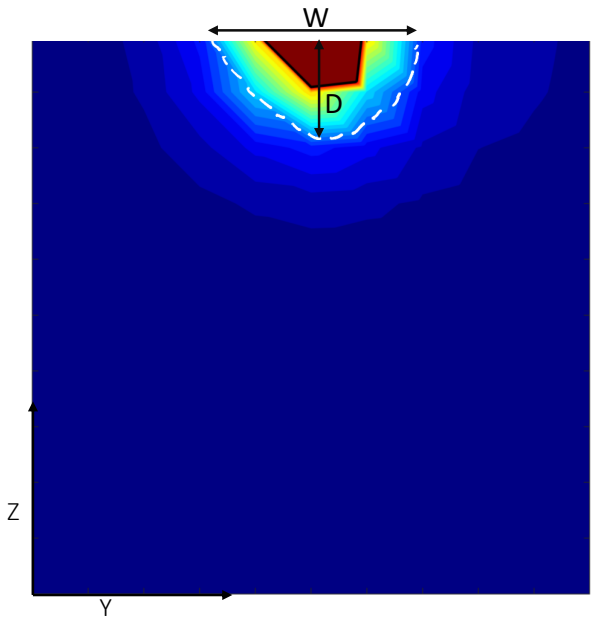

Figure 2.13: Depth as seen from the cross-section view

progresses, the thermal gradient stabilizes, which leads to a steady state [31]. As discussed above, the single-track scans exhibit an initial transient, a steady region and a final transient region. The plots signify that the steady state has been achieved for the prescribed scan direction. The material experiences intense temperature gradients and dynamic melt pool variations during the first stage of laser activation, which frequently results in the formation of an enormous and unstable molten zone. Heat accumulation causes a stable thermal gradient as the scan goes on, resulting in more constant melt-pool dimensions. The exit transient region is formed when variability is eventually introduced toward the end of the track by geometric tapering or thermal loss. This structure is well aligned with what has been given in the experimental studies [31].
Let $x_s(k)$ denote the laser x-position at discrete time index k with corresponding time t_k. Let T_{melt} be the melting temperature and z_{top} the top-surface elevation. To avoid transient effects occurring at the start and end of the laser track, the steady-state regime was defined as the central portion of the scan where the melt pool geometry remains nearly constant. The total scan length L is obtained from the range of laser positions and the midpoint is calculated as:

$$x_{\text{mid}} = \tfrac{1}{2}\Big(\min_k x_s(k) + \max_k x_s(k)\Big) \tag{2.40}$$

A symmetric window around this midpoint according to a fractional parameter $\eta \in (0, 1)$ of the total scan track length:

$$S(\eta) = \Big\{\, k : \ \big|x_s(k) - x_{\text{mid}}\big| \le \tfrac{\eta}{2}\, L \Big\}, \quad L = \max_k x_s(k) - \min_k x_s(k), \tag{2.41}$$

with window fraction is taken to be $\eta = \frac{1}{3}$. The steady-state index (k_{ss}) is the median index of this window,

$$k_{\text{ss}} = \text{median}\big(S(\eta)\big),$$

which is a robust way to determine the melt pool width and allows small oscillations or numerical noise to be averaged out which provides a stable and representative estimate of steady-state

melt pool dimensions. In the present implementation, this selection simplifies to identifying the timestep k_{ss} whose laser position is closest to the track midpoint x_{mid}.
At the indentified index k_{ss} corresponding to laser position $x_s(k_{ss})$ and time t_{ss}, the temperature field is reconstructed using linear interpolant on surface mesh. A sampled line in the y direction is used to locate the intersections of the melt isotherm $T = T_{\text{melt}}$. If multiple disjoint molten segments are detected, the widest contiguous span defines the steady state melt-pool width:

$$W_{\text{ss}} \;=\; \max_{r}\big(y_R(r) - y_L(r)\big).$$

where $y_L(r)$ and $y_R(r)$ are the left and right isotherm crossings of segment r. This measurement captures the stable molten footprint under the quasi-steady thermal conditions and ensures that the reported width corresponds to the widest continuous molten zone observed at steady state, providing a robust measure of the stable melt pool geometry. The variation of width with respect to time is given in the following Figure 2.14a.

The steady-state melt-pool depth is evaluated using the 3D temperature field. At $k = k_{\text{ss}}$ with laser position at $x_s(k_{\text{ss}})$, a 2D temperature slice in the y-z plane is interpolated on a focussed grid on the laser track. The depth is defined as the vertical distance from the top surface to the lowest point in the molten region:

$$D(x,t) \;=\; z_{\text{top}} - \min\Big\{\, z :\; \exists\, y \text{ s.t. } T(x,y,z,t) \geq T_{\text{melt}} \Big\}.$$

The variation of depth with respect to time is given in the Figure 2.14b:

Both steady-state quantities, W_{ss} and D_{ss} are obtained from the same transient temperature field. Evaluating width and depth at the central, near-equilibrium portion of the track yields representative geometry not effected by initial and final transients. The liquidus threshold T_{melt} provides a clear, physics-based boundary for the molten region. Time histories $W(t)$ and $D(t)$ (Figure 2.14) and spatial profiles $W(x)$, $D(x)$ are used as diagnostics to verify that variations in the steady window are small compared to the transient regions. Furthermore, to check for the steady state status for the other sources, the widths and depths plots as a function of time and scan position are plotted and are provided in the Appendix A.4.

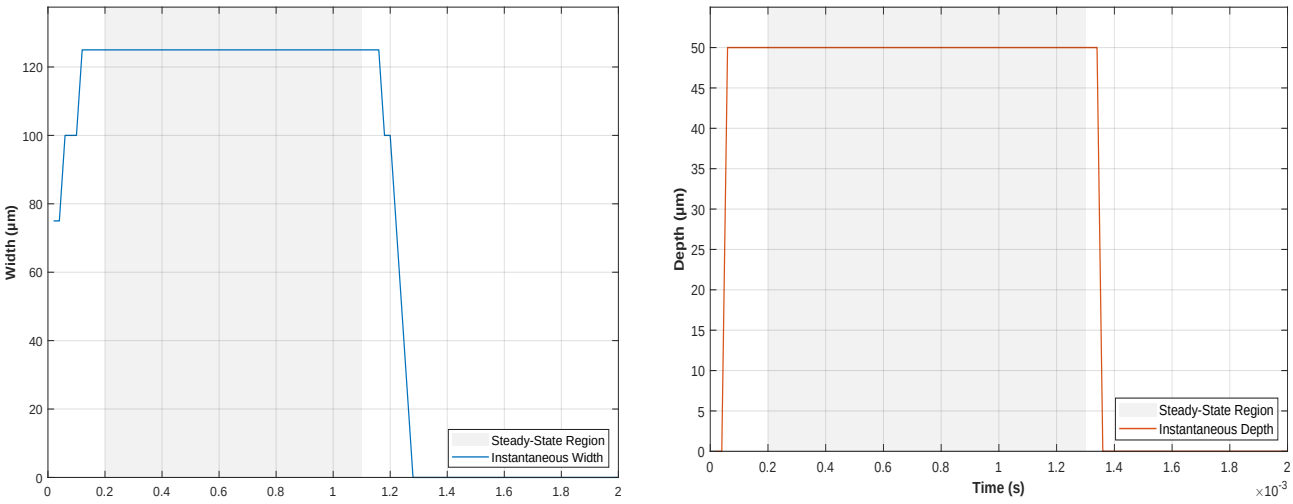

(a) Melt pool width as a function of time.

(b) Melt pool depth as a function of time.

Figure 2.14: Temporal evolution of melt pool dimensions for $P = 200$ W and $V = 1$ m/s: (a) width and (b) depth as functions of time.

2.7 Concluding Remarks

This section presents the complete methodological framework developed to predict temperature evolution and melt-pool geometry during the Laser Powder Bed Fusion (L-PBF) process using a semi-analytical approach. Analytical temperature field solutions were formulated for two representative laser source configurations: a two-dimensional circular Gaussian beam and a uniform-intensity square (top-hat) beam. The Gaussian formulation was analytically obtained in closed form, but the top-hat case necessitated symbolic manipulation in Mathematica to yield a manageable analytical expression. The analytical temperature field, denoted as $\tilde{T}$ provides a physically interpretable solution describing transient heat conduction in a semi-infinite medium and forms the foundation of the temperature prediction framework. To verify the spatial energy distribution of the heat sources, the laser intensity profiles were first examined under stationary conditions and evaluated at successive time instants. These plots reveal the distinct thermal footprints associated with each source shape. In particular, the top-hat formulation exhibits a spatially uniform intensity at the moment of laser activation, consistent with its definition, whereas the Gaussian source displays a radially decaying profile. With increasing time, heat conduction into the substrate leads to a progressive reduction in the peak surface temperature at the same spatial location, confirming the expected transient thermal diffusion behavior. Spatial derivatives of the closed-form temperature solutions were subsequently computed using Mathematica and incorporated into the semi-analytical framework to facilitate coupling with the finite-difference scheme. This integration enables simulation of different laser source shapes under consistent boundary and material conditions, will be discussed in the following chapter. The semi-analytical method provides a computationally inexpensive predictor of temperature transients $T(x, y, z, t)$ that preserves key physics while remaining sufficiently computationally efficient for parametric exploration.

Melt-pool geometry is extracted using a consistent thermal criterion: the molten region is defined by $T \geq T_{\text{melt}}$. The method is widely accepted in the experimental and numerical L-PBF studies because it provides a physics-based link between the thermal field and the observable molten shape. The melt pool width and depth has been quantified through linear and scatter interpolation schemes that identify the melt pool with sub cell accuracy providing spatial precision finer than the original computational grid and acting as a means to reduce the discretization error and ensures physically consistent melt-pool profiles. In summary, the steady-state melt-pool width and depth are extracted at the center of the laser scan path, within the region where transient effects are minimized and the geometry stabilizes. This integrated approach provides a computationally robust and physically interpretable foundation for subsequent simulations, parametric studies and process map generation.

3 Simulation Setup and Results

In this section, the temperature distributions obtained for the three laser source shapes: point, 2D circular Gaussian, and top-hat square are presented. The simulations were conducted primarily to implement these different heat source models within the semi-analytical framework and to verify the accuracy of the thermal predictions. The objective is to demonstrate that the semi-analytical thermal model performs reliably for each source type and that the boundary conditions are correctly imposed.

3.1 Simulation Setup

The dimensions of the part illustrated in Figure 3.1a are 2 mm x 2 mm x 2 mm. The part is built by adding layers in the positive z-direction and the bottom surface, ∂V_{bot}, is attached to the base plate. The temperature of the base plate is assumed to be constant and equal to T_c, while the top surface, ∂V_{top}, and the lateral surfaces,∂V_{lat}, are insulated. The thermal parameters of the material representative of Ti-6Al-4V are given in Table 3.1 and are assumed to be temperature independent.

Table 3.1: Ti-6Al-4V properties used in simulations

Quantity	Value (unit)
Density, ρ	$4420\,\mathrm{kg/m^3}$
Specific heat, c_p	$990\,\mathrm{J\,kg^{-1}\,K^{-1}}$
Thermal conductivity, k	$42\,\mathrm{W\,m^{-1}\,K^{-1}}$
Absorptivity, A	0.818
Melting Temperature, T_{melt}	1928 K

3.2 Part geometry and discretization

The laser scanning vector scans the top surface of the domain, Figure 3.1 (a). The process parameters are listed in the following Table 3.2 for the three cases, namely C1 - point, C2 - 2D Gaussian circular and C3 - Top-hat Square. A single track simulation was performed on a thermally insulated cuboid body with dimensions of $l_a = l_b = l_c = 2$ mm with the origin of the body V at bottom left corner, where the scan track is depicted in the Figure 3.1 (b). The point A with coordinates in mm that is located at (1.9, 1.8, 2). A single scan vector having a length of 1.8 mm is discretized into a number of point sources, 2D circular Gaussian and square sources. To obtain the temperature distribution of the domain, the semi-analytical model proposed in [6] is implemented in MATLAB. The part in Figure 3.1 (a) is discretized using an equidistant grid of size 0.05 mm, that is $\Delta x = \Delta y = \Delta z = 0.05$ mm. To calculate the numerical time step

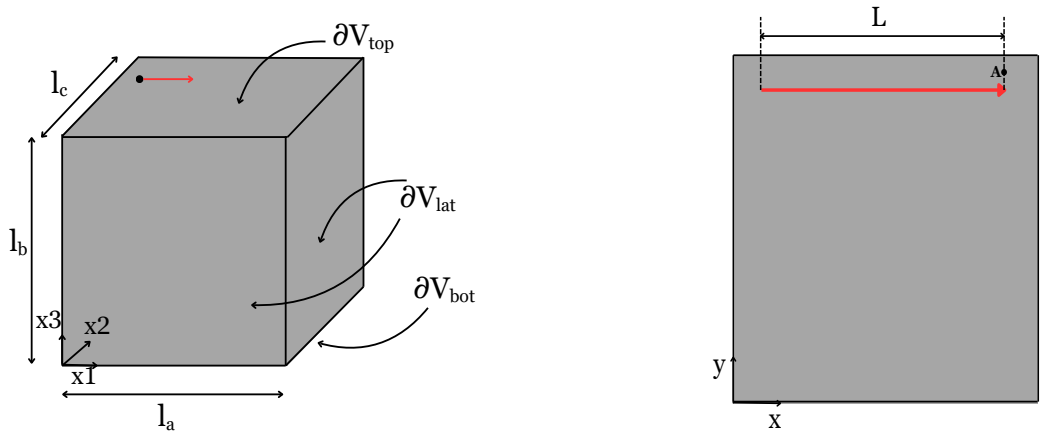

(a) (b)

Figure 3.1: (a) Schematic of the body V and its dimensions. The body is attached to the base plate at ∂V_{bot} and the boundaries ∂V_{top} and ∂V_{lat} are insulated. (b) Schematic of the top surface of the body V, where a moving laser heats the body. The scanning laser track, with a length of L = 1.9 mm, is shown in red. The coordinates of point A are (1.9,1.8,2) mm, where a moving laser heats.

for the explicit finite difference scheme to be stable and convergent, the following expression will be used.

$$\left(\frac{\alpha}{\Delta x^2}+\frac{\alpha}{\Delta y^2}+\frac{\alpha}{\Delta z^2}\right)\Delta t \leq \frac{1}{2} \tag{3.1}$$

For an equidistant grid size of 0.05 mm, the time step should be smaller than 4.34×10^{-5}. Nevertheless, it was shown in [6], that temporal convergence was attained for a time step size of 5×10^{-5} s independent of the chosen diffusivity value, α. But according to the calculated time step from the stability condition it should be less than the 4.34×10^{-5}. Therefore, the time step size of 2×10^{-5} s will be used in the finite difference scheme for more accurate results and for more finer temporal discretization of the body.

3.3 Process Parameters

The process parameters used in the single-track simulations for all three source shapes are summarized in Table 3.2. A spot size of 75 μm was selected for both the Gaussian and top-hat sources to keep the spot area approximately equal, thereby enabling a more direct comparison. This choice ensures that any observed differences in melt pool geometry, defect formation, or process window can be attributed to the beam intensity profile itself rather than variations in the total delivered energy [33]. The spot size also plays a critical role in influencing melt pool dimensions, process stability, and the transition thresholds between conduction and keyhole mode. By maintaining an equal spot area across source types, the energy density and resulting process behavior can be directly compared, which forms the basis for constructing the process maps in Chapter 4.

For top-hat sources, spot sizes typically range from 100μm to 200μm in studies of conduction- and keyhole-mode melting in L-PBF. Reported power levels in the literature include 140 W, 200 W, 250 W, and 300 W, while higher powers are in the range of 600–900 W are often em-

ployed for larger beams due to their reduced energy density [3, 11, 15]. The present choice of power and spot size is therefore consistent with values commonly used in the literature, while also ensuring a meaningful and controlled comparison between different beam profiles.

For the Gaussian and top-hat cases, the spot area was matched for fairness of comparison. Both the laser power and the spot size were increased, in line with common practice in the literature, to achieve realistic melt pool formation. Finally, since the computational domain is significantly larger than the laser spot, the mesh resolution was refined to ensure that the localized temperature gradients near the beam were captured accurately.

Table 3.2: Process Parameters used in Single-track simulation cases.

Case	Shape	Spot Size (μm)	P (W)	v (mm/s)	Base plate T_c (K)
C1	Point	35	35	0.3	453
C2	Circular Gaussian	75	150	0.3	453
C3	Top-Hat Square	75×75	150	0.3	453

3.4 Simulation Results

The results of the single track simulations for different sources are given in this section. The simulation has been performed in MATLAB, where the different source shapes are implemented in the semi-analytical method. The primary reason behind performing the study on single-track is due to their efficiency and their ability to provide fundamental insights into complex manufacturing phenomena of the L-PBF process, where full layer scanning is performed. The primary motivation for focusing on single-track studies is their computational and experimental efficiency: single-track simulations and experiments require substantially less time, material, and computational resources compared to full-layer or multi-track analyses. This allows for rapid, systematic exploration of key process parameters and melt pool behavior, providing essential insights into L-PBF fundamentals.

3.4.1 Single-Track Simulations for Different Source Shapes

Figure 3.2 presents snapshots of the temperature distribution at the top surface of the domain for the three source cases, namely the point source, the 2D circular Gaussian source, and the uniform-intensity square source. The results correspond to a single laser track, as illustrated in Figure 3.1b, and are shown at three different time instants: 0.0006 s, 0.0032 s, and 0.0060 s. The first row shows the point source case at the respective time instants (Figures 3.2a, 3.2b, and 3.2c). The second row corresponds to the 2D circular Gaussian source (Figures 3.2d, 3.2e, and 3.2f), while the third row depicts the uniform-intensity square source (Figures 3.2g, 3.2h, and 3.2i). The total scan time for the single track is 0.006 s. The baseplate temperature is prescribed as 453 K. Regions where the temperature exceeds the liquidus temperature of 1928 K indicate melting, as the material in these zones has reached or surpassed the melting threshold.

Earlier, it was shown that stationary sources exhibit a broadened and smoothed temperature distribution as time progresses. This behavior is observed for both the 2D circular Gaussian

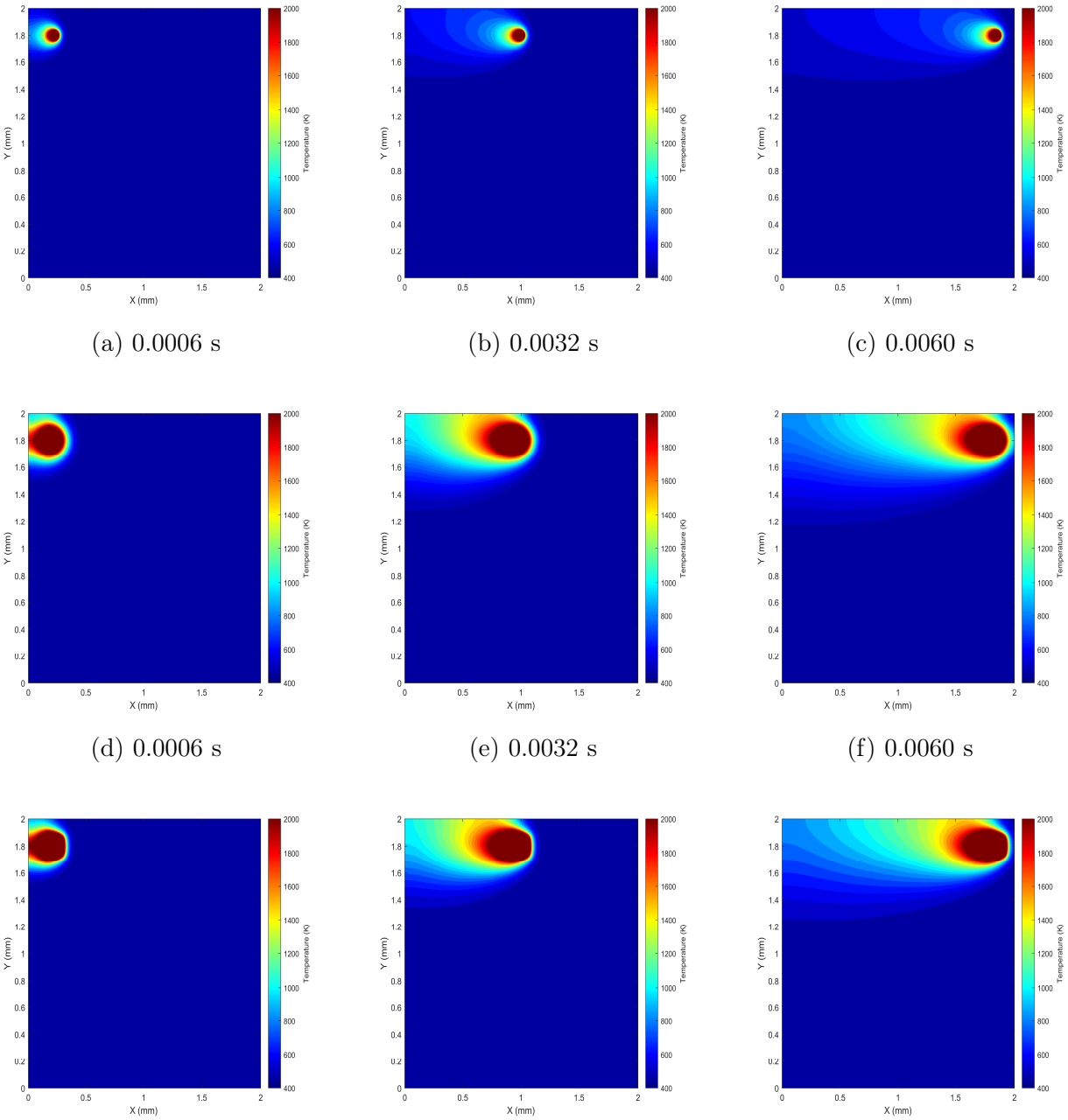

(a) 0.0006 s (b) 0.0032 s (c) 0.0060 s

(d) 0.0006 s (e) 0.0032 s (f) 0.0060 s

(g) 0.0006 s (h) 0.0032 s (i) 0.0060 s

Figure 3.2: Snapshots of the temperature distribution at the top surface of the domain at three instants in time (0.0006 s, 0.0032 s, and 0.0060 s). The rows correspond to (a–c) point source, (d–f) 2D circular Gaussian source, and (g–i) square source. All results are obtained using the semi-analytical model proposed in [6].

source and the uniform-intensity square source. While the circular Gaussian case initially follows a distinct Gaussian profile, the temperature field becomes increasingly spread out once the source starts moving due to the effects of laser motion and heat conduction. A similar broadening effect is visible in the uniform-intensity square source scenario. For a clearer comparison, zoomed-in temperature distributions are provided in Figure 3.3, with individual cases shown for the point source in Figures 3.3a, the 2D circular Gaussian case in 3.3b, and the uniform-intensity square source in 3.3c. The distinct square profile is clearly visible, while the smoother appearance arises from the combined influences of laser scanning and thermal conduction within the material.

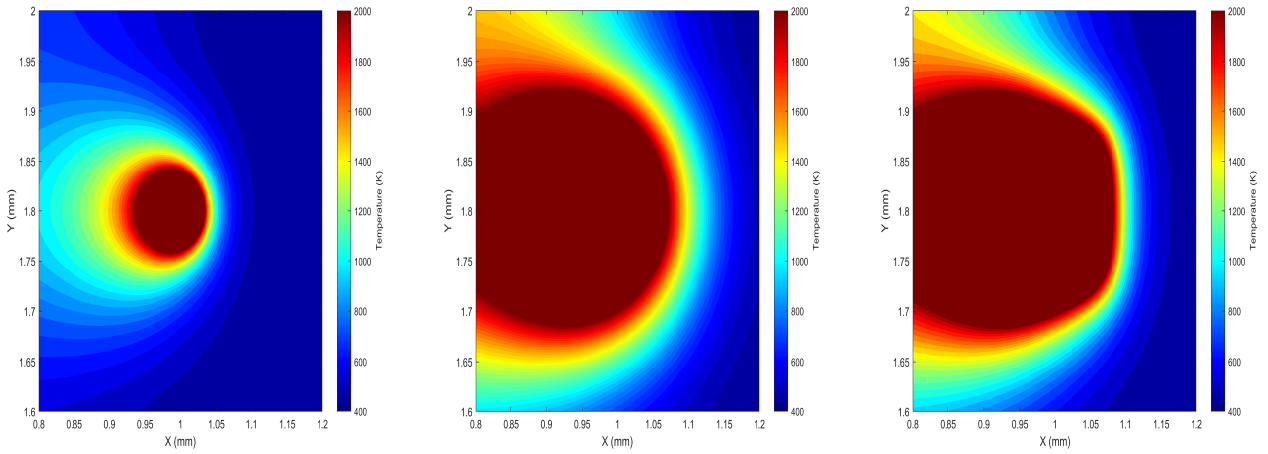

(a) Point source (b) 2D circular Gaussian source (c) Uniform-intensity square source

Figure 3.3: Close-up of the temperature distribution around the laser beam for (a) the point source, (b) the 2D circular Gaussian source, and (c) the uniform-intensity square source, predicted by the semi-analytical model proposed in [6]. Zoom window: 400 μm.

3.4.2 Verification of Boundary Conditions

The proper enforcement of the boundary conditions is crucial in the establishing the credibility of the implementation of the different sources. The adiabatic conditions are met when the heat flux to be across the lateral boundaries are zero which can require the temperature isolines to be perpendicular to the boundary of interest. For the proper enforcement of the boundary conditions finite difference scheme is utilised which has been explained in the above chapter 2. In Figure 3.4, we can clearly see the decomposed temperature field for all the three sources, where the analytical field for the point case is presented 3.4a, where figure 3.4b is the boundary correction field and finally the total temperature field which is the summation of analytical field $\tilde{T}$ and numerical correction field $\hat{T}$. All plots are shown on a consistent temperature scale (0–2000 K) to facilitate direct comparison. In the total temperature field, we are able to observe the contour lines are nearly orthogonal to the right boundary. For more clear view, the isolines corresponding to specific temperatures are also plotted for all the three cases and are given in the Appendix B.

Figure 3.5 presents the finite-difference grids used for all three source cases, illustrating the

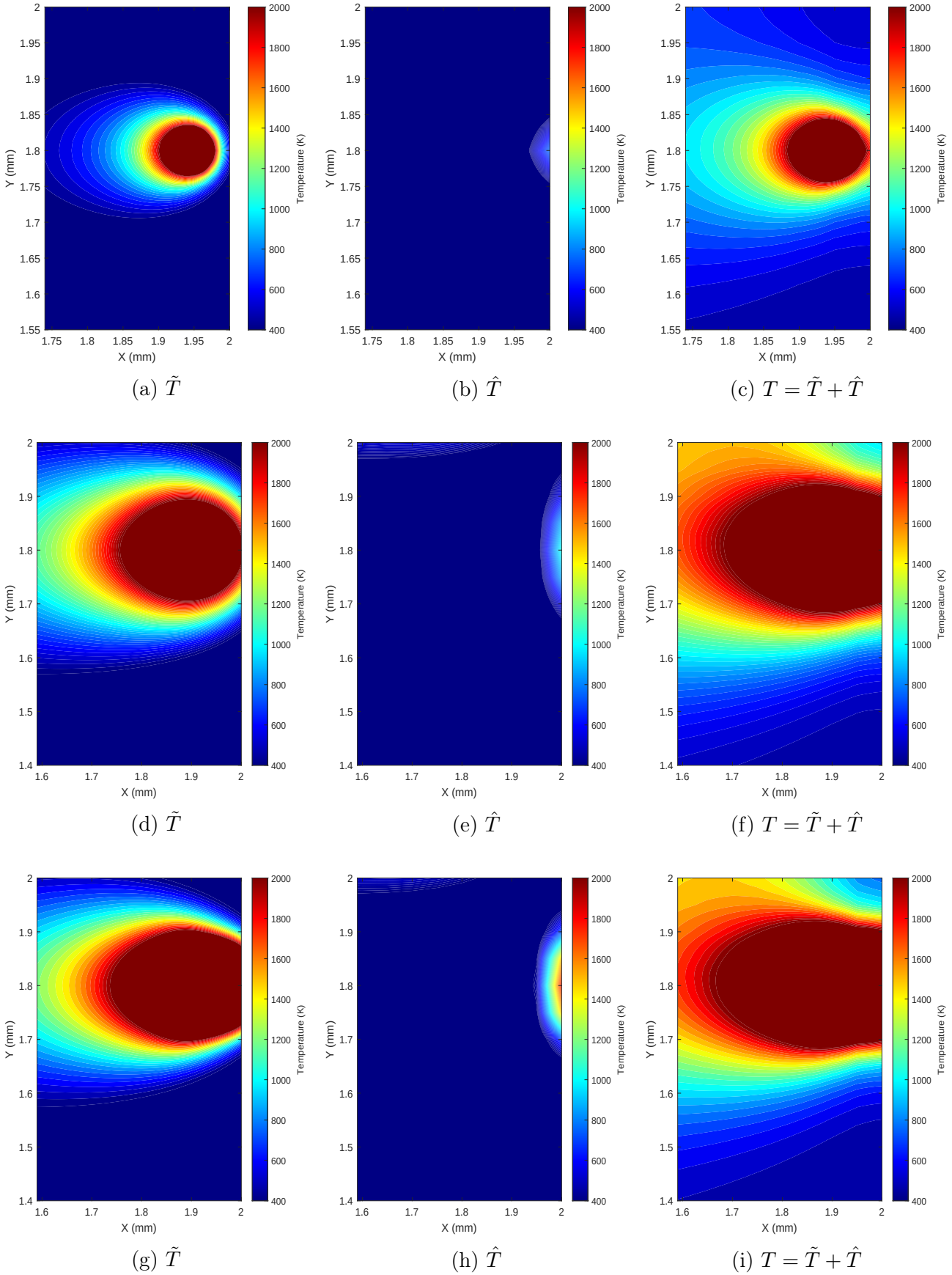

(a) $\tilde{T}$ (b) $\hat{T}$ (c) $T = \tilde{T} + \hat{T}$

(d) $\tilde{T}$ (e) $\hat{T}$ (f) $T = \tilde{T} + \hat{T}$

(g) $\tilde{T}$ (h) $\hat{T}$ (i) $T = \tilde{T} + \hat{T}$

Figure 3.4: Comparison of analytical ($\tilde{T}$), correction ($\hat{T}$), and total ($T = \tilde{T} + \hat{T}$) temperature fields near the adiabatic boundary for (top) point, (middle) circular Gaussian, and (bottom) square sources. Each row is zoomed to 500–800 μm to show contour behavior near the boundary.

spatial discretization and the distribution of grid points across the computational domain. The lack of orthogonality of contour lines at the right boundary is attributed to the limitations imposed by the relatively coarse mesh size 50μm. However, if the mesh is increased more then there would be better orthogonality. With insufficient grid resolution, the thermal gradients near the domain boundary are not adequately resolved, leading to numerical artifacts including non-orthogonal isotherms. This effect is well-known in finite difference and finite volume simulations, and can be mitigated by refining the mesh which improves both gradient representation and enforcement of boundary conditions.

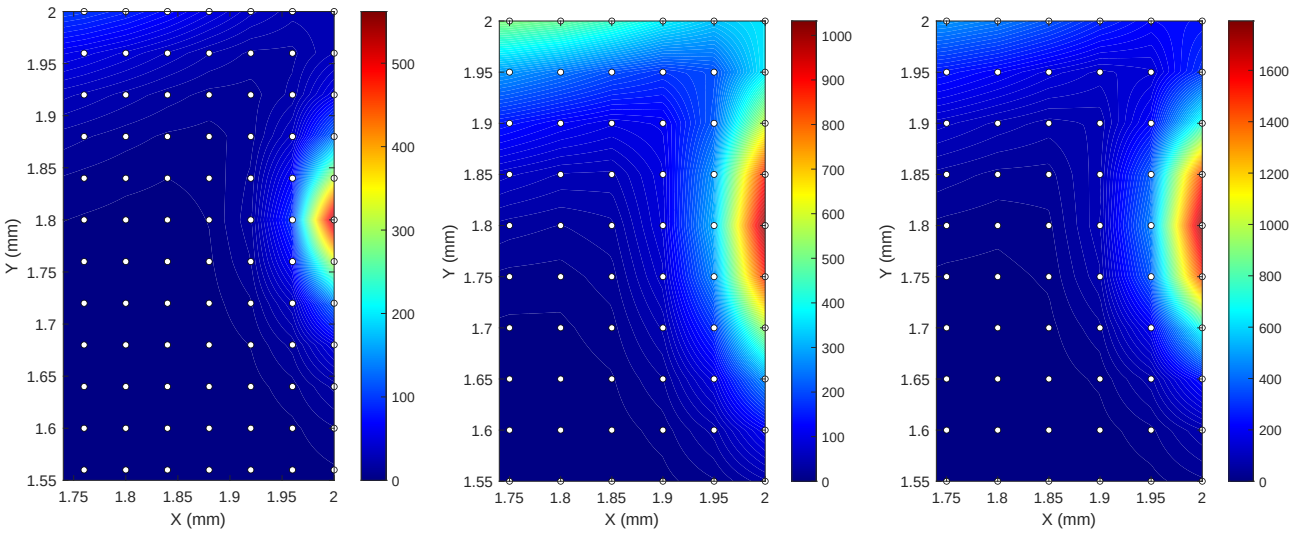

(a) Point source (b) 2D circular Gaussian source (c) Square source

Figure 3.5: Finite-difference correction field ($\hat{T}$) with grid visualization for the three source types: (a) point, (b) 2D circular Gaussian, and (c) uniform-intensity square.

3.4.3 Thermal history

In Laser Powder Bed Fusion (L-PBF), the thermal history represents the temporal evolution of temperature at a given location as the laser scans, melts, and subsequently cools the material. Figure 3.6 illustrates the temperature histories for the three considered source cases: point source, uniform-intensity square source, and 2D circular Gaussian source. All simulations were performed under identical process parameters to enable direct comparison.

It can be observed that the point source exhibits the highest peak temperature, reaching approximately 5000 K. In contrast, the uniform-intensity square and 2D circular Gaussian sources yield lower peak temperatures, which are comparable to each other. This difference arises because the latter two sources distribute the same total laser power over a finite area, resulting in a lower energy density at any given point within the melt pool. Consequently, the spatial spreading of power reduces the localized heating intensity, leading to lower maximum temperatures in their thermal histories.

Additionally, the Gaussian source shows a gradual intensity decay from the center toward the edges, further diminishing the peak temperature relative to the point source. The top-hat square source, while maintaining uniform intensity, similarly reduces the maximum temperature by distributing energy evenly across a larger footprint rather than concentrating it at a single point. Although the total input power remains constant across all cases, the spatial distribution

of energy in the Gaussian and square sources broadens the thermal profile and limits the peak temperature, explaining their comparatively lower thermal histories.

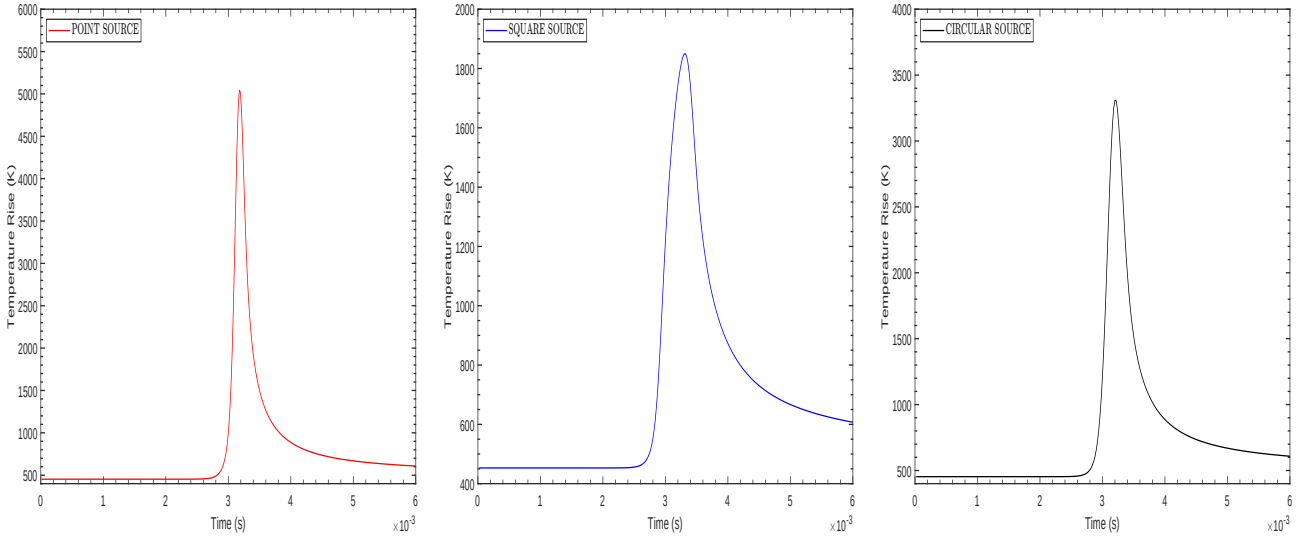

(a) (b) (c)

Figure 3.6: Comparison of the thermal history at point $(1, 1.8, 2)$ mm obtained with the point source, square source and circular source in the semi-analytical model (with a grid size of 0.05 mm), highlighted in red, blue and black respectively. $P = 35$ Watts, Velocity $= 0.3$m/s, spot size $= 35\ \mu m$.

3.5 Concluding remarks

This chapter established and validated the semi-analytical thermal framework for three representative laser-source models: point, 2D circular Gaussian, and top-hat square within a finite domain. The field decomposition into an analytical component and a finite-difference correction was shown to enforce the insulated and base-plate boundary conditions. However, slight deviations from contour orthogonality near the adiabatic surfaces indicate that the boundary conditions are not fully satisfied. These discrepancies primarily stem from discretization limitations. The grid spacing (50μm) is larger than the laser spot size ($35\,\mu$m), leading to under resolved source representation and gradient errors at boundaries. For the source cases where the spot size is comparitively on the larger side (i.e., 75μm), the situation improves partially. However, the grid still remains too coarse to fully resolve the local thermal gradients, as fewer than five nodes span the beam diameter. Minor deviations from ideal orthogonality and slight artificial flux leakage can therefore still occur, reflecting discretization rather than physical inaccuracies.

Single-track simulations demonstrated physically reasonable transients and melt footprints across sources, with peak temperatures behaving as expected (highest peaks for the point source, more distributed fields for area sources). On this basis, the framework provides reliable temperature fields from which steady-state melt-pool dimensions can be extracted using a consistent melt criterion ($T \geq T_{\text{melt}}$) and robust interpolation. These results enable systematic power–velocity sweeps and direct comparison across source shapes. The present setup adopts constant thermophysical properties, neglects vaporization-driven effects and detailed powder

interactions, and omits mirror sources in favor of a refined grid and small time step. These assumptions are acceptable for the scope of single-track scanning, but they delineate the model's applicability. The next chapter builds on this foundation to (i) quantify steady-state widths and depths across the process space, (ii) construct process maps for each source shape, and (iii) identify lack-of-fusion and keyholing boundaries that define the optimal, defect-minimizing operating window.

4 Process Maps

In the context of L-PBF, process maps are also known as "printability maps." They are specifically designed to measure the impact of defects, especially porosity, in L-PBF. These maps are essential for identifying different types of defects, such as lack of fusion, keyholing, and balling, as well as optimal areas. The maps are typically created using a mix of experimental data, physics-based modeling, and data analysis.

The overall steps for generating process maps are shown in Figure 4.1. Based on the experimental studies [7, 8], we defined our ranges for process parameters, including Power (P) and Velocity (V). We constructed the process maps for two layer thicknesses: 100 μm and 30 μm. This approach helps us understand how layer height affects defect occurrence. After identifying the parameter ranges, we used a semi-analytical method to calculate transient temperature fields. From these simulations, we obtained the steady-state melt pool width and depth using the isotherm-based method described in chapter 2. We then used these geometric measurements to categorize each processing condition based on physical defect criteria.

Here's a detailed breakdown of how we construct processing maps:

Defining Input Variables: This typically includes

1. Processing Parameters: The maps are usually plotted in a Power-Velocity (P-V) space, where laser power (P) and scan velocity (V) serve as the primary axes. Other important parameters include hatch spacing (H), layer thickness (T), and laser spot size. We systematically vary these parameters to cover a wide processing range.

2. Material Properties: Key thermophysical properties of the material, such as melting temperature, density, specific heat, thermal conductivity, thermal diffusivity, and laser absorptivity, are vital inputs since they influence the interaction between the laser and the metal, as well as the melt pool shape.

Melt Pool Modeling and Prediction: This part involves

1. Thermal Models: We use physics-based thermal models and a semi-analytical method that employs superposition to forecast the thermal history and melt pool dimensions (width and depth) based on processing parameters and material properties.

Application of Defect Criteria: We consider two defect criteria, namely Lack of Fusion and Keyholing, which are determined by the melt pool's geometry.

1. Lack of Fusion (LOF): The LOF phenomenon occurs when there is incomplete fusion due to insufficient energy penetration from the laser into the material. For a single-scan track, it is defined by the condition $D < T$, where D is the depth of the melt pool and T is the layer thickness [25, 34].

2. Keyhole: Keyhole porosity results from excessive energy input and intense vaporization. The key geometric indicator for this situation is the melt pool aspect ratio, defined as the depth-to-width ratio D/W>0.5. Beyond this threshold, the melt pool shifts from a stable, shallow conduction mode to a deep, narrow cavity, which is a sign of keyhole formation. This shift is tied to the onset of recoil pressure-driven vapor depression and melt instability and has been confirmed in several studies [8, 35].

Mapping and Visualization: This process includes

1. Process Map Generation: We evaluate the steady-state melt pool dimensions predicted by the models using the criteria described above. We classify each power-velocity pair as defect-free or associated with a specific defect mode. This process is repeated across the P-V space to create printability maps.

Refinement: We assess the predictive ability of these maps by comparing them with experimental data from existing literature. Any differences may point to areas where we need to refine our analytical models or defect criteria.

Overall, process maps offer engineers and designers a straightforward decision-making tool. They provide clear visual cues about the chances of meeting quality standards and help guide the selection of processing parameters needed to create desired components.

4.1 Steady-State Melt Pool Profiles and Dimensions

In this study the steady state depths and widths, for a single track simulation has been considered. This is the point where in the melt pool track the least variation in the dimensions of melt pool depths and widths is observed. For the construction of the process maps the laser scan starting and ending points are set away from boundaries to avoid edge effects which can distort melt pool geometry, particularly at low or high velocities. Typically it is considered to be set away at approximately 1-2x laser spot radius. For single track cases, the melt pool features (width/depth) are small compared to the domain, in these case, the melt pool dimensions are expected to have the order of 100 μm. Accordingly, a computationally domain of is 2 x 2 x 2 mm is adopted. A mesh size of 50 μm is employed to balance computational cost and spatial resolution. However, this resolution provides only 2 grid points across a characteristic 100μm melt pool dimension, which may be insufficient for highly accurate thermal boundary and feature representation. Hence, while this setup is sufficient for trend analysis and process-map generation, further refinement (e.g., 10 μm spacing) would be necessary for high-fidelity validation or boundary-sensitive simulations. The total scan length is kept at least 1 mm, ensuring that the melt-pool reaches a steady thermal state within the track. The energy input is quantified using the volumetric energy density, given by:

$$\text{Energy Density } \left[\frac{\text{J}}{\text{mm}^3}\right] = \frac{P}{V \times h \times t} \tag{4.1}$$

Where P is the power, V is scan speed, t is layer thickness and h is Hatch distance.

4.1.1 Influence of laser power

Increasing laser power enhances the input energy and peak temperature in the molten zone, thereby expanding both the width and depth of the melt pool. The following Figure 4.2, illustrates these general trends for all three heat-source formulations: point, uniform-intensity square (top-hat), and 2D circular Gaussian. For all these cases, the melt pool widths and depths are plotted as a function of power while all the other parameters are held constant. The results demonstrate a clear upward trend in melt-pool dimensions with increasing power consistent across all source types. According to Equation 4.1, the energy density is directly proportional to P, and the analytical temperature expressions (Equations 2.23 and 2.29) show a

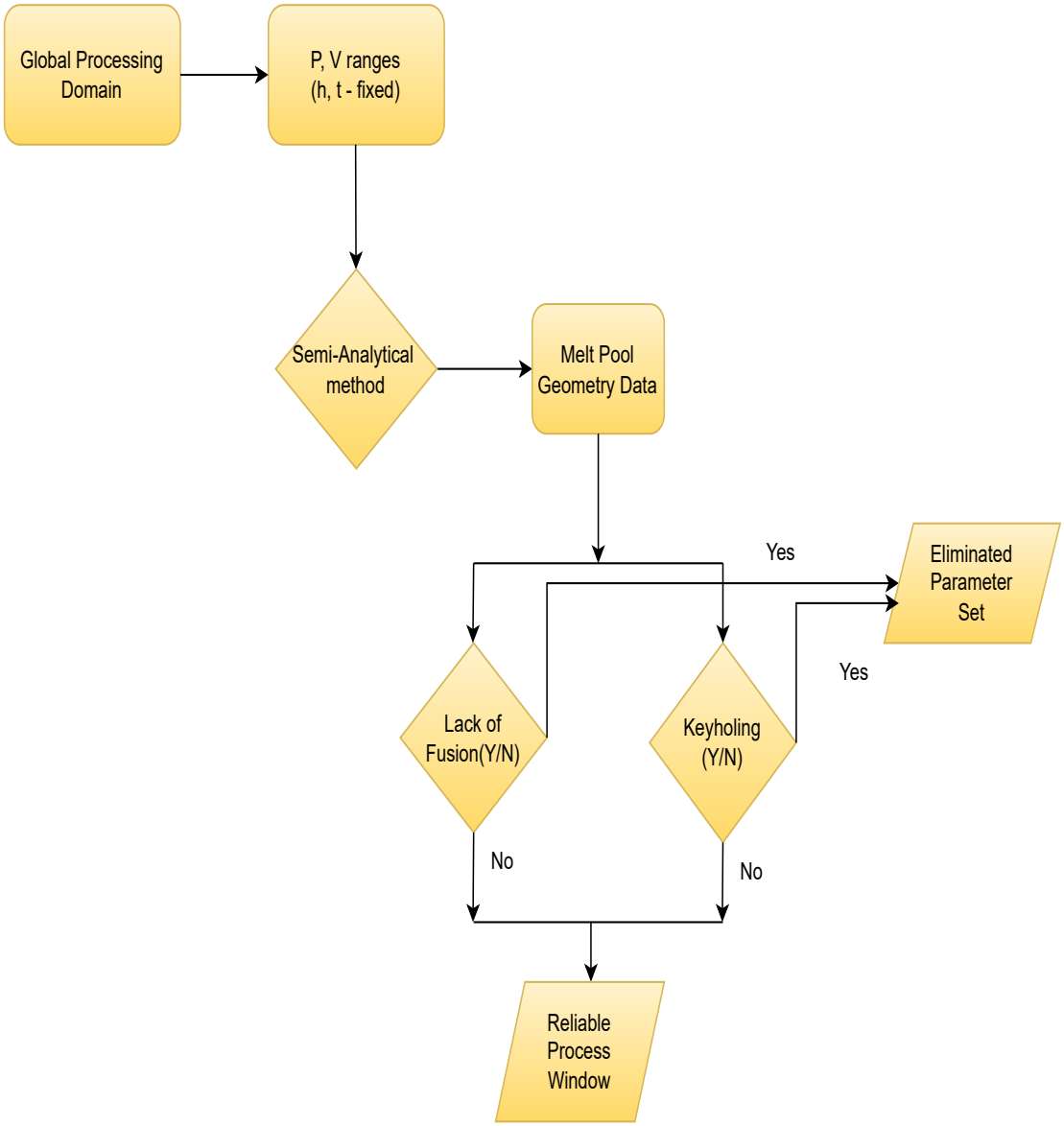

Figure 4.1: Schematic workflow for constructing process windows, showing the dependence on hatch spacing (h) and layer thickness (t).

direct proportionality between temperature rise and laser power. Consequently, both the peak temperature and molten zone extent increase with P, reinforcing that power primarily governs the overall heat input and melt-pool expansion.

4.1.2 Influence of laser velocity

In L-PBF, higher scan speed decreases the effective heat input per unit length leading to reduced melting and smaller melt-pool dimensions. This inverse trend is observed consistent with Equation 4.1. For all the three sources, point, 2D circular Gaussian and uniform intensity square source, the melt pool width and depth decrease as the velocity increases indicating a clear transition from a deeply penetrated melt pool at low speeds to a shallow, conduction-dominated pool at high speeds. The obtained results exhibit strong qualitative agreement with experimental findings from [7] and semi-analytical predictions by [36]. Minor deviations arise primarily from differences in thermal parameters and source size assumptions, which influence the energy distribution within the melt pool.

To consolidate the influence of power and velocity into a single representative metric the linear energy density (LED), defined as the ratio of laser power to scan velocity (P/V) is introduced. This parameter effectively represents the energy input per unit scan length, offering a compact measure of overall heat input. The objective is to evaluate whether the three sources: Point, Square and 2D Gaussian collapse into a unified trend when expressed in terms of LED.

For each laser source type, the steady-state melt-pool widths were plotted against the linear energy density (LED), with data points color-coded according to their predicted defect regime: lack-of-fusion, optimal, or keyholing. It is based on the geometric criteria discussed later in Section 4.3. The color segmentation highlights how variations in P/V translate into distinct process outcomes. A first-order linear regression is fitted to reveal dominant trend.

Across all beam profiles, the melt-pool width shows an approximately linear dependence on the linear energy density (LED), as illustrated in Figure 4.10. This behavior aligns with the expectation that higher energy input per unit scan length results in wider molten tracks. However, the color-segmented regimes reveal that beyond certain thresholds, the width increase no longer signifies stable conduction; instead, transitions into lack-of-fusion or keyhole modes occur, depending on the beam profile. This observation highlights that while LED serves as a convenient global indicator of heat input, it cannot by itself capture defect transitions or represent the influence of spatial energy distribution within the melt pool.

Therefore, to gain a more complete understanding of how laser source shape influences melt-pool geometry and defect formation, the subsequent section compares melt-pool profiles obtained for different intensity distributions under identical process parameters. This comparison forms the basis for constructing the power-velocity process maps presented later in Section 4.3.

4.2 Comparison of Melt Pool Geometries Across Source Shapes

The steady state melt pool geometries for all the three laser sources, point, 2D circular Gaussian and uniform-intensity square (top-hat) are compared in this section to elucidate the difference

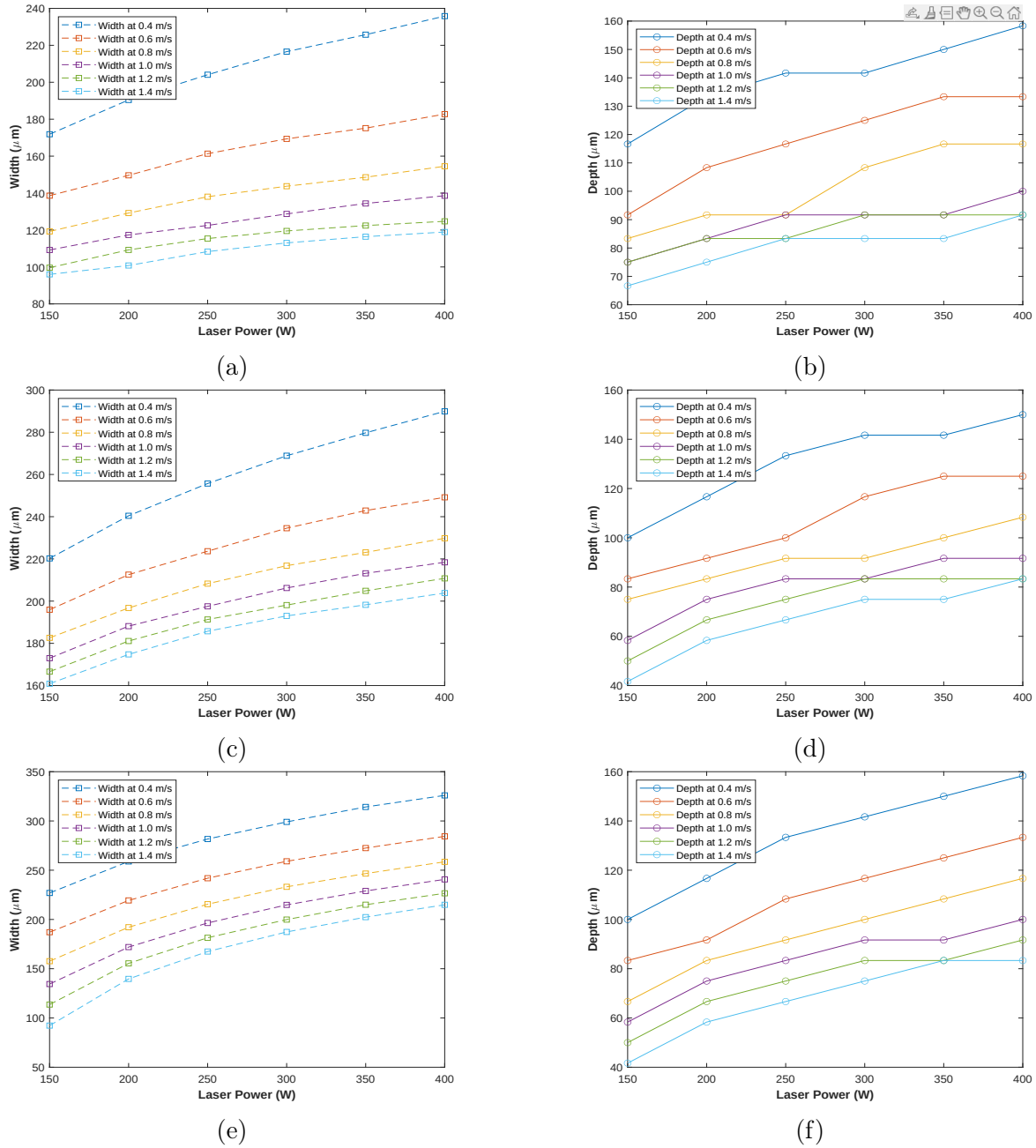

Figure 4.2: Variation of steady-state melt pool widths and depths with laser power for three heat source types: point source, uniform square source, and 2D circular Gaussian source. Power range: 150-400 W (interval: 50 W), velocity range: 0.4-1.4 m/s (interval: 0.2 m/s), layer thickness = 100 μm.

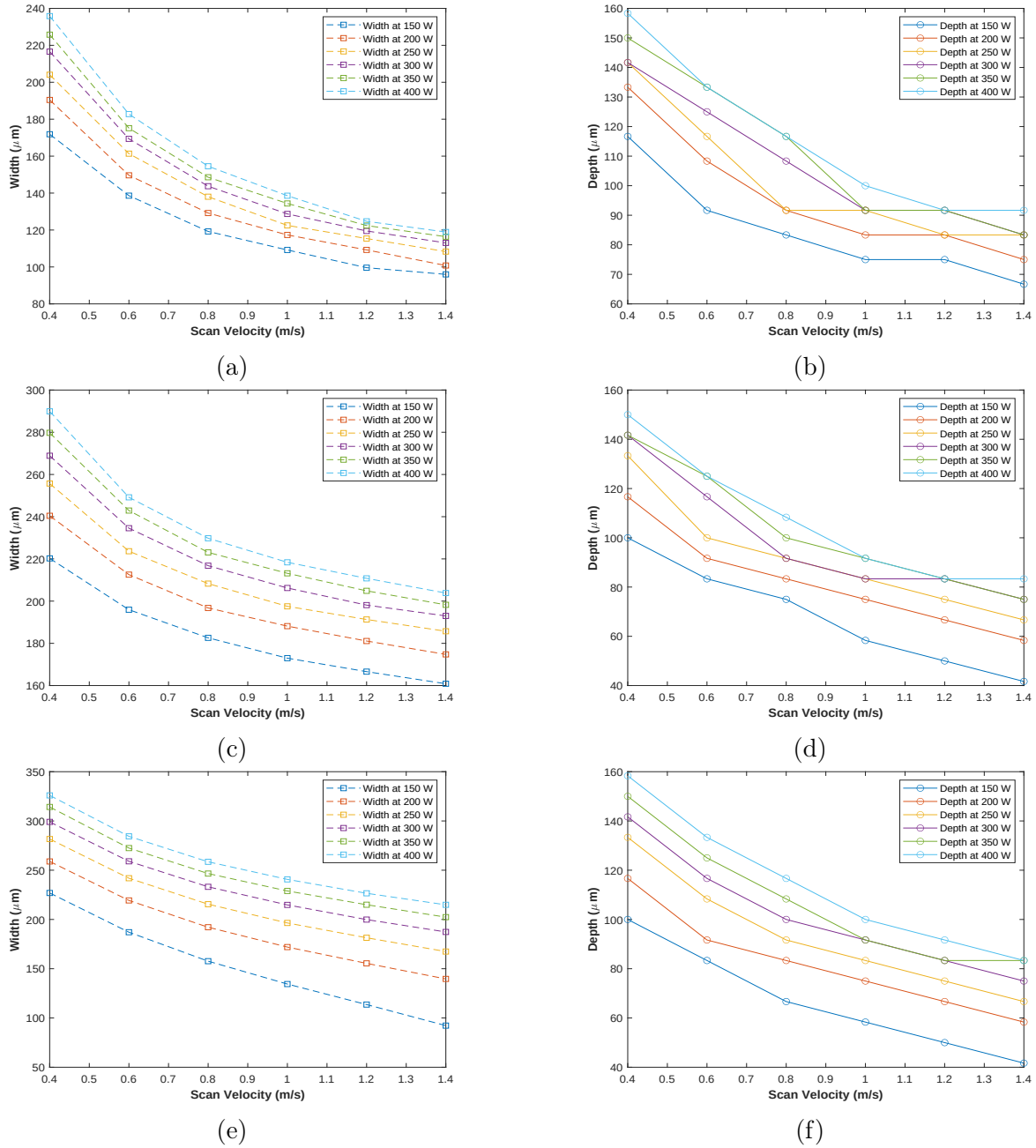

Figure 4.3: Variation of Steady state depths and widths with respect to Velocity and calculated for the point source, uniform intensity square source and 2D circular Gaussian source. Power range: 150-400 Watts with an interval of 50 W and velocity range : 0.4 - 1.4 m/s with an interval of 0.2 m/s and layer thickness = 100 μm.

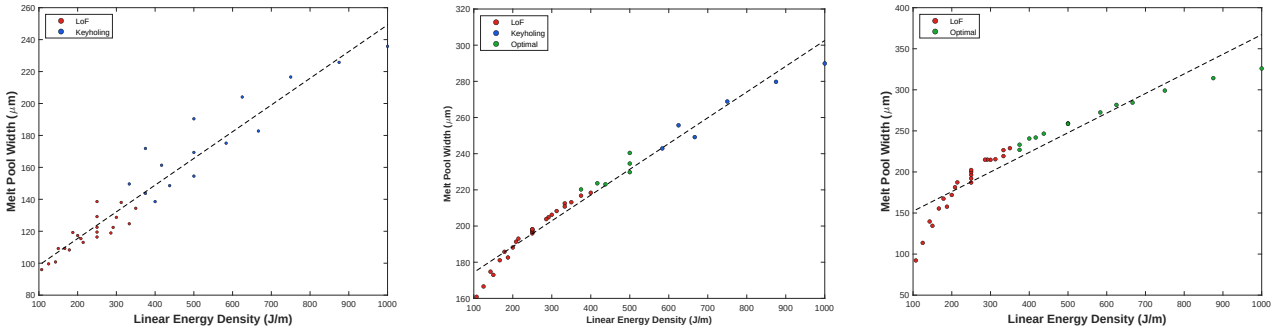

(a) Point source (b) Square source (c) Gaussian source

Figure 4.4: Comparison of linear energy density plots for three source cases: (a) point source, (b) uniform square source, and (c) 2D circular Gaussian source. Red points indicate lack-of-fusion regions, green points show optimal regions, and blue points represent keyholing regimes.

between the profiles. The melt pool widths and depths have been calculated and visualized using the methodology discussed in chapter 2. However, the widths have been calculated with sub-cell precision via top-surface refinement whereas depths have been calculated from the 3D computational grid to maintain the computational efficiency. The Figure 4.5(a-c), showcase the single track simulation of the point source along with the different profiles of the melt pool. The Figure 4.5(a) shows the snapshot of the temperature distribution of the whole domain at 0.0032 seconds. This is the temperature distribution of the point source predicted by the semi-analytical method in [6]. The top-view (XY-plane) and cross-sectional (YZ-plane) profiles are shown in Figures 4.5(b) and (c), respectively. The melt-pool width and depth are indicated in the Figure 4.5, with the peak temperature reaching 36000 K for the effective spot radius of 35μm along with the layer thickness as 30μm. Because the point source represents an idealized, highly localized energy input, it produces a deep and narrow melt pool characterized by steep temperature gradients around the beam center.

Furthermore, the Figure 4.6(a-c) showcase the single track simulation of the 2D circular Gaussian source along with the melt pool profiles under identical processing conditions. The full domain temperature distribution at t=0.0032 seconds is shown in the Figure 4.6 (a) with corresponding XY and YZ sections in Figure 4.6 (b) and (c) respectively. Compared to the point-source case, the 2D circular Gaussian beam produces a wider but shallower melt pool. The width of the melt pool is more as compared to the point source because the circular source spans an area and the depth is less as compared to the point source. The steady-state results for the uniform-intensity square source are shown in Figures 4.7(a-c). Figure 4.7(a) presents the overall temperature distribution at $t = 0.0032$s, while the top-view and cross-sectional melt-pool profiles are displayed in Figures 4.7(b) and (c). Unlike the Gaussian beam, the square top-hat profile maintains a constant intensity across the beam footprint with sharp spatial cut-offs at the edges. This uniformity produces the widest melt pools among the three cases, with relatively flat bottom profiles indicative of homogeneous energy deposition.

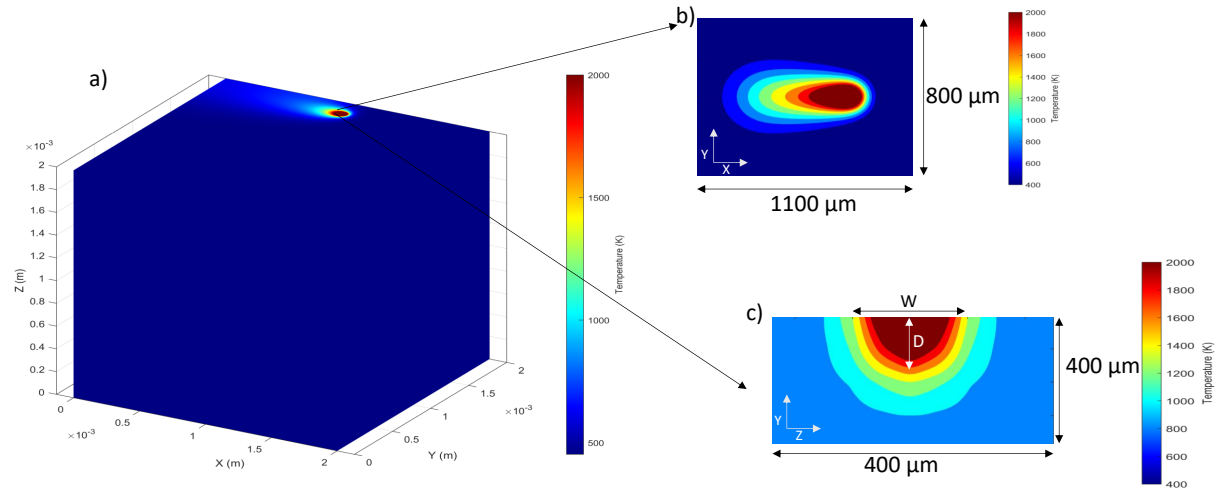

POWER-VELOCITY	WIDTH (W)	DEPTH(D)	PEAK TEMPERATURE	SPOT SIZE
300 W – 1 m/s	128.7 µm	91.7 µm	36908 K	35 µm

Figure 4.5: a) Snapshot of the temperature distribution of the bounded domain at t = 0.0032 s for point source, b) XY cross section of the melt pool and c) YZ cross section of the melt pool.

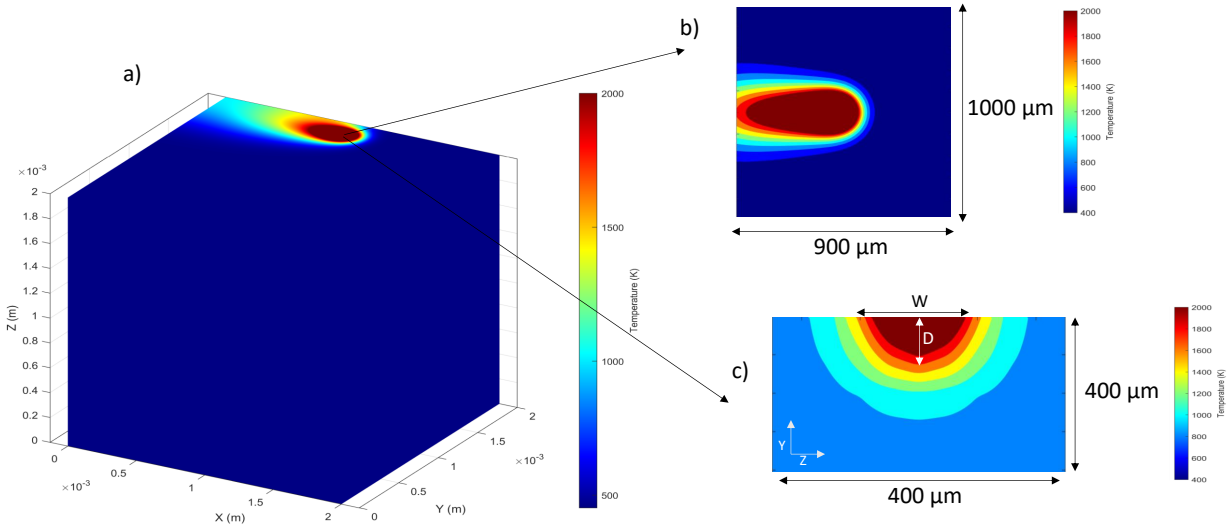

POWER-VELOCITY	WIDTH	DEPTH	PEAK TEMPERATURE	SPOT SIZE
300 W – 1 m/s	187.5 µm	83.3 µm	6007 K	75 µm

Figure 4.6: a) Snapshot of the temperature distribution of the bounded domain at t = 0.0032 s for 2D circular Gaussian, b) XY cross section of the melt pool and c) YZ cross section of the melt pool.

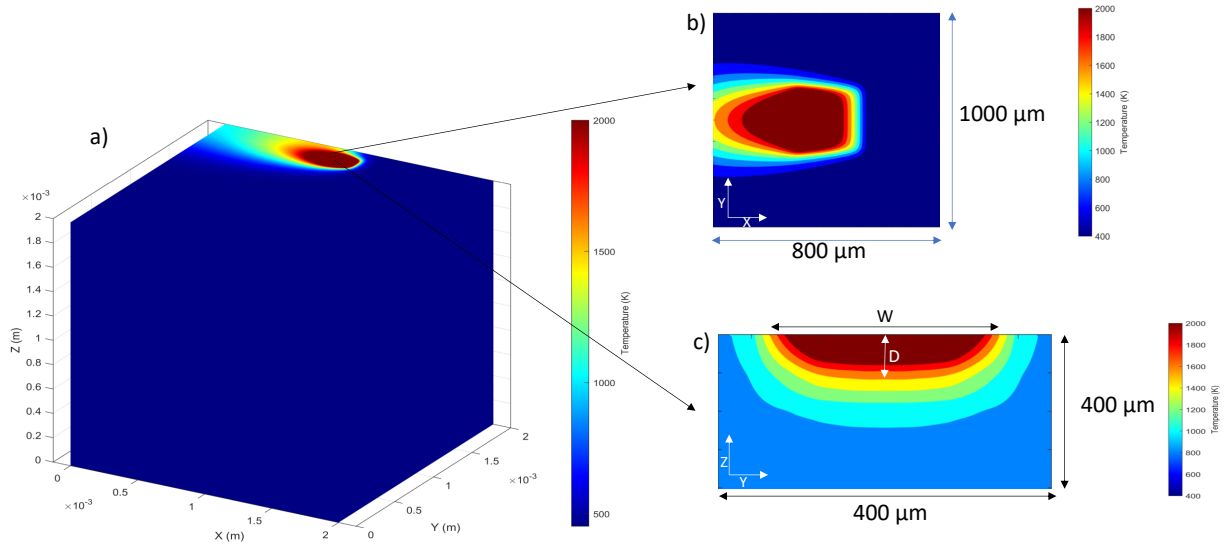

POWER-VELOCITY	WIDTH	DEPTH	PEAK TEMPERATURE	SPOT SIZE
300 W – 1 m/s	272.8 µm	58.3 µm	3488 K	75 x 75 µm

Figure 4.7: a) Snapshot of the temperature distribution of the bounded domain at t = 0.0032 s for uniform intensity square source, b) XY cross section of the melt pool and c) YZ cross section of the melt pool.

4.3 PV Map Construction and Defect Classification

Power velocity maps were constructed for the all the three sources, point, 2D circular Gaussian and uniform-intensity square (top-hat) utilising the above discussed approach. In these cases, the keyholing region has been defined by the aspect ratio (D/W) being greater than 0.5 and LOF occurs when the melt pool depth is insufficent to penetrate the layer thickness $D < t$. The P-V ranges for Ti-6Al-4V were selected with guidance from [8]; material properties are those in Table 3.1. To maintain consistency in defect definitions, hatch spacing h and layer thickness t were held fixed within each study. In the Table 4.1, the parameters opted for the study are presented. The material properties are same as given in Table 3.1. Figure 4.8 presents the resulting process maps: the left column shows color-segmented maps (red = LOF, blue = keyhole, green = conduction/optimal), while the right column shows scaled-marker overlays where marker dimensions are proportional to the steady-state width and depth at each (P, V) pair. In the marker plots, regions with depth > width visually reinforce the keyhole regime, whereas width > depth is typical for top-hat distributions operating in conduction or LOF regions.

4.3.1 Lack-of-Fusion Regions

LOF is predicted where the melt pool fails to penetrate the deposited layer $D < t$. As expected, high velocity / low power combinations fall in the LOF regime. In the Figure, 4.8a shows LOF (red) concentrated at low energy density; the corresponding width/depth markers in Figure 4.8b

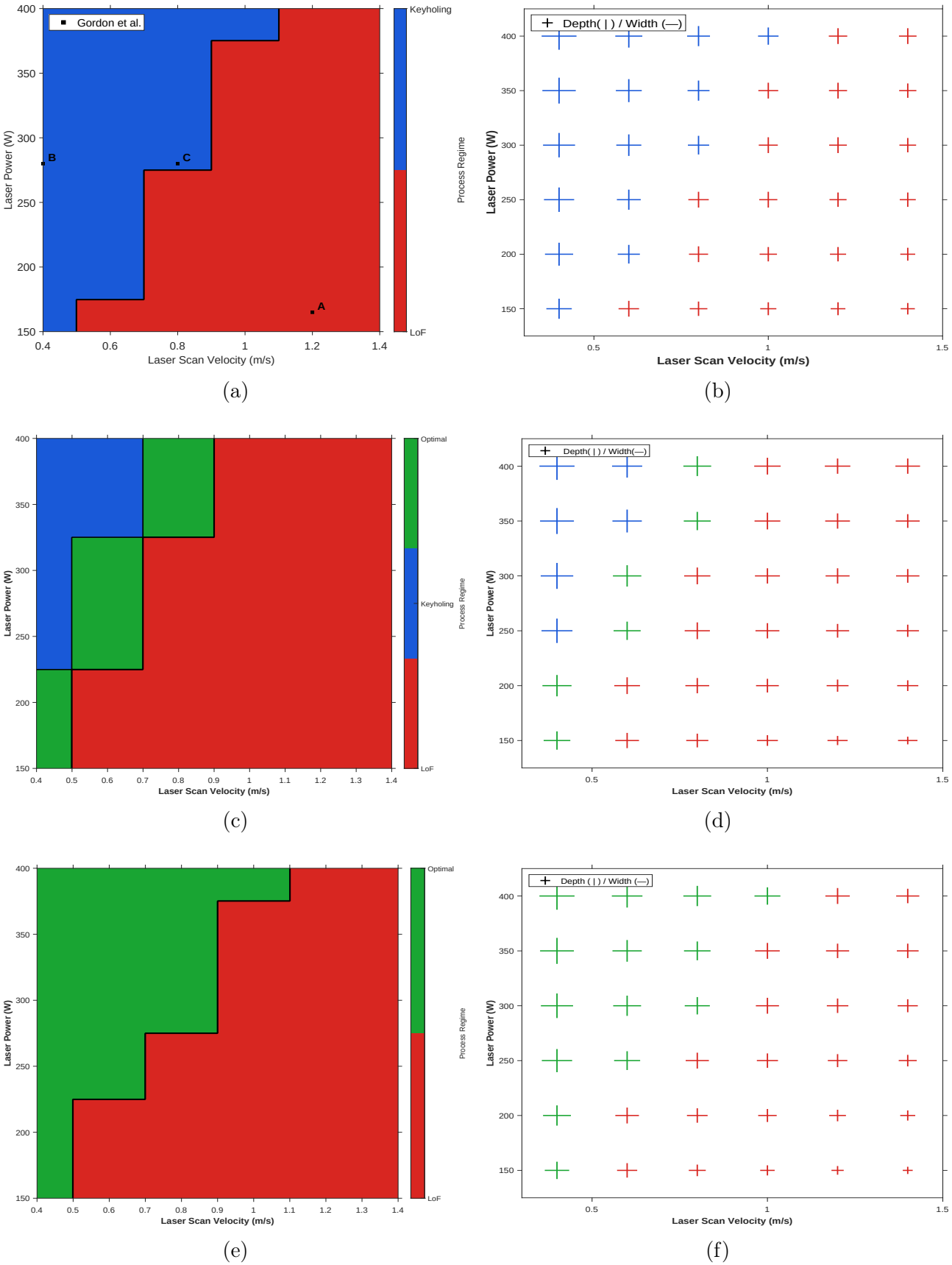

Figure 4.8: Power-velocity process maps for Ti-6Al-4V using (a,b) point source, (c,d) square source (e,f) 2D circular Gaussian. Red = lack-of-fusion region, blue = keyholing region, green = optimal region. (b),(d) and (f) show depth and widths associated with the sources, layer thickness = 100 μm

Table 4.1: Parameters for process maps study

Power (W)	**Velocity (m/s)**	**Hatch spacing** (μm)	**Layer thickness** (μm)	**Spot size** (μm)	**Source shape**
150–400	0.2–1.4	80	100	35	Point
150–400	0.2–1.4	80	100	37.5 × 37.5	Top-hat square
150–400	0.2–1.4	80	100	75	2D Circular Gaussian
100–195	0.5–1.2	80	30	35	Point
300–600	0.2–1.4	80	30	75 ×75	Top-Hat Square
150–400	0.1–1.3	80	30	75	2D circular Gaussian

show small vertical extents (shallow pools). The points A, B and C whose values are given in the Table 4.2 are marked on the plot which depicts the parameters the same region as obtained in the experimental study [8].

Subsequently, the process maps are plotted for the uniform-intensity square source, here we can observe the optimal regions marked in green regions. There is a prominent lack-of-fusion region because the melt-pool energy distribution are majorly wider in the case of top-hat profiles, which can be seen from the Figure 4.8c and has been observed in the experimental studies [11, 15, 22]. For smaller spot size of $37.5 \times 37.5\,\mu$m and high layer thickness $t = 100\mu$m, reflects the broader, shallower pools. This is consistent with the width-dominated markers in Figure 4.8d.

Point	**Power (W)**	**Velocity (m/s)**	**Defect Status**
A	165	1.2	Lack-of-fusion
B	280	0.4	Keyholing
C	280	0.8	Keyholing

Table 4.2: Experimentally observed defect regimes from [8] mapped onto the generated process window through semi-analytical method in Figure 4.8a(a).

We note that some discrepancies with multi-layer experimental datasets are expected: experiments typically include layer-to-layer thermal accumulation and hatch-overlap effects, whereas the present maps are based on single-track steady-state metrics with fixed h and t. Furthermore, to further align with the actual experimental conditions, the power velocity range and the layer thickness are set according to what has been given in the [7], and the following process map was obtained Figure 4.9a. Agreement is good for the location and trend of regime boundaries; where mismatches occur, they can be attributed to differences in absorptivity and the inability to capture the actual physics phenomena.

4.3.2 Keyholing Boundaries

Keyholing arises at high energy input where recoil pressure and vaporization induce a deep, narrow cavity. We classify this regime by $D/W > 0.5$. In the point and top-hat maps (Figures 4.8a

Point	Power (W)	Velocity (m/s)	Defect Status	Predicted by Process Map
A	100	0.5	Optimal	Yes
B	150	0.75	Optimal	Yes
C	150	1	Optimal	Yes
D	150	0.5	Keyholing	No
E	195	1	Optimal	No
F	195	1.2	Optimal	Yes
G	195	0.5	Keyholing	Yes

Table 4.3: Comparison of experimentally observed defect regions reported by [7] with the semi-analytical model predictions, mapped onto the corresponding process map.

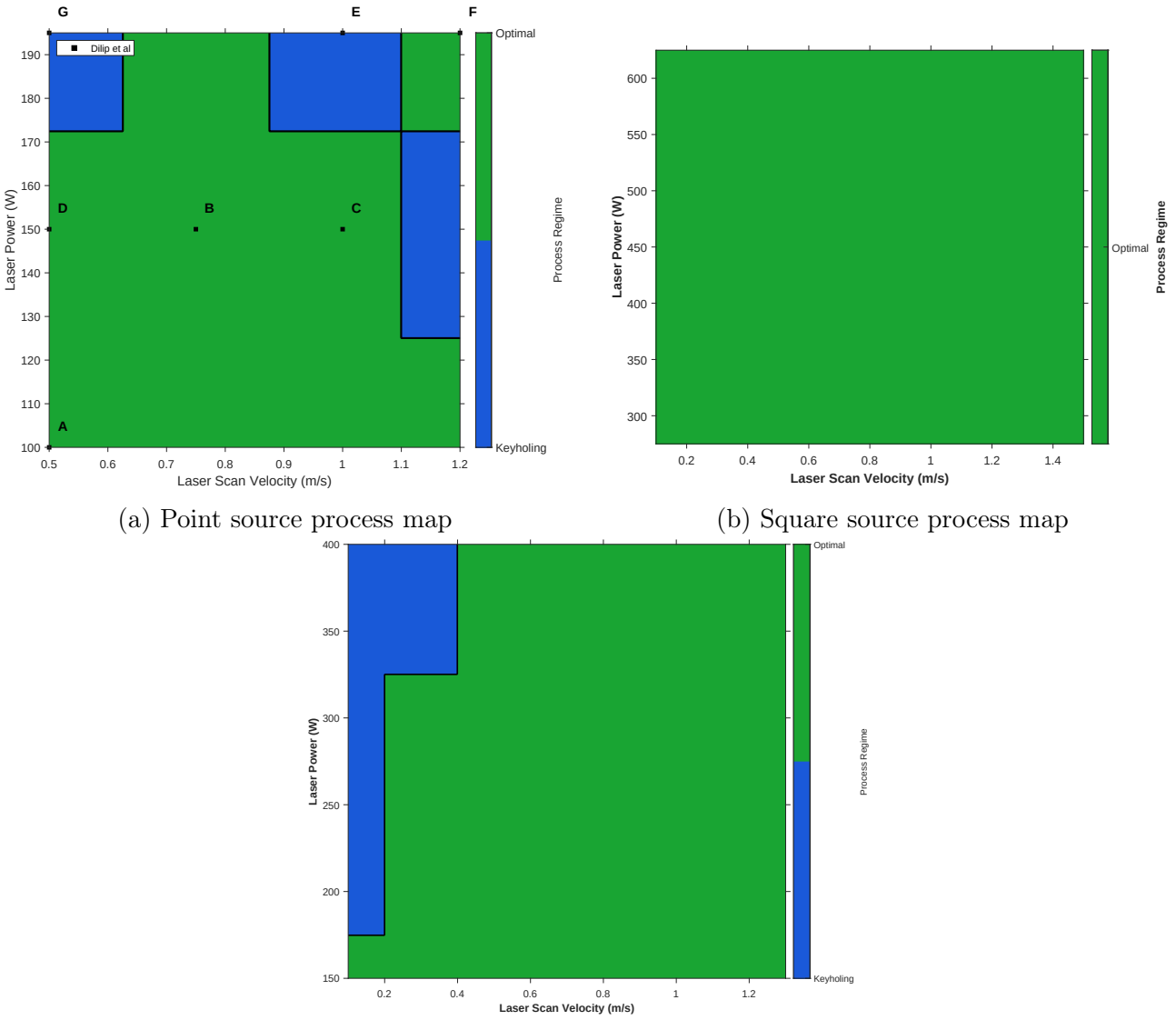

(a) Point source process map

(b) Square source process map

(c) Circular Gaussian source process map

Figure 4.9: Comparison of process maps for point, square laser sources and circular Gaussian at a layer thickness of 30 μm.

and 4.8c), blue regions cluster at high P and low V. The marker plots (Figures 4.8b and 4.8d) visually confirm $D > W$ within these zones. For certain datasets, increasing the threshold to $D/W > 0.7$ improved alignment with [7], highlighting the sensitivity of keyhole classification to the chosen aspect-ratio cut-off. For the Gaussian case, no keyhole region appears within the baseline (P, V) ranges of Table 4.1; keyholing emerges only when the parameter space is extended to higher energy densities (Appendix C). Finally, Figure 4.10 compares the aspect-ratio trend vs. scan velocity for the point source with [7]; the decreasing D/W with increasing V agrees well with experimental trends.

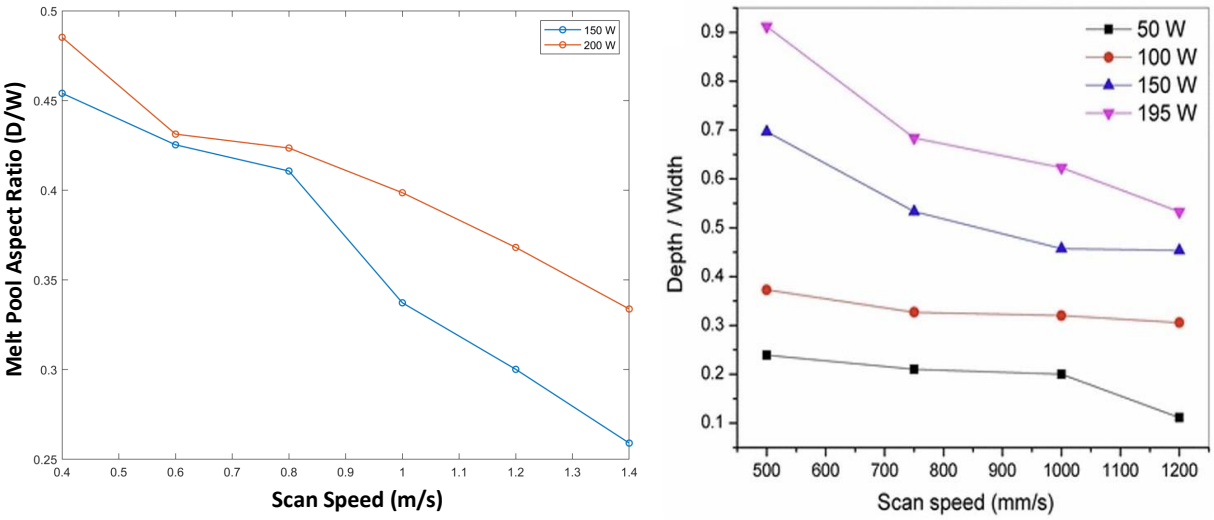

Figure 4.10: Comparison of aspect ratios for the point source case obtained using the semi-analytical method and experimental data from [7].

4.4 Discussion

The process maps constructed in this chapter illustrate the influence of laser power (P) and scan velocity (V) on melt pool geometry and defect formation in Ti-6Al-4V. The workflow (Figure 4.1) employs a semi-analytical thermal model to compute temperature fields, from which the steady-state melt pool width (W) and depth (D) are extracted.These metrics underpin two geometry-based criteria: lack-of-fusion (LOF) when $D < T$ (where T is the layer thickness) and keyholing when the aspect ratio exceeds a threshold, $D/W > 0.5$. This framing provides a physically interpretable and computationally efficient route to classify regimes over large (P, V) grids. For the point source, Figures 4.8a and 4.9a present the predicted process maps alongside representative defect data from [7, 8]. The locations of experimentally observed defect points from [8] correspond well with the expected regions in the model-derived maps (Table 4.2). For instance, the reported LOF defect at $(P, V) = (165\ \text{W}, 1.2\ \text{m/s})$ appears in the predicted low-energy region, while the experimentally observed keyholing cases align with the

high-energy (blue) regions of the map. Melt-pool width and depth increase with laser power and decrease with scan velocity, as both dimensions are governed by the energy density, which scales directly with P and inversely with V. Higher power increases total energy input and peak temperature, enlarging the molten region and deepening penetration [37]. Conversely, higher scan velocity shortens the laser-material interaction time, reducing energy absorption and limiting melt-pool growth. Minor quantitative deviations between the model and experimental data are attributed to differences in layer thickness and hatch spacing, variations in the geometric criterion for keyholing, and the scope of the thermal model. To assess the sensitivity of the classification criterion, the aspect ratio threshold was adjusted to 0.7 to match the conditions reported by [7]. The resulting process map (Figure 4.9a) showed the closest agreement with experimental trends, confirming that discrepancies between prediction and experiment can be reconciled through parameter calibration within the semi-analytical framework. Also in the Figure 4.8a, the optimal region is completely missing which is attributed to high layer thickness ($100\,\mu$m) causing the inaccurate penetration of energy and this can be also because of insufficient pre-heating temperature. For smaller layer thicknesses, such as 30 μm, the model predictions show good agreement with experimental observations for dense Ti-6Al-4V samples. Under manufacturer-recommended processing conditions, the lowest porosity levels were observed experimentally, matching the predicted optimal processing window. For example, the experimentally identified dense-optimum condition at $P = 100$ W and $V = 0.5$ m/s corresponds closely with the model predictions [38, 39].

Influence of 2D circular Gaussian Source on Defects:

The intensity distribution of the 2D circular Gaussian source is characterized by a peak at the beam center that gradually tapers toward the edges. This spatial distribution strongly influences the thermal behavior, melt pool morphology, and defect formation mechanisms during the L-PBF process. The general trends in melt pool width and depth with respect to laser power and scan velocity observed in this study are consistent with the literature [2, 7, 36]. Increasing scan velocity leads to reduced penetration and narrower tracks, while the Gaussian energy distribution typically results in deeper penetration due to the concentration of intensity at the beam center. The melt pool morphology transitions from a semi-circular, conduction-mode profile at low power densities (Figure 4.6c) to a deeper, narrower keyhole-mode profile at higher power densities. Figure 4.8e shows that at higher layer thicknesses, the Gaussian source exhibits a broader optimal processing window which can make it suitable for high build-rate capability. The strong penetration capability of the Gaussian beam reduces the likelihood of lack-of-fusion (LOF) defects making it suitable for higher build rates typically associated with increased layer thicknesses [40]. However, at very high scan velocities, LOF can still occur, as observed in the process map. Beyond this operating range, keyholing becomes increasingly dominant, corresponding to conditions where the aspect ratio D/W exceeds 0.5. The lower threshold of 0.5 simply marks the point where the melting mode becomes geometrically classified as keyhole, susceptible to increased depths, rather than the final point where pores inevitably form. The process map illustrating this extended regime is provided in Appendix C.1 (Figure C.1a). At lower layer thicknesses, a broader and denser optimal processing window is observed. However, the onset of keyholing begins around $(P, V) = (175\,\text{W}, 0.2\,\text{m/s})$ and becomes more pronounced at higher energy inputs, particularly at $P = 400\,W$ with scan velocities between 0.1 and 0.4 m/s.

Influence of Uniform intensity Square source on Defects:

The uniform-intensity square source, often referred to as a top-hat or flat-top beam, is characterized by an even distribution of energy across the entire spot area. For the same laser power and spot radius, the top-hat profile exhibits a lower peak intensity than the Gaussian distribu-

tion. The resulting melt pool morphology produced by the square source typically features a flatter bottom boundary (Figure 4.7c). The melt pool widths are strongly influenced by this uniform energy distribution and are generally larger compared to those formed under a Gaussian beam [3, 22]. The uniform-intensity (top-hat) profile produces lower peak temperatures within the melt pool, resulting in reduced thermal gradients and improved thermal stability. At smaller layer thicknesses, the square source exhibits a well-defined optimal processing window across the higher power-velocity range (300-600 W), Figure 4.9b, consistent with experimentally observed trends [15]. It is clear that the top-hat square source operates over a broader range of stable parameters than the circular Gaussian source. For instance, at (P,V)=(400 W,0.2 m/s), the Gaussian beam transitions into the keyhole regime, while the square beam remains in the conduction mode. This enhanced process stability stems from the uniform and spatially diluted energy distribution of the square beam, which minimizes localized overheating and suppresses keyhole formation [11, 22]. Furthermore, the melting behavior transitions toward keyhole-mode melting with decreasing spot size, lower scan speeds, and higher laser power [15]. As observed when the spot size is reduced from 75 μm to 37.5 μm for the top-hat beam, heat input becomes more concentrated, enhancing energy absorption within a smaller area 4.8c. Combined with increased laser power and reduced velocity, this intensified energy input promotes deeper penetration and the formation of keyhole-mode melt pools.

For Ti-6Al-4V in L-PBF, the conventional layer thickness working range is $20 - 60\,\mu$m. This range balances full melting, good surface quality, and interlayer bonding. Increasing the powder layer thickness beyond this range, such as to 100 μm, dramatically reduces process stability unless the laser energy input is significantly increased, which can be covered through the Gaussian Beam profile. The porosity can rise from about 0.09% at 20μm to 10.68% at 100 μm, mainly due to incomplete melting and trapped gas and can lead to unmolten regions which is evident from the process maps of Figure 4.9c and because the energy cannot penetrate fully through the thicker powder layer [41]. Also it was seen in [27, 42], lower layer thickness is generally attributed to highly dense parts and a better option for manufacturability when defining "better" by quality, density, and precision (e.g., for aerospace or biomedical components where fatigue life is critical). Considering these factors, the uniform intensity square source would be the better choice. The characteristics of the Top-Hat beam can ultimately lead to an improved and expanded process window, Figure 4.9b by trading off extreme keyholing risk for managed energy input. The stable nature of the Top-Hat melt pool enables achieving high relative densities and overall higher build rates compared to Gaussian beams in certain operational windows, in our case, it is very evident that complete optimal window is depicted.

The present semi-analytical framework is purely thermal and does not account for fluid flow, recoil pressure, or multiple reflections that become significant in deep keyhole mode. As a result, the onset of keyholing may be slightly under- or over-predicted in certain regions of the map. To maintain a conservative classification, the optimal regime is defined only when both keyhole and lack-of-fusion conditions are not met, which may marginally expand the predicted keyhole area compared to some reports [8].

Despite these simplifications, the constructed process maps offer an efficient screening tool: for each power-velocity pair, the model predicts steady-state melt-pool dimensions and defect type within seconds. The distinct behaviors of Gaussian and top-hat beams demonstrate that beam shaping can effectively tailor the process window using top-hat profiles to stabilize width and Gaussian beams for deeper penetration at lower power. Overall, the maps are physically consistent, align with literature trends, and provide a reliable basis for rapid parameter selection and beam-profile optimization prior to detailed experimental studies.

5 Conclusions and Future Work

5.1 Summary of Key Findings

The primary findings of this study include the process windows obtained for the different laser source shapes, namely the uniform-intensity square (top-hat) source and the 2D circular Gaussian source. It was observed that the optimal processing window for the 2D Gaussian source is relatively broader than that of the square source, particularly at larger layer thicknesses (e.g., 100 μm). However, when the layer thickness is reduced, the square source exhibits a more complete and well-defined optimal range. Furthermore, the melt pool widths were consistently found to be larger for the square source. The aspect ratio threshold of 0.5 was identified as indicative of the transition to the keyhole regime, consistent with trends observed in experimental studies. The spot size also had a significant influence, particularly for the uniform-intensity source. When the top-hat beam diameter was small (around 37.5 μm), the keyhole regime became more pronounced, whereas for larger and more conventional spot sizes, keyholing was rarely observed under equivalent processing conditions. Within the power–velocity range of 100–400 W and 0.1–0.4 m/s, keyholing was not observed for the 2D circular Gaussian source. However, extending this range to higher energy densities resulted in the onset of keyhole formation, as shown in Appendix C. The influence of layer thickness on the optimal process window was also evident. For instance, at a layer thickness of 30 μm, the model predictions for the point source showed near-perfect agreement with the experimental single-track results (Figure 4.9a), where the predicted dense regions closely matched those reported in literature. Although Gaussian laser sources are more commonly used in commercial L-PBF systems, uniform-intensity top-hat square beams are better suited for applications requiring improved part quality and dimensional consistency.

5.2 Contribution of the Thesis

The work presented in this study provides a foundation for gaining deeper insight into the L-PBF process using a semi-analytical approach. Incorporating different laser source shapes offers a new perspective on defect formation. The predictive capability of the developed model enables the identification and elimination of suboptimal operating conditions before experimentation, reducing both cost and time. The construction of process maps for the source shapes through the semi-analytical method provides a computationally efficient means of predicting parameter combinations that minimize defect occurrence. The model can classify defect regimes based on power and velocity inputs within seconds, functioning effectively for both single-point evaluations and full parametric sweeps. Unlike previous studies that relied solely on numerical or finite element methods, the semi-analytical approach bridges this gap, offering both efficiency and physical interpretability. A key contribution of this thesis is the derivation and implementation of a closed-form analytical formulation for the uniform-intensity square (top-hat) heat source, achieved through symbolic integration in Mathematica. This formulation extends the applicability of semi-analytical modeling to non-Gaussian beam profiles and establishes a foundation for future optimization of laser shaping strategies in metal additive manufacturing.

5.3 Limitations of the Current Study

The present model is best suited for evaluating melt pool characteristics under steady-state conditions rather than near the domain boundaries, where the adiabatic boundary assumption tends to break down. The semi-analytical framework developed in this work is purely thermal and does not incorporate fluid flow, recoil pressure, or multiple reflections, all of which play an important role in deep keyhole mode. Consequently, the model may underpredict or oversimplify the onset of keyholing in certain regions of the process map. To ensure conservative interpretation, the defect classification criteria were deliberately defined with narrow bounds, which may slightly enlarge the predicted keyhole regime compared to experimental observations. Since the heat source model assumes surface absorption and neglects vapor recoil and multiple reflections the regions identified as keyhole-prone should be regarded as indicators of increased susceptibility rather than fully developed keyhole geometries. The quantitative boundaries of these regimes remain sensitive to the chosen thresholds and could be further refined through calibration against experimental data. The mesh resolution adopted here represents a balance between computational cost and accuracy. While the current boundary condition enforcement is satisfactory, further improvements can be achieved through mesh refinement or the inclusion of mirror-source corrections in future implementations.

5.4 Recommendations for Future Research

The recommendations includes the following:

1. The methodology used here can be applied to other non-Gaussian sources-particularly ring beams and uniform-intensity circular beams-whose closed-form temperature fields have already been derived (see Appendix D). Implementing these sources within the semi-analytical framework would enable a systematic comparison of their melt-pool geometries, defect boundaries, and printable windows against the circular and square cases.

2. To assess model fidelity and quantify uncertainty, the results should be independently validated using commercial finite-element software (e.g., Simufact Additive). A black-box verification procedures matching material data, boundary conditions, and scan strategies would provide reference solutions for steady-state widths/depths and defect classification.

3. The current approach can be easily extended to full layer simulation to capture powder-to-solid transitions, inter-track overlap, and inter-layer reheating. This will enable more faithful prediction of cumulative heating, remelting, and defect evolution in build-relevant geometries.

4. Implementing Beer-Lambert absorption into the formulation that would account for laser attenuation, improving depth prediction and aligning the model more closely with experimental measurements.

Appendices

Appendix A Supplementary to Methodology

A.1 Green's Function

The green's function as the temperature at (x, y, z) at the time t due to an instantaneous point source of strength unity generated at the point P (x', y', z') at the time τ, the solid being initially at zero temperature and the surface being kept at zero temperature. This solution maybe written as : $u = F(x, y, z, x', y', z', t - \tau)$ $(t > \tau)$ and u satisfies the following equation

$$\frac{\partial u}{\partial t} = k\,\nabla^2 u, \quad (t > \tau) \tag{A.1}$$

However, since t only enters in the form $(t - \tau)$, we have also

$$\frac{\partial u}{\partial t} + k\,\nabla^2 u = 0 \quad (t > \tau) \tag{A.2}$$

Further, $\lim u$ at all the points inside S, except at the point (x', y', z'), where the solution takes the form

$$\frac{1}{8[\pi\,\alpha(t-\tau)]^{3/2}} \exp\left(-\frac{(x-x')^2 + (y-y')^2 + (z-z')^2}{4\alpha(t-\tau)}\right) \tag{A.3}$$

Finally, at the surface S, u= 0 $(t < \tau)$

A.2 Gaussian Convulation

Convolution is a mathematical operation that combines two functions to generate a third function, which represents how one function modifies or spreads the shape of the other. For two functions of the form :

$$f(x) = e^{-ax^2}, \quad g(x) = e^{-bx^2}$$

The direct evaluation integral will be of the form:

$$(f * g)(x) = \int_{-\infty}^{\infty} f(t)\, g(x-t)\, dt = \int_{-\infty}^{\infty} e^{-ax'^2 - b(x-x')^2}\, dt. \tag{A.4}$$

The convulation of two gaussians is another gaussian. The final expression obtained by convolving two gaussians takes the following form and is given in simpler terms Equation A.5:

$$\int_{-\infty}^{\infty} \exp\left(-a\,x'^2 - b\,(x-x')^2\right) dx' = \sqrt{\frac{\pi}{a+b}} \cdot \exp\left(-\frac{a\,b}{a+b}x^2\right) \tag{A.5}$$

This technique has been utilised to derive the temperature field formulation for the 2d gaussian source shape.

A.3 Error Functions

The function $\mathrm{erf}(z)$, known as the error function, arises in the integration of the normal distribution, which is the normalized form of the Gaussian function. It is an entire function defined as:

$$\mathrm{erf}(z) = \frac{2}{\sqrt{\pi}} \int_0^z e^{-t^2}, dt. \tag{A.6}$$

A.4 Steady state plots for Square and 2D gaussian sources

The steady-state temperature distributions for the 2D Gaussian and uniform-intensity top-hat sources are presented below, demonstrating that both source models achieve thermal stabilization over time.

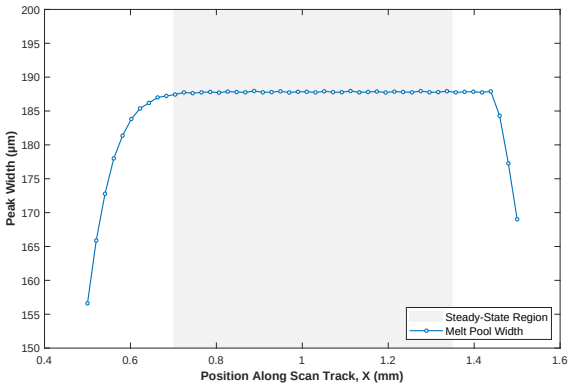

(a) Width vs. Position

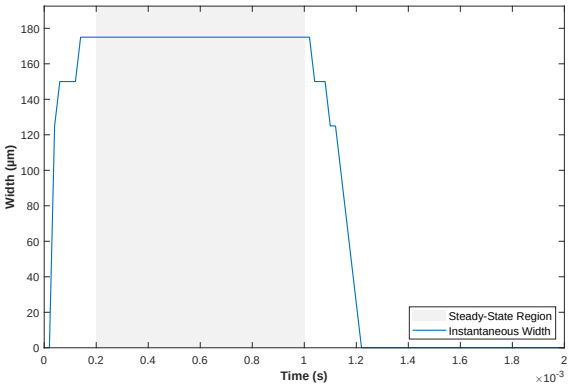

(b) Width vs. Time

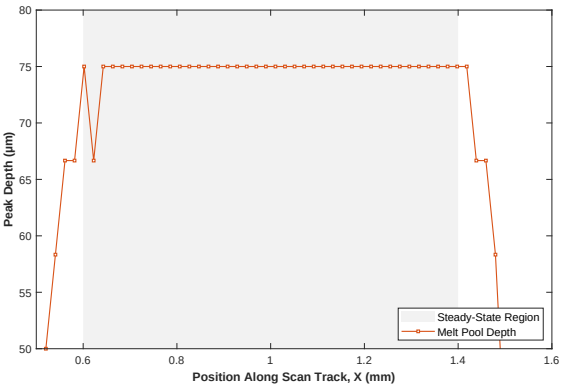

(c) Depth vs. Position

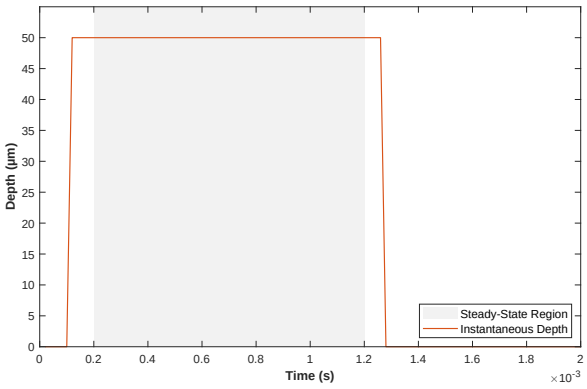

(d) Depth vs. Time

Figure A.1: Square top-hat source: melt-pool width and depth as functions of position and time.

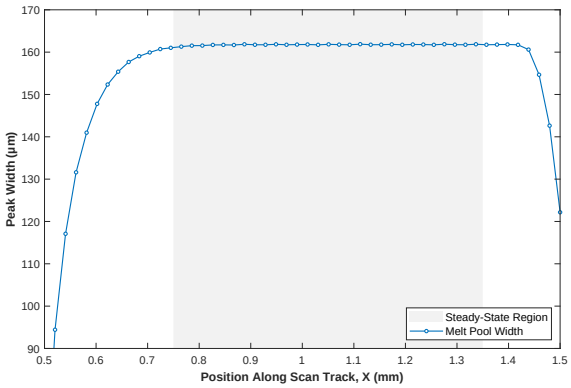

(a) Width vs. Position

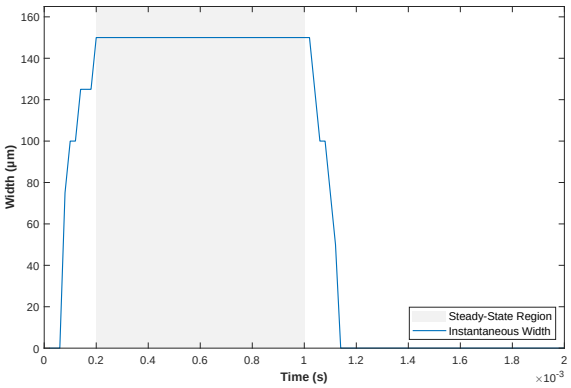

(b) Width vs. Time

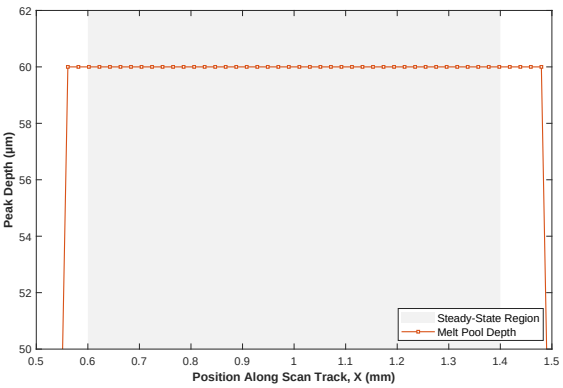

(c) Depth vs. Position

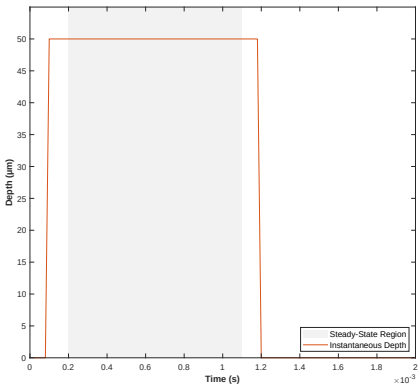

(d) Depth vs. Time

Figure A.2: 2D circular Gaussian source: melt-pool width and depth as functions of position and time.

Appendix B Simulation

B.1 Contour plots

In this section, the contour plots are presented corresponding to the simulation setup described in Chapter 3. For all source types, it is observed that applying the finite-difference scheme alone for the numerical correction field does not fully satisfy the adiabatic boundary condition. This is evident from the slight loss of contour orthogonality near the insulated surfaces, indicating minor deviations from the ideal zero-flux behavior.

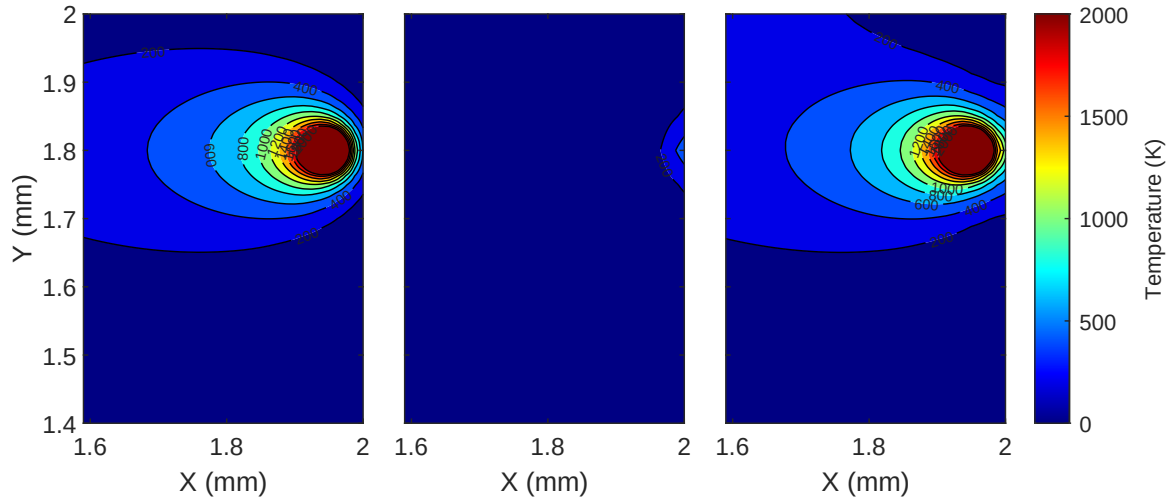

Figure B.1: Contour plots for the point source case.

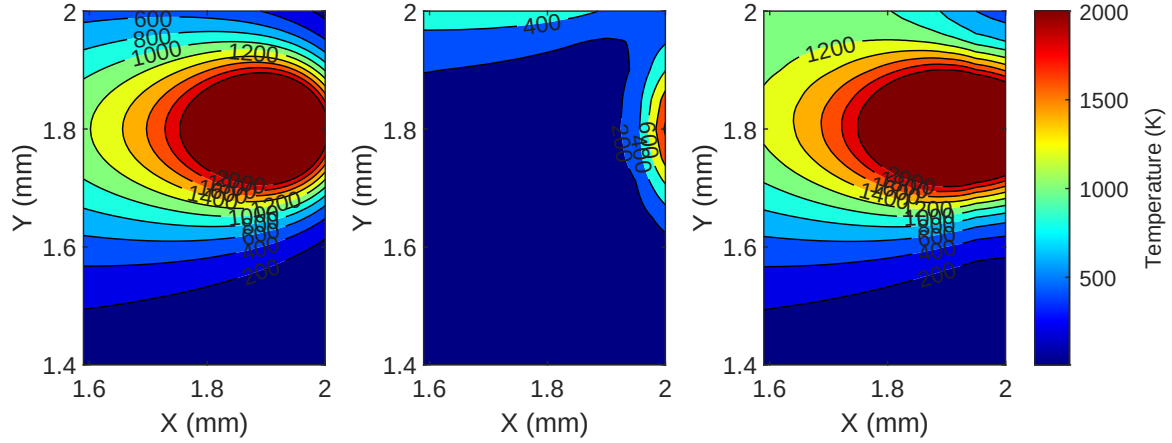

Figure B.2: Contour plots for the 2D circular Gaussian source.

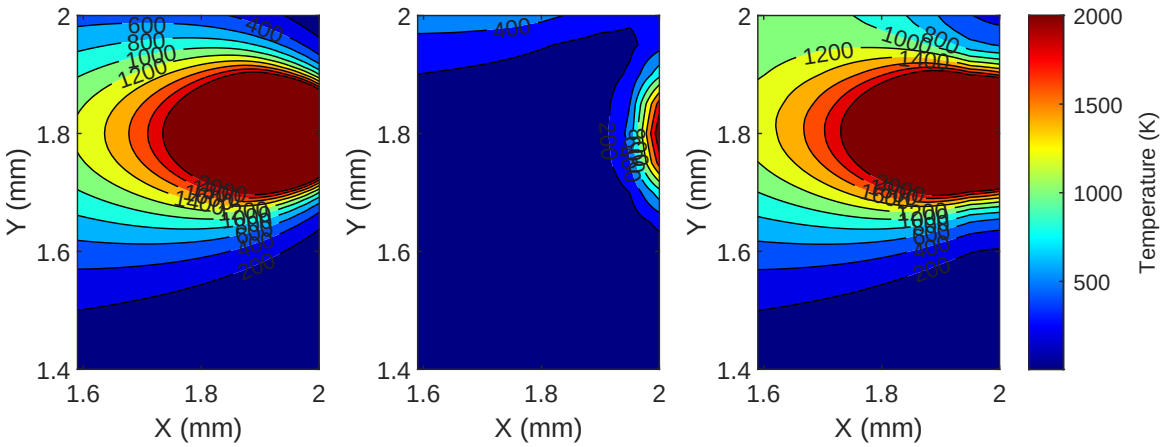

Figure B.3: Contour plots for the uniform intensity square top-hat source.

Appendix C Process Windows

C.1 Broad process window

The following process map is for the case where the power and velocity range has been made broad, so as to check if we see the keyholing or not. The Figure C.1a has been plotted for the extended window for the 2D Gaussian circular source for the high layer thickness case with 100μm. Figure C.1b has been plotted for the uniform intensity square source for the low spot size and layer thickness.

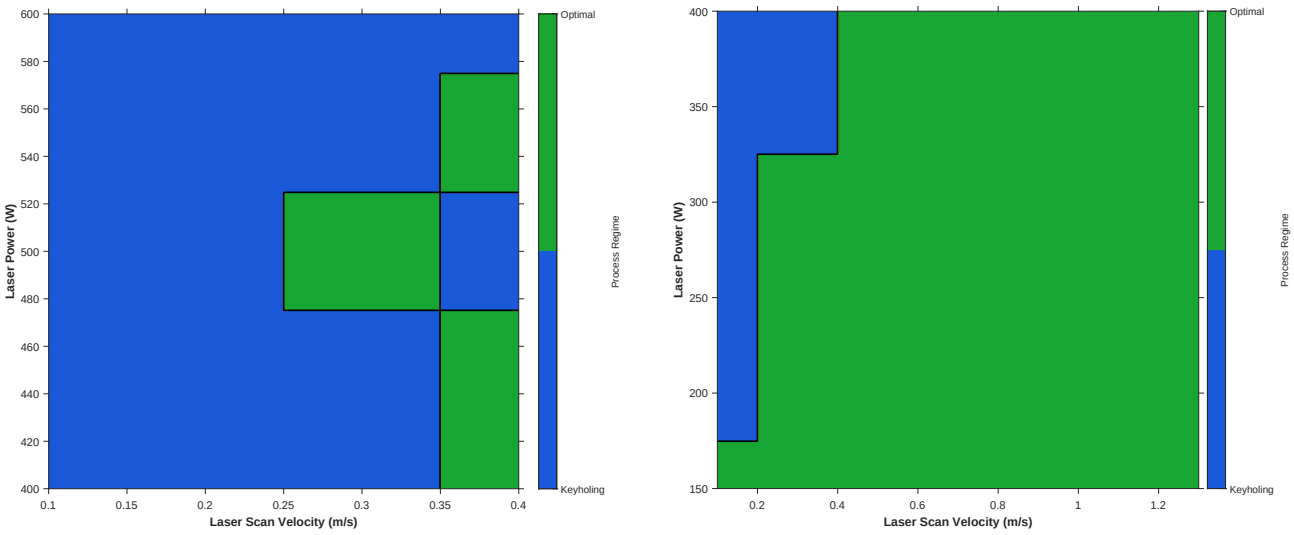

(a) (b)

Figure C.1: (a) For the 2D circular Gaussian source, widening the window depicts the keyholing region, for the layer thickness 100 μm. (b) Top-hat square source for the parametric window 150-400 W and 0.2-1.4 m/s, layer thickness = 30 μm, spot size = 37.5μm.

Appendix D Future direction

D.1 Ring/Donut/Annular

For the future work and direction, the following analytical formulation for ring source can be utilised. The heat energy distribution corresponding to the donut/ring/annular source is given by:

$$q_D(x,y,z) = \frac{2AP}{\pi\, R_o^2}\, \exp\!\left(-\frac{2r^2}{R_o^2}\right)\left[1-\exp\!\left(-\frac{2r^2}{R_{\text{inner}}^2}\right)\right]$$

where R_0 is the outer radius and R_i is the inner radius. Using the above energy distribution, similar steps like Gaussian Circular can be followed:

$$\begin{aligned} dT = \int_{-\infty}^{\infty}\int_{-\infty}^{\infty} & \frac{dx'\,dy'}{\rho c[4\pi\alpha(t-t')]^{3/2}}\frac{2\,A\,P}{\pi R_o^2} \\ & \exp\left(-\frac{-2(x'^2+y^2)}{R_o^2}\right)\exp\left(-\frac{(x-x')^2+(y-y')^2+z^2}{4\alpha(t-t')}\right) - \\ & \exp\left(-\frac{-2(x'^2+y^2)}{R_o^2}\right)\exp\left(-\frac{-2(x'^2+y^2)}{R_i^2}\right)\exp\left(-\frac{(x-x')^2+(y-y')^2+z^2}{4\alpha(t-t')}\right) \end{aligned} \tag{D.1}$$

Finally the closed form equation is given by:

$$\begin{aligned} T(x,y,z,t) = & \frac{8\,\alpha\,A\,P}{\rho\,c\left(4\pi\alpha\,(t-t_p)\right)^{3/2}}\exp\!\left(-\frac{z^2}{4\alpha\,(t-t_p)}\right) \\ & \left[\frac{(t-t_p)\,\exp\!\left(-\dfrac{2(x^2+y^2)}{R_o^2+8\alpha\,(t-t_p)}\right)}{R_o^2+8\alpha\,(t-t_p)} + \right. \\ & \left. \frac{R_i^2\,(t_p-t)\,\exp\!\left(-\dfrac{2(R_i^2+R_o^2)(x^2+y^2)}{8\alpha R_o^2(t-t_p)+R_i^2\left(R_o^2+8\alpha\,(t-t_p)\right)}\right)}{8\alpha R_o^2(t-t_p)+R_i^2\left(R_o^2+8\alpha\,(t-t_p)\right)}\right] \end{aligned} \tag{D.2}$$

$$\tau := t-t_p,\quad r_\perp^2 := x^2+y^2,\quad \Gamma_o := R_o^2+8\alpha\,\tau,\quad \Gamma_i := 8\alpha R_o^2\tau + R_i^2\Gamma_o. \tag{D.3}$$

$$T(x,y,z,t) = \frac{8\alpha AP}{\rho c\left(4\pi\alpha\tau\right)^{3/2}}\,\exp\!\left(-\frac{z^2}{4\alpha\tau}\right)\left(\frac{\tau}{\Gamma_o}\,e^{-\,2r_\perp^2/\Gamma_o} + \frac{R_i^2(-\tau)}{\Gamma_i}\,e^{-\,2(R_i^2+R_o^2)\,r_\perp^2/\Gamma_i}\right). \tag{D.4}$$

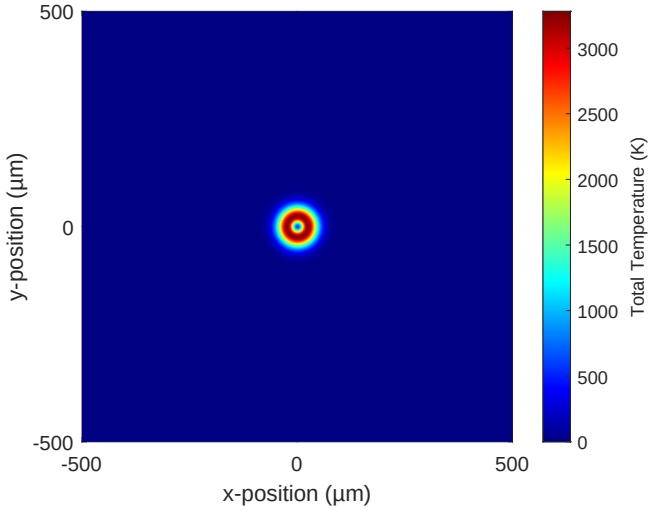

Figure D.1: Stationary Ring source at 1μs after its creation.

D.2 Uniform intensity Circular

Convert to polar coordinates: $x' = r'\cos\theta$, $y' = r'\sin\theta$, where r' is the instantaneous circular source in the plane z'=0. using $r = x^2 + y^2$

Substitute into the heat expression:

$$T(r,\theta,z,t) = \int_0^{2\pi}\int_0^{R} \frac{\exp\left(-\frac{r^2+z^2+r'^2-2\cdot r\cos\theta\cdot r'\cos\theta-2r\sin\theta\cdot r'\sin\theta}{4\alpha(t-t_0)}\right)}{(4\pi\alpha(t-t_0))^{3/2}}\, r'\, dr'\, d\theta \tag{D.5}$$

Now this expression can be integrated over θ from 0 to 2π and r' from 0 to R using Mathematica.

The inner integral with respect to θ gives the following expression:

$$T(r,\theta,z,t) = \frac{2\, e^{-\frac{r'^2}{4\alpha(t-t_0)}}\, \pi\, I_0\left(\frac{r'r}{2\alpha(t-t_0)}\right)}{(t-t_0)^{3/2}}, \tag{D.6}$$

where $I_0\left(\frac{r'r}{2\alpha(t-t_0)}\right)$ is the bessel function of the first kind. Finally, integrating with respect to the radius of the circular source, the final expression is going to be as follows:

$$T(x,y,z,t) = \frac{P\Delta t\, A}{4\rho c_p\, \pi\, R^2\, (\pi\alpha)^{3/2}} \exp\left(-\frac{r^2+z^2+r'^2}{4\alpha(t-t_0)}\right) \frac{2\,\pi\, I_0\left(\frac{r'r}{2\alpha(t-t_0)}\right)}{(t-t_0)^{3/2}} \tag{D.7}$$

Final temperature equation is as follows, which includes the outer integral as is, as a closed form is not coming out. The only possibility is to perform the numerical integration.

$$T(r,\theta,z,t) = \frac{P\Delta t\, A}{4\rho c_p\, \pi\, R^2\, (\pi\alpha)^{3/2}} \exp\left(-\frac{r^2+z^2}{4\alpha(t-t_0)}\right) \int_0^{R} \frac{2\pi\, \exp\left(-\frac{r'^2}{4\alpha(t-t_0)}\right)\, I_0\left(\frac{r'r}{2\alpha(t-t_0)}\right)}{(t-t_0)^{3/2}}\, r'\, dr' \tag{D.8}$$

Bibliography

[1] P. Nyamekye, P. Nieminen, M. R. Bilesan, E. Repo, H. Piili, and A. Salminen, "Prospects for laser based powder bed fusion in the manufacturing of metal electrodes: A review," *Applied Materials Today*, vol. 23, p. 101040, 2021.

[2] M. Balbaa, S. Mekhiel, M. Elbestawi, and J. McIsaac, "On selective laser melting of inconel 718: Densification, surface roughness, and residual stresses," *Materials & Design*, vol. 193, p. 108818, 2020.

[3] M. Sattari, A. Ebrahimi, M. Luckabauer, and G.-w. R. Römer, "The effect of the laser beam intensity profile in laser-based directed energy deposition: A high-fidelity thermal-fluid modeling approach," *Additive Manufacturing*, vol. 86, p. 104227, 2024.

[4] Z.-J. Li, H.-L. Dai, J. Xu, and Z.-W. Huang, "A semi-analytical approach for analysis of thermal behaviors coupling heat loss in powder bed fusion," *International Journal of Heat and Mass Transfer*, vol. 201, p. 123621, 2023.

[5] A. K. Agrawal, B. Rankouhi, and D. J. Thoma, "Predictive process mapping for laser powder bed fusion: A review of existing analytical solutions," *Current Opinion in Solid State and Materials Science*, vol. 26, no. 6, p. 101024, 2022.

[6] Y. Yang, M. Knol, F. Van Keulen, and C. Ayas, "A semi-analytical thermal modelling approach for selective laser melting," *Additive manufacturing*, vol. 21, pp. 284–297, 2018.

[7] J. Dilip, S. Zhang, C. Teng, K. Zeng, C. Robinson, D. Pal, and B. Stucker, "Influence of processing parameters on the evolution of melt pool, porosity, and microstructures in ti-6al-4v alloy parts fabricated by selective laser melting," *Progress in Additive Manufacturing*, vol. 2, no. 3, pp. 157–167, 2017.

[8] J. V. Gordon, S. P. Narra, R. W. Cunningham, H. Liu, H. Chen, R. M. Suter, J. L. Beuth, and A. D. Rollett, "Defect structure process maps for laser powder bed fusion additive manufacturing," *Additive Manufacturing*, vol. 36, p. 101552, 2020.

[9] S. Chowdhury, N. Yadaiah, C. Prakash, S. Ramakrishna, S. Dixit, L. R. Gupta, and D. Buddhi, "Laser powder bed fusion: a state-of-the-art review of the technology, materials, properties & defects, and numerical modelling," *Journal of Materials Research and Technology*, vol. 20, pp. 2109–2172, 2022.

[10] S. Sun, M. Brandt, and M. Easton, "Powder bed fusion processes: An overview," *Laser additive manufacturing*, pp. 55–77, 2017.

[11] A. Ebrahimi, M. Sattari, A. Babu, A. Sood, G.-W. R. Römer, and M. J. Hermans, "Revealing the effects of laser beam shaping on melt pool behaviour in conduction-mode laser melting," *Journal of Materials Research and Technology*, vol. 27, pp. 3955–3967, 2023.

[12] S. A. Khairallah, A. T. Anderson, A. Rubenchik, and W. E. King, "Laser powder-bed fusion additive manufacturing: Physics of complex melt flow and formation mechanisms of pores, spatter, and denudation zones," *Acta Materialia*, vol. 108, pp. 36–45, 2016.

[13] M. Bayat, R. Rothfelder, K. Schwarzkopf, A. Zinoviev, O. Zinovieva, C. Spurk, M. Hummel, A. Olowinsky, F. Beckmann, J. Moosmann, *et al.*, "Exploring spatial beam shaping in laser powder bed fusion: High-fidelity simulation and in-situ monitoring," *Additive Manufacturing*, vol. 93, p. 104420, 2024.

[14] I. Yadroitsev, I. Yadroitsava, A. Du Plessis, and E. MacDonald, *Fundamentals of laser powder bed fusion of metals*. Elsevier, 2021.

[15] C. Tenbrock, F. G. Fischer, K. Wissenbach, J. H. Schleifenbaum, P. Wagenblast, W. Meiners, and J. Wagner, "Influence of keyhole and conduction mode melting for top-hat shaped beam profiles in laser powder bed fusion," *Journal of Materials Processing Technology*, vol. 278, p. 116514, 2020.

[16] C. Boley, S. A. Khairallah, and A. M. Rubenchik, "Calculation of laser absorption by metal powders in additive manufacturing," *Applied optics*, vol. 54, no. 9, pp. 2477–2482, 2015.

[17] J. Trapp, A. M. Rubenchik, G. Guss, and M. J. Matthews, "In situ absorptivity measurements of metallic powders during laser powder-bed fusion additive manufacturing," *Applied Materials Today*, vol. 9, pp. 341–349, 2017.

[18] W. E. King, H. D. Barth, V. M. Castillo, G. F. Gallegos, J. W. Gibbs, D. E. Hahn, C. Kamath, and A. M. Rubenchik, "Observation of keyhole-mode laser melting in laser powder-bed fusion additive manufacturing," *Journal of Materials Processing Technology*, vol. 214, no. 12, pp. 2915–2925, 2014.

[19] D. Weckman, H. Kerr, and J. Liu, "The effects of process variables on pulsed nd: Yag laser spot welds: Part ii. aa 1100 aluminum and comparison to aisi 409 stainless steel," *Metallurgical and Materials Transactions B*, vol. 28, no. 4, pp. 687–700, 1997.

[20] P. Promoppatum, S.-C. Yao, P. C. Pistorius, and A. D. Rollett, "A comprehensive comparison of the analytical and numerical prediction of the thermal history and solidification microstructure of inconel 718 products made by laser powder-bed fusion," *Engineering*, vol. 3, no. 5, pp. 685–694, 2017.

[21] A. R. Bakhtari, H. K. Sezer, O. E. Canyurt, O. Eren, M. Shah, and S. Marimuthu, "A review on laser beam shaping application in laser-powder bed fusion," *Advanced Engineering Materials*, vol. 26, no. 14, p. 2302013, 2024.

[22] W. Yuan, H. Chen, S. Li, Y. Heng, S. Yin, and Q. Wei, "Understanding of adopting flat-top laser in laser powder bed fusion processed inconel 718 alloy: simulation of single-track scanning and experiment," *Journal of Materials Research and Technology*, vol. 16, pp. 1388–1401, 2022.

[23] T. T. Roehling, R. Shi, S. A. Khairallah, J. D. Roehling, G. M. Guss, J. T. McKeown, and M. J. Matthews, "Controlling grain nucleation and morphology by laser beam shaping in metal additive manufacturing," *Materials & Design*, vol. 195, p. 109071, 2020.

[24] S. Abadi, Y. Mi, F. Sikstrom, A. Ancona, I. Choquet, *et al.*, "Effect of shaped laser beam profiles on melt flow dynamics in conduction mode welding," *International Journal of Thermal Sciences*, vol. 166, 2021.

[25] J. Katagiri, M. Kusano, S. Minamoto, H. Kitano, K. Daimaru, M. Tsujii, and M. Watanabe, "Melt pool shape evaluation by single-track experiments and finite-element thermal analysis: Balling and lack of fusion criteria for generating process window of inconel738lc," *Materials*, vol. 16, no. 4, p. 1729, 2023.

[26] S. Sheikh, B. Vela, P. Honarmandi, P. Morcos, D. Shoukr, I. Karaman, A. Elwany, and R. Arróyave, "An automated computational framework to construct printability maps for additively manufactured metal alloys," *npj Computational Materials*, vol. 10, no. 1, p. 252, 2024.

[27] M. A. Mahmood, K. Ishfaq, M. Oane, M. Khraisheh, and F. Liou, "Integrated approach for alsi10mg rapid part qualification: Fem, machine learning, and experimental verification in lpbf-based additive manufacturing process," *Progress in Additive Manufacturing*, pp. 1–14, 2024.

[28] R. Rothfelder, M. Bayat, D. Bartels, M. Döring, L. Chechik, J. H. Hattel, and M. Schmidt, "Beam shaping and high layer thicknesses: A recipe for success for high build rates?," *Available at SSRN 5157226*.

[29] T. Stoll, R. Prudlik, M. Birg, and K. Wudy, "Influence of different beam shapes on melt pool geometry of single melt tracks on in718," *Progress in Additive Manufacturing*, vol. 10, no. 4, pp. 2675–2690, 2025.

[30] H. S. Carslaw, "J. c. jaeger," *Conduction of heat in solids*, vol. 2, 1959.

[31] S. Shrestha and K. Chou, "A study of transient and steady-state regions from single-track deposition in laser powder bed fusion," *Journal of Manufacturing Processes*, vol. 61, pp. 226–235, 2021.

[32] B. Lane, J. Heigel, R. Ricker, I. Zhirnov, V. Khromschenko, J. Weaver, T. Phan, M. Stoudt, S. Mekhontsev, and L. Levine, "Measurements of melt pool geometry and cooling rates of individual laser traces on in625 bare plates," *Integrating materials and manufacturing innovation*, vol. 9, no. 1, pp. 16–30, 2020.

[33] J. S. Weaver, J. C. Heigel, and B. M. Lane, "Laser spot size and scaling laws for laser beam additive manufacturing," *Journal of Manufacturing Processes*, vol. 73, pp. 26–39, 2022.

[34] R. Seede, D. Shoukr, B. Zhang, A. Whitt, S. Gibbons, P. Flater, A. Elwany, R. Arroyave, and I. Karaman, "An ultra-high strength martensitic steel fabricated using selective laser melting additive manufacturing: Densification, microstructure, and mechanical properties," *Acta Materialia*, vol. 186, pp. 199–214, 2020.

[35] Y. Huang, T. G. Fleming, S. J. Clark, S. Marussi, K. Fezzaa, J. Thiyagalingam, C. L. A. Leung, and P. D. Lee, "Keyhole fluctuation and pore formation mechanisms during laser powder bed fusion additive manufacturing," *Nature communications*, vol. 13, no. 1, p. 1170, 2022.

[36] D. Bombe, R. Kumar, S. K. Nandi, and A. Agrawal, "Semi-analytical formulation for single-track laser powder-bed fusion process to estimate melt-pool characteristics considering fluid-flow and marangoni effect," *International Journal on Interactive Design and Manufacturing (IJIDeM)*, vol. 18, no. 7, pp. 5121–5137, 2024.

[37] M. Tang, P. C. Pistorius, and J. L. Beuth, "Prediction of lack-of-fusion porosity for powder bed fusion," *Additive Manufacturing*, vol. 14, pp. 39–48, 2017.

[38] Q. C. Liu, J. Elambasseril, S. J. Sun, M. Leary, M. Brandt, and P. K. Sharp, "The effect of manufacturing defects on the fatigue behaviour of ti-6al-4v specimens fabricated using selective laser melting," *Advanced Materials Research*, vol. 891, pp. 1519–1524, 2014.

[39] H. O. Psihoyos and G. N. Lampeas, "Density-based optimization of the laser powder bed fusion process based on a modelling framework," *Alloys*, vol. 2, no. 1, pp. 55–76, 2023.

[40] R. Rothfelder, M. Bayat, D. Bartels, M. Döring, L. Chechik, J. H. Hattel, and M. Schmidt, "Beam shaping and high layer thicknesses: A recipe for success for high build rates?," *Available at SSRN 5157226*.

[41] C. Ni, J. Zhu, B. Zhang, K. An, Y. Wang, D. Liu, W. Lu, L. Zhu, and C. Liu, "Recent advance in laser powder bed fusion of ti–6al–4v alloys: microstructure, mechanical properties and machinability," *Virtual and Physical Prototyping*, vol. 20, no. 1, p. e2446952, 2025.

[42] S. P. Narra, A. D. Rollett, A. Ngo, D. Scannapieco, M. Shahabi, T. Reddy, J. Pauza, H. Taylor, C. Gobert, E. Diewald, *et al.*, "Process qualification of laser powder bed fusion based on processing-defect structure-fatigue properties in ti-6al-4v," *Journal of Materials Processing Technology*, vol. 311, p. 117775, 2023.